University College London

Department of Physics & Astronomy

Application of Quantum Magnetometers to Security and Defence Screening

By

Sarah Yasmin Hussain

A thesis submitted to

University College London

for the degree of

Doctor of Philosophy

I, Sarah Yasmin Hussain, confirm that the work presented in this thesis is my own. Where information has been derived from other sources, I confirm that this has been indicated in the thesis.

Signed ..... Date .....

Application of Quantum Magnetometers to Security and Defence Screening

Sarah Yasmin Hussain

Doctor of Philosophy of Physics

University College London

Prof. Ferruccio Renzoni, Supervisor

Abstract

Over recent years the sensitivity of alkali-metal vapour magnetometers has been demonstrated to surpass that of even Superconducting Quantum Interference Devices (SQUIDs), the current commercial gold standard in laboratory weak-field magnetometry sensing. Here we present a proof-of-principle approach to building an RF atomic magnetometer which is robust, portable, tunable, non-invasive and operable at room temperature in an unshielded environment. In view of these characteristics, we discuss the potential application of alkali-metal magnetometry in imaging concealed objects, non-destructive evaluation of the structural integrity of metallic objects (e.g. pipelines and aircraft), and detection of rotating motors.

We present a cost-effective approach to operating an atomic magnetometer in a Magnetic Induction Tomography (MIT) modality, to non-invasively map the conductivity of conductive objects concealed by conductive materials remotely and in real time. This is achieved by measuring the secondary field in the subject due to eddy currents circulating as a result of application of a tunable radio-frequency oscillating field, which overcomes the bandwidth and sensitivity limitations of using coils for sensing as in conventional MIT.

In addition, we demonstrate the use of the atomic magnetometer for the remote detection of DC and AC electric motors with an improved response compared with a commercial fluxgate magnetometer in the sub 50 Hz regime (particularly detection down to 15 Hz). Its capability for non-invasive measurement through concrete walls is established, with potential for use in industrial monitoring and detection of illicit activity.

Finally, the possibility of detection of submerged targets or for the atomic magnetometer to be mounted on submarine vehicles was explored. Promising results were obtained, but further investigation is required in this environment to establish this as a viable marine detector.

Acknowledgments

Wrapping up this thesis has had a profound effect on me- it has served as a diary of sorts for the last few years, both inside and outside of the lab. The writing process has most definitely been a chance to reflect on those who have helped shape this body of work, and here I take the opportunity to thank them.

My supervisor, Ferruccio, for introducing me to this exciting project and giving me the chance to work on it. I have learnt so many unusual and unexpected skills. I am hugely grateful to you for reading the first, possibly poorly worded and difficult to read incarnations of this thesis; your suggestions for improvements were invaluable.

My thanks to Luca for also re-reading the entire document, with some fantastic comments and questions to think about. However, I don't think I can thank you enough for all the discussions, technical assistance and patience you have demonstrated with me; I honestly couldn't have done it without you. You have been the powerhouse of this lab.

My heartfelt thanks also to my examiners, Paul Griffin and David Cassidy for reading my research and asking me some really great questions which helped me gain new insights into my work. I had more than a few 'lightbulb' moments!

As for the rest of the lab, I couldn't have asked for better colleagues. Cameron (he won't believe I'm saying this) has been a joy to work with on part of the experiment, Michela who has shown me such generosity in spirit, Raffa who always pushed me to be a better person, and Pik who taught me that having your life turned upside down is no reason to give up.

I would like to thank my Mum and Dad, in particular for always helping me along the path less trodden. You've never wavered in your belief in me and left me well equipped for making my own way in the world.

Thanks to Harry for casting his shrewd eye over this for me (he has always been my helper), and to Andy for giving me his opinion on 'his one and only gripe'.

Huge gratitude to Sammy, for cleaning everything up and making it all shiny again. She has been my fixer, guide and wise head. Saarah, Mina, Zoe, and Shib- you have truly taught me the value of friendship and Sisterhood, constantly seeing the world in a new way with me and never failing to make me howl with laughter. Mina wanted me to add this: 'Thank you to Mina Elton. You set me straight when I thought 500 words was an essay and look at me now.'

All of these people I owe so much to. But I couldn't end without a little thanks to Pocy and Apollo.

Thank you.

Contents

List of Figures

List of Tables

Chapter I

An Introduction to Optical Atomic Magnetometry

1 A Brief History

One of the primary discoveries that facilitated the development of Optical Atomic Magnetometers (OAMs) was of the magneto-optical effects of light with matter made by Michael Faraday– the so– called Faraday rotation. He describes in his 1845 paper [1] how he observed the rotation of the polarisation of light upon transmission through a glass block from light generated by an Argand lamp and directed parallel to magnetic field lines.

Just over a century later Dehmelt's observation of the transfer of angular momentum of polarised light to a sample of Mercury atoms [2] was expanded to later suggest that the Larmor precession (rotation of the magnetic moment of an object about the axis of an external magnetic field) of atomic spins due to their angular momenta could be used to measure magnetic field strengths [3]. Following on from Dehmelt's pioneering work, the first alkali-metal magnetometer was developed by Bell and Bloom in 1957. They used Dehmelt's optical pumping scheme and an additional so-called 'cross beam'; the latter being used to monitor the precession of Sodium atoms [4].

2 Principles of Optical Atomic Magnetometry

OAMs can be described as a general class of instruments that use light to collect information about the arrangement of atomic magnetic moments in response to an applied magnetic field [5]. Most atomic magnetometers use alkali metal vapours as the sensing medium but Helium is also currently used in some OAMs for space exploration owing to its potential for increased comparative sensitivity [6]. Modern OAMs are not dissimilar to Faraday's original demonstration in 1845; that is to say their operation can be defined by

the following processes [7]:

1. **Initialisation**,
2. **Spin Evolution**, and
3. **Readout**

of the atomic spin state. The first step requires transfer of angular momentum to the sample, resulting in a spin polarised state which is responsive to an external magnetic field. One way in which this can be achieved is via optical methods (see section I.2.3 and figure I.1); historically the Stern-Gerlach set-up has also been used for this purpose [8].

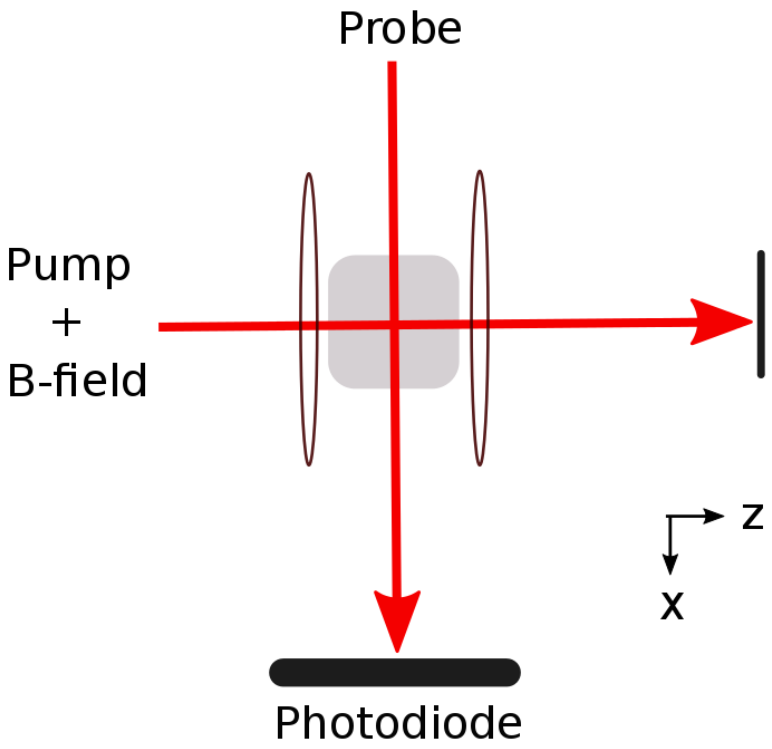

Figure I.1: An example of a type of OAM which uses optical pumping to spin polarise the atoms, which in this case is an Rb vapour. The pump laser beam provides angular momentum since it is circularly polarised and the probe beam monitors the atomic precessional modulation. The Rb vapour cell in the centre is surrounded by a Helmholtz coil pair that produce a static, homogenous, DC magnetic field with field lines parallel to the pump beam, both of which are used to spin polarise the atoms in the initialisation stage.

Once atoms are spin polarised, a torque is exerted on the atoms in the presence of a magnetic field which, due to their angular momentum, causes their magnetic moments to

precess [9] at a frequency proportional to the external magnetic field. This is the Larmor frequency [10] and is described in equation I.1:

$$\omega_L = \gamma B \tag{I.1}$$

where γ is a fundamental constant related to the electron charge, electronic rest mass, and the dimensionless electron g-factor. The precession of the atoms results in a changing spin state.

Finally, this changing spin state is then detected to determine the precessional frequency, and therefore, the magnetic field strength experienced by the atoms. Examples of how this can be achieved include the monitoring of atomic spin polarisation using off resonant light [11], monitoring transmitted intensity of an off-resonant probing beam [6], or the detection of secondary radiation produced by the precessing atoms [12].

Preparation, evolution, and detection are possible through a variety of means, giving rise to different families of atomic magnetometer. Varying methods impact sensitivity (the smallest detectable field), the required operating temperature, the choice of atom used as the sensor, the light sources used in the different processes or whether they measure scalar or vector quantities. Of these, the most sensitive magnetometer is the Spin-Exchange Relaxation-Free (SERF) sensor, developed at Princeton, which has the potential to reach sensitivities below 0.01 fT/$\sqrt{Hz}$ [13]. The sensitivity of OAMs is limited (in part) by spin exchange collisions between the atoms; the SERF magnetometer addresses this limitation by operating in the near-zero field and at a high atomic density [14]. In this technical configuration, the atomic spin-exchange is much more rapid than the precessional frequency, resulting in a condition where the the average spin remains more or less constant.

The type of magnetometer built for this PhD is an optically-pumped radio-frequency OAM (RF-OAM), a type of scalar magnetometer, using vapour phase Rubidium as the active sensing medium. The underlying physics regarding this type of sensor are set out in the subsequent sections.

2.1 Matter-Photon Interactions

In OAMs, the initialisation stage is completed using a light source– most use LASERs but it has been demonstrated that modern discharge lamps may have a comparable performance to LASERs for some OAM applications [15].

Light may interact with matter by means of several processes [16]: pair production, coherent scatter, Compton interactions, absorption, spontaneous emission and stimulated emission.

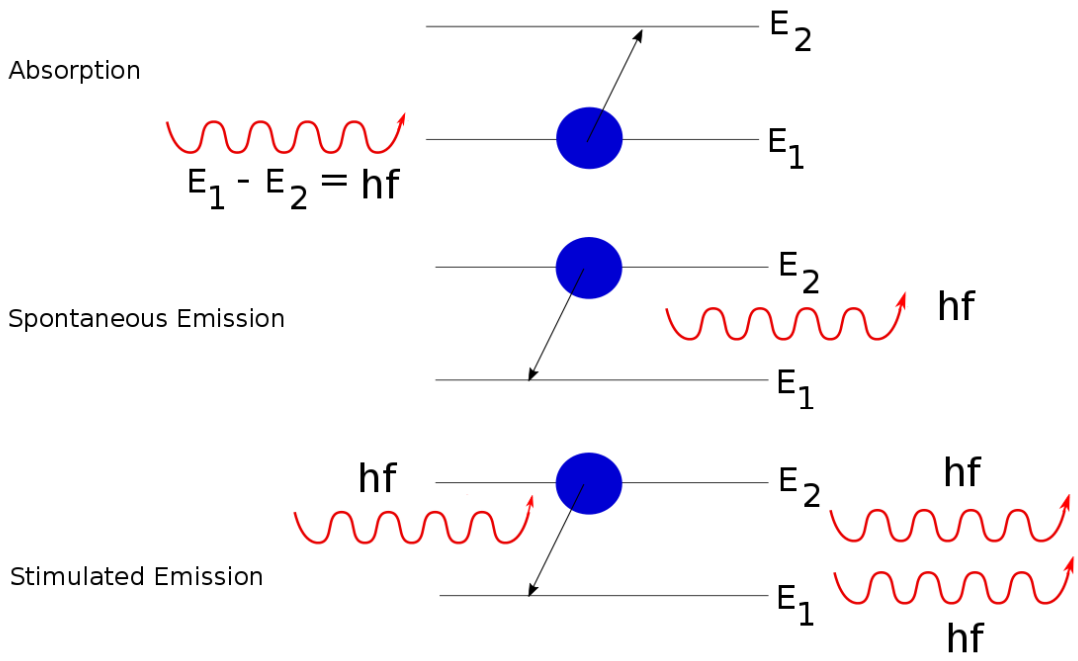

Figure I.2: Absorption, spontaneous emission and stimulated emission of photons in a two-level atom.

The relevant interactions in atomic magnetometry are absorption, spontaneous emission, and stimulated emission. Consider an atom with two discrete energy levels, E_1 and E_2, with an electron initially in the lower level E_1. An incoming photon may be described as consisting of a discrete individual packet, or quantum [17], of energy

$$E = hf = \hbar\omega, \tag{I.2}$$

with h, the Planck constant, $\hbar = \frac{h}{2\pi}$, and f and ω , the photon frequency.

Absorption of a photon of energy equal to E_2 - E_1 promotes the atom from E_1 to E_2. The electron in the E_2 level then may decay by spontaneous emission to E_1, with a photon of random direction and phase being radiated as a result. Stimulated emission occurs when atoms in an excited state are 'knocked out' of this energy level after interaction with an incoming photon of energy $\hbar\omega$, resulting in the release of a copy of the initial incoming photon and an additional photon in phase with the first, also of energy $\hbar\omega$. The OAM exploits absorption and spontaneous emission.

The strength of the light-atom coupling in the absorption interactions, H_l,

$$H_l = -\mathbf{D}\cdot\boldsymbol{\epsilon} = \hbar\,\Omega_R\,, \tag{I.3}$$

is proportional to Ω_R, the Rabi frequency [18], which is the rate at which the atomic populations between E_1 and E_2 are transferred [19]. H_l also depends on $\boldsymbol{\epsilon}$, the electric

field of the light and **D**, the electric dipole of the atom it is interacting with. As the beam is transmitted through the vapour, it is assumed to be quasimonochromatic in nature, and can be described by the following function [20]:

$$\boldsymbol{\epsilon} = \frac{\boldsymbol{\epsilon}_0}{2} \exp^{i(\mathbf{k}\cdot\mathbf{r}-\omega t)} \; + \; \text{c.c} \; . \tag{I.4}$$

In this expression, $\boldsymbol{\epsilon}_0$ is the complex amplitude, $\mathbf{k}$ has magnitude $\frac{\omega}{c}$ and the c.c term is the complex conjugate of the first part of the function. After interaction with this wave, the atom is most likely to decay by spontaneous emission, whose profile is observed as a Lorentzian spectral peak centred on $\hbar\omega$ with width equal to 1/lifetime of the excited level.

The broadening of the spectral line is due to three mechanisms [21]: lifetime broadening, collisional broadening and Doppler broadening. Lifetime broadening is so-called as it comes about due to the finite time lived in the excited state, the length of which varies between atoms due to the nature of spontaneous emission [22]. For an atom in an excited state, the uncertainty principle,

$$\Delta \text{E} \; \Delta \text{t} \gtrapprox \hbar, \tag{I.5}$$

states that there cannot be a precise measurement of E_2 - E_1 when the atoms decay by spontaneous emission with a finite lifetime. This smears the spectral linewidth for the transition as the error in energy measurement translates into an uncertainty on the frequency of the emitted radiation.

Collisions between the atoms perturb their excited states compared to when they are further apart, affecting the emission frequency and phase of a decaying atom. This introduces an additional source of broadening in the spectral line called collisional broadening [23]. It is also referred to as pressure broadening since the extent of this broadening is proportional to the atomic pressure [24].

The pump beam (in this case, the beam used to tranfer angular momentum to atoms, and is therefore mainly absorbed by them) used in this type of magnetometer can be assumed to be weak enough that spontaneous emission is much more probable than stimulated emission following absorption. The profile of the spontaneous emission spectrum is determined mainly by the Doppler broadening effect since it causes the spectral line to widen by around 100 times more than collisional and lifetime broadening at room temperature and pressure [25].

The Doppler broadening occurs due to the random motions of atoms in the alkali-metal vapour cell. Examining the case of an atom travelling at speed V_x, interacting with

a laser of frequency ω_0, has observed frequency [26]

$$\omega = \omega_0 \left(\frac{1 + V_x}{c} \right) \ . \tag{I.6}$$

Rearranging, it follows that

$$V_x = \left(\frac{c\,\omega}{\omega_0} \right) - 1 \tag{I.7}$$

$$dV_x = \frac{c}{\omega_0} d\omega \ . \tag{I.8}$$

In addition, the probability that this atom has a velocity between V_x and $V_x + dV_x$ is described by a Maxwell-Boltzmann distribution [27]:

$$P(V_x)dV_x = \sqrt{\frac{m}{2\pi\, k_B\, T}} \exp\left(\frac{-m\, V_x^2}{2 k_B\, T} \right) dV_x \ , \tag{I.9}$$

where m is the atomic mass, T is the temperature of the atoms and k_B is the Boltzmann constant.

Substitution of equation I.5 and I.6 yields the probability of detection of a wave of frequency in the range $\omega_0 \to \omega$:

$$P(\omega_0)d\omega = \frac{c}{\omega_0} \sqrt{\frac{m}{2\pi\, k_B\, T}} \exp\left(\frac{-m\, c^2 (\omega - \omega_0)^2}{2 k_B\, T\, \omega_o^2} \right) d\omega \ . \tag{I.10}$$

The extent of Doppler broadening is given by the full-width half maximum of this probability function [26]:

$$\delta_{\text{doppler}} = \frac{4\pi}{\lambda} \left(\frac{(2 \ln 2) k_{\text{B}}\, T}{m} \right)^{1/2} \ . \tag{I.11}$$

2.2 The Zeeman effect

Atoms have intrinsic momentum, **F**, that is the sum of the orbital angular momentum, **L**, of the valence electrons, the spin angular momentum, **S**, of these electrons, and the total nuclear angular momentum, **I** [28].

$$\mathbf{J{=}L{+}S} \tag{I.12}$$

$$\mathbf{F{=}J{+}I} \tag{I.13}$$

where **J** takes values from $|\mathbf{L{+}S}| \to |\mathbf{L\text{-}S}|$ and **F** takes values from $|\mathbf{J{+}I}| \to |\mathbf{J\text{-}I}|$.

Alkali-metal vapours are used since they have only one valence electron. As a result, coupling of the spin-orbit interaction is easier to exploit and analyse theoretically. In

addition, they are able to be interrogated by relatively inexpensive and readily available semiconductor lasers.

With no magnetic field acting on the atomic vapour, there is no general alignment of the magnetic momenta of the atoms. Optical pumping (described in more detail in I.2.3) is a necessary mechanism for the OAM to work since it can bring about a net magnetisation of the sample by forcing the momenta to align in a certain direction. The particular process to achieve optical pumping for this RF-OAM is two-fold– firstly, a DC homogeneous magnetic field must act upon the atoms and secondly, the vapour should be irradiated by means of polarised light in a direction of propagation parallel to the magnetic field lines. To pump the atoms using the so-called D_2 line (the D_1 line may also be used), from figure I.3, the tuning required for the pump beam is 780 nm for a transition between $5^2S_{1/2}$ and the $5^2P_{3/2}$ state.

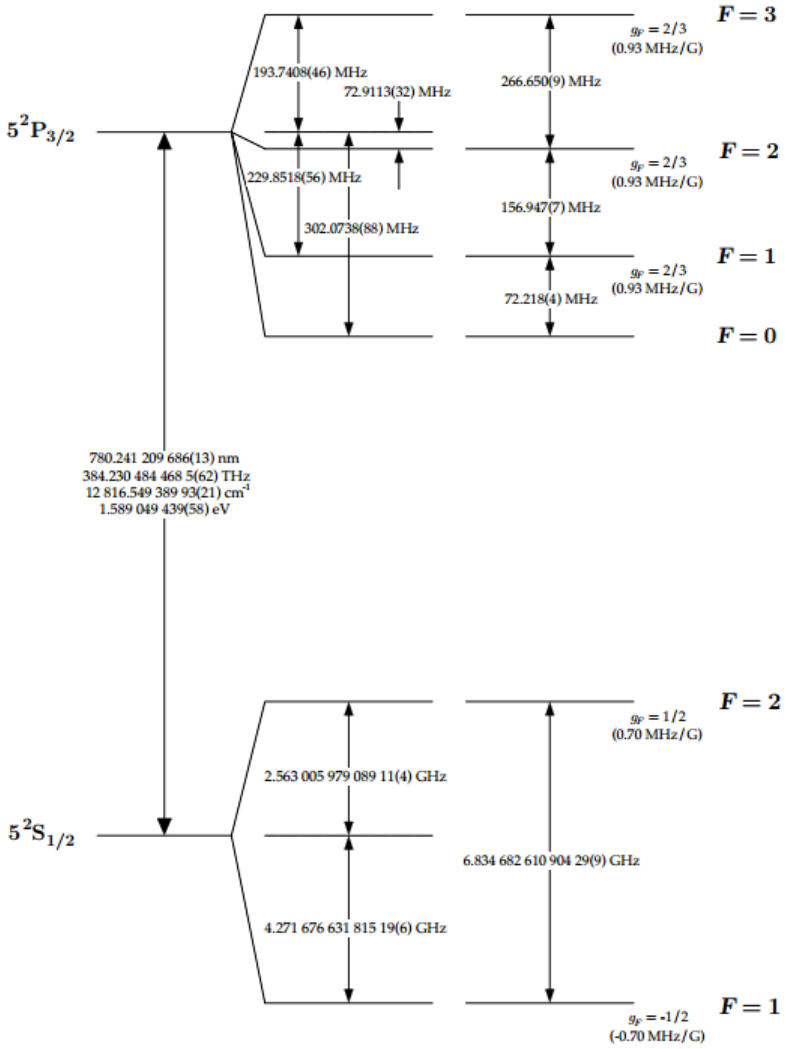

Figure I.3: ^{87}Rubidium D_2 hyperfine states and the frequency splitting between them [28]. The F states are further split into $2F+1$ equally spaced m_F quantum states.

Interaction between the magnetic dipole moment and an external magnetic field, $\mathbf{B}_0$, in this case applied by a Helmholtz coil pair, lifts the degeneracy inherent in the hyperfine structure. This phenomenon is known as the Zeeman effect. The Zeeman sublevels m_F are the projection of $\mathbf{F}$ onto the magnetic field quantisation axis [29]. There are $2F+1$ equally spaced hyperfine sublevels whose splitting is arranged in steps of one symmetrically about $m_F = 0$, with the energy gaps between them being proportional to the magnetic field strength.

The energy shift due to the Zeeman effect is [30]

$$\Delta E = g_F \mu_B \mathrm{B}_z m_F \ , \tag{I.14}$$

where μ_B is the Bohr magneton (atomic unit of the magnetic moment), B_z is the magnitude of the projection of $\mathbf{B}_0$ onto the quantisation axis, and g_F is given by:

$$g_F \approx g_J \frac{F(F+1) + J(J+1) - I(I+1)}{2F(F+1)} \ , \tag{I.15}$$

In this expression, the term g_J is the Landé g-factor, a term arising in the first order perturbation to the atom since B_z is weak, and is a dimensionless conversion factor to transform from angular momenta into units of μ_B.

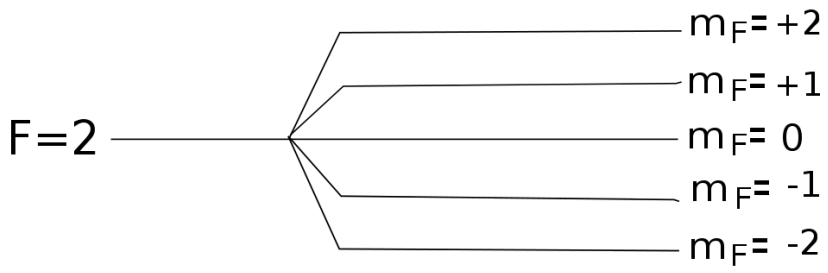

Figure I.4: ^{87}Rubidium Zeeman sublevel structure for Hyperfine splitting of F=2, under influence of a DC magnetic field. The m_F states are equidistant (an approximation only valid for weak fields); the extent of the splitting is proportional to the magnetic field strength.

The atomic magnetic moment is independent of an external field acting upon it at suitably small values; this is the regime in which the RF-OAM is operated. When the

field exceeds around 500 mG [31], however, the Zeeman shifts are much larger than the splittings from internal atomic fine interactions, leading to a coupling between the atomic magnetic moment and the external field [32]. In this regime, the Zeeman split hyperfine states are no longer equally separated and spectra exhibit additional splittings, resulting in a nonlinear dependence of the atomic precessional frequency on the external field.

The Zeeman energy sublevel splittings can be expanded in powers of the external field magnitude as per the Breit-Rabi equation [33]:

$$\Delta\ \mathrm{E}(F, m_f) = -\frac{E_{gs}}{2I+1}\ +\ (g_I\mu_N \pm \mu_{eff})Bm_F\ \pm\ \frac{\mu_{eff}^2 B^2 m_F^2}{E_{gs}}\ +\ 2\frac{\mu_{eff}^3 B^3 m_F^3}{(E_{gs})^2} \quad \text{(I.16)}$$

where E_{gs} is the ground state hyperfine splitting, g_I is the nuclear g-factor, μ_N is the nuclear magneton, $\mu_{eff} = \dfrac{g_e\mu_B\ +\ g_I\mu_N}{2I+1}$, and I is the nuclear spin.

The non-linear Zeeman regime is the origin of a source of error on scalar magnetometers; this is called the 'heading error' [34]. The absolute measurement of the magnetic field gains a dependence on orientation of the scalar device in relation to the 'strong' magnetic field lines, as a result of the coupling between the atomic magnetic moment and the external field.

2.3 Optical Pumping

Optical pumping employs absorption and spontaneous emission to prepare the atomic ensemble in a spin-polarised state. Considering a sample initially with electrons in the ground hyperfine F=2 state of a Zeeman split ^{87}Rb atom, there is no general alignment of the atomic vapour since their momenta are isotropically arranged.

Upon illumination of the atomic sample by on-resonant σ^+ polarised light, each photon can deliver $\hbar$ of angular momentum to a single electron changing its quantum state from $|\mathrm{F},\mathrm{m}_F - 1\rangle \rightarrow |\mathrm{F'},\mathrm{m}_F\rangle$, where F' is the excited state.

As set out in the formalism by Happer and Mathur [20], the effect of $\mathrm{H_l}$ on the vapour can be described by an effective ground state Hamiltonian expressed in terms of the electric field $\boldsymbol{\epsilon}$, of the pumping light source and $\boldsymbol{\alpha}^{(L)}$, the atomic polarisability. The perturbation to the ground state is

$$\partial H = -\boldsymbol{\epsilon}^\dagger\ \cdot\ \boldsymbol{\alpha}^{(L)}\ \cdot\ \boldsymbol{\epsilon}\ . \quad \text{(I.17)}$$

The Hamiltonian can also be written in terms of ∂E, the light shift operator and ∂T, the light absorption operator.

$$\partial H = \partial E - \ i\frac{\hbar}{2}\ \partial T\ . \quad \text{(I.18)}$$

∂E displaces the ground state energy levels whereas ∂T is a dissipatory term describing the pumping of atoms out of the ground state when they absorb a photon.
The effect of the light absorption operator,

$$\partial T = -\Gamma_{pump}\left(\frac{1}{2} - \frac{2}{2\mathbf{I}+1}\ \mathbf{S}\cdot\hat{s}\right)\ , \tag{I.19}$$

is determined by the mean spin of the irradiating photons,

$$\hat{s} = \frac{1}{|\epsilon_0|^2}\left(\boldsymbol{\epsilon}_0^{\dagger}\times\boldsymbol{\epsilon}_0\right)\ , \tag{I.20}$$

and the pumping rate of the atoms by the beam [35],

$$\Gamma_{pump} = \frac{\Omega_R^2}{\Gamma_0}, \tag{I.21}$$

where Γ_0 is the spontaneous emission rate and $\mathbf{S}$ is the electron spin.

By atomic selection rules [36], the electron may decay by spontaneous emission to either $|F,\mathrm{m}_F-1\rangle$, $|\mathrm{F},\mathrm{m}_F\rangle$ or $|F,\mathrm{m}_F+1\rangle$. By conservation of momentum, the polarisations of emitted light are determined by the spontaneous decay from excited to ground states (see Table I.1).

When the absorption and emission cycles repeatedly occur, eventually the atomic population will be transferred to the state with the largest value of angular momentum, or in the case of optical pumping in the F=2 to F'=3 line, m_F=+2, as illustrated in figure I.4. The atoms are now spin polarised and the extent of this polarisation, $\mathbf{P}$, can be found by [20]

$$\mathbf{P} = \langle\chi\rangle\cdot\frac{\boldsymbol{\epsilon}}{2} + c.c\ . \tag{I.22}$$

The susceptibility operator, χ, determines how strongly the atoms are magnetised in the presence of a magnetic field, and is

$$\chi = \mathrm{n}_{ad}\ \boldsymbol{\alpha}^{(L)}\ , \tag{I.23}$$

with n_{ad} the atomic density and c.c the complex conjugate. The polarisation of the sample and atomic density are therefore related to the effective ground state Hamiltonian of the vapour, the magnetometer signal, and ultimately the sensitivity of the device. Polarisation of the sample in conjunction with an aligned DC magnetic field in the same direction gives it known net magnetisation, and as a result, the atoms become sensitive to applied magnetic fields.

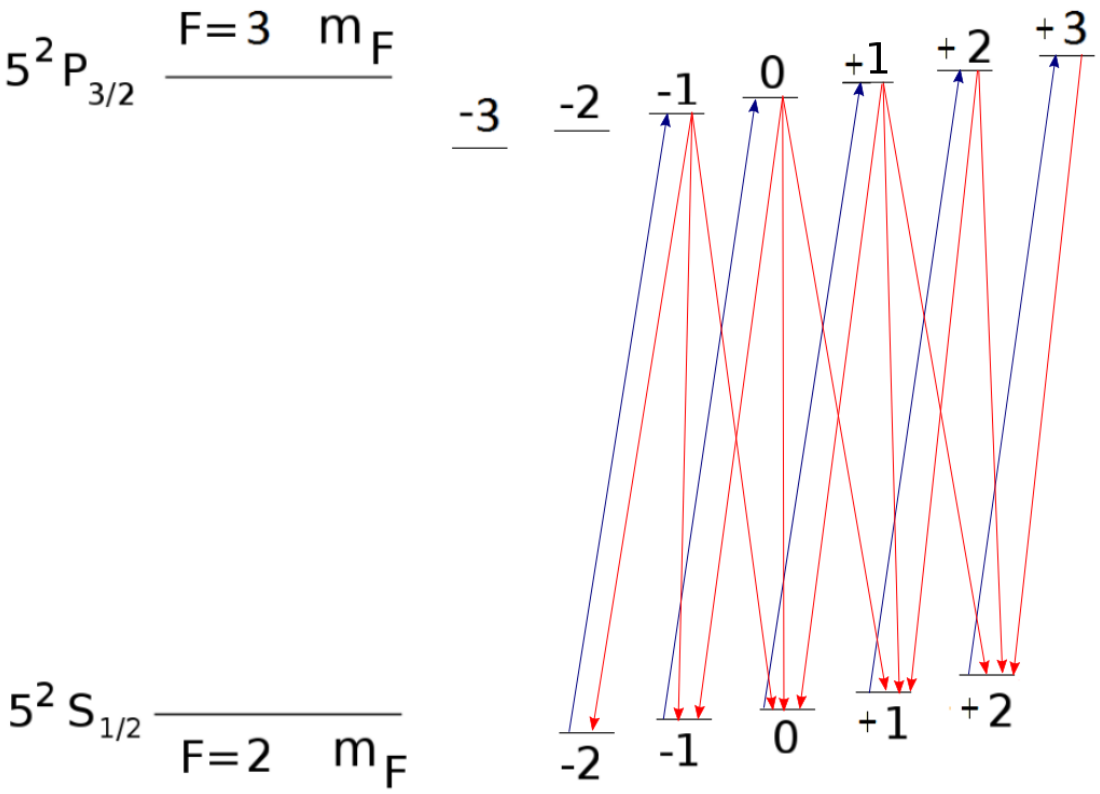

Figure I.5: Optical Pumping for the ^{87}Rb transition between the ground state F=2 to F'=3 excited states. Atoms are promoted to higher states when they exchange angular momentum with an incoming photon. By spontaneous emission, they decay down to F=2 states with either $m_F - 1$, m_F, or $m_F + 1$.

Ground m_F State	Excited m_F State	Allowed De-Excitation	Polarisation of Emitted Light
-2	-1	-2	σ^+
		-1	π
		0	σ^-
-1	0	-1	σ^+
		0	π
		+1	σ^-
0	+1	0	σ^+
		+1	π
		+2	σ^-
+1	+2	+1	σ^+
		+2	π
+2	+3	+2	σ^+

Table I.1: Allowed transitions between ground and excited states and the polarisations of emitted radiation.

2.4 Saturated Absorption Spectroscopy

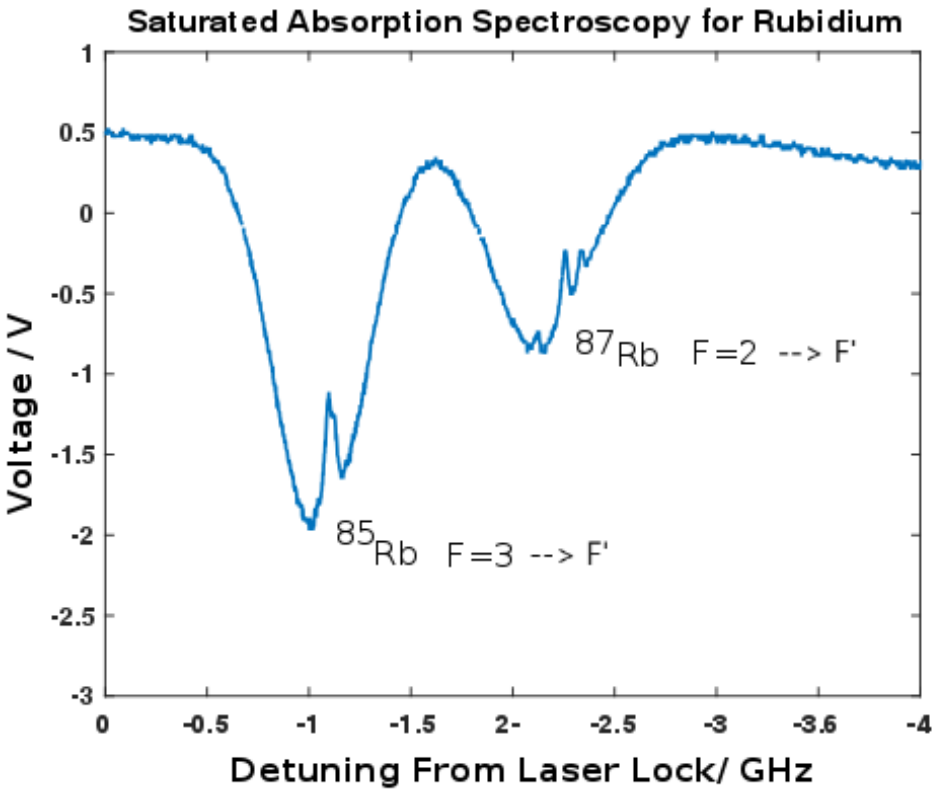

Figure I.6: Doppler-free (Saturated Absorption Spectroscopy) for rubidium. The hyperfine structure of the excited states are resolved unlike in the case of the Doppler broadened profile obtained without the use of a weak counter propagating 'probe' beam.

The Doppler-broadened Gaussian absorption profile obtained using a single beam passing through an alkali-metal vapour sample is too broad to resolve the hyperfine splitting of the excited states. Saturated absorption spectroscopy is a technique which allows resolving the excited states by firstly illuminating the sample with an intense pump beam, and secondly interrogating the vapour with a relatively weak probe beam.

Optical pumping of the medium until approximately half the atoms are in the excited quantum states 'saturates' the vapour. This can be achieved by a 'pump' beam with frequency ω travelling in, say, the $+x$ direction. The excitation of atoms to higher states is also known as hole burning, and refers to a dip in the population distribution of atoms in the ground state travelling at very particular velocities.

Due to the Doppler effect, a counter-propagating weak probe beam with the same frequency but heading in the direction of $-x$ interacts with a different velocity class of atoms and burns a hole in a different region of the population distribution.

When both beams are at or near the resonant frequency, both the pump and probe beams interact with the same atoms; those with velocity $V_x = 0$ [37]. Since the pump beam saturates the sample, the ground state population is depleted such that promotion to higher energy levels is highly improbable by the probe beam. This is seen at a photodiode as a relative peak in transmission intensity of the probe beam, with multiple peaks being visible. An example of the Spectroscopy is shown in figure I.6 for the Rubidium D2 line.

2.5 Monitoring the Spin Evolution

To find the atomic spin precession induced by a magnetic field, the RF-OAM measures the atomic spin rotation angle by comparing the plane of polarisation of a linearly polarised, off-resonant, weak beam before and after propagation through the vapour [38]. To demonstrate this, consider a linearly polarised beam travelling along the $\hat{\mathbf{x}}$ direction for a distance l through a spin polarised vapour. Linearly polarised beams can be described as being composed of two circularly polarised beams with opposite helicities, whose electric field function may be written [39]

$$\boldsymbol{\epsilon}(l) = \frac{\boldsymbol{\epsilon}_0}{4} \exp^{i\omega \mathrm{t}} (\hat{\mathbf{x}} + i\hat{\mathbf{z}}) \;\; + \;\; \frac{\boldsymbol{\epsilon}_0}{4} \exp^{i\omega \mathrm{t}} (\hat{\mathbf{x}} - i\hat{\mathbf{z}}) \;\; + \;\; c.c \; . \tag{I.24}$$

Defining the time taken to traverse the medium [39]

$$t = \frac{nl}{c} \; , \tag{I.25}$$

where n is the refractive index of the vapour and and c is the speed of light in air, the wavefunction can be expressed in terms of t:

$$\boldsymbol{\epsilon}(l) = \frac{\boldsymbol{\epsilon}_0}{4} \exp^{i\omega n_+ l/c} (\hat{\mathbf{x}} + i\hat{\mathbf{z}}) \;\; + \;\; \frac{\boldsymbol{\epsilon}_0}{4} \exp^{i\omega n_- l/c} (\hat{\mathbf{x}} - i\hat{\mathbf{z}}) \;\; + \;\; c.c \; . \tag{I.26}$$

The two helicities experience differing refractive indices of the medium and so are assigned separate values for this quantity, n_+ and n_-. Following manipulation of these values into the forms

$$\bar{n} = \frac{n_+ + n_-}{2} \tag{I.27}$$

and

$$\Delta n = \frac{n_+ - n_-}{2} \; , \tag{I.28}$$

and substitution of equation I.27 and I.28, I.26 may be rewritten

$$\boldsymbol{\epsilon}(l) = \frac{\boldsymbol{\epsilon}_0}{4} \exp^{i\omega \bar{n} l/c} \exp^{i\omega \Delta n l/c} (\hat{\mathbf{x}} + i\hat{\mathbf{z}}) \;\; + \;\; \frac{\boldsymbol{\epsilon}_0}{4} \exp^{i\omega \bar{n} l/c} \exp^{-i\omega \Delta n l/c} (\hat{\mathbf{x}} - i\hat{\mathbf{z}}) \;\; + \;\; c.c \; . \tag{I.29}$$

In equation I.29 it becomes clear that the two helicities have different phases as they pass through the medium. Since the rotation angle, θ_R, is by definition ω multiplied by the time taken by the beam to rotate by this angular distance,

$$\theta_R = \frac{\omega l}{c} \ \Re \ \Delta n \tag{I.30}$$

in terms of t, then substitution of equation I.30 into equation I.29, and cancellation of the common $\exp^{i\omega\bar{n}l/c}$ term leads to

$$\boldsymbol{\epsilon}(l) = \boldsymbol{\epsilon}_0 \left(\cos\theta_R \hat{\mathbf{x}} - \sin\theta_R \hat{\mathbf{z}}\right) \ . \tag{I.31}$$

This wavefunction describes the rotation of the plane of polarisation of linearly polarised beam of initial amplitude ϵ_0 by an angle θ_R as it traverses a birefringent medium.

In addition, the rotation angle, θ_R of the beam can be written in terms of the gyrotropic eigenvalue (where the left and right helicities of a plane polarised wave in a medium rotate at different speeds), α_g, of $\boldsymbol{\alpha}^{(L)}$ [40]:

$$\theta_R = 2\pi \ \mathrm{n_{ad}} \ \mathrm{k} \ \alpha_g \ l\langle \mathbf{n} \cdot \mathbf{S} \rangle \ . \tag{I.32}$$

In this expression, k has its usual meaning, the wavenumber of a wave vector, $\mathrm{n_{ad}}$ is the number density of polarised atoms, and $\mathbf{n}$ is the unit vector along the direction of travel of the probe beam. We see here that the comparison of the probe beam polarisation before and after passing through the vapour contains information about the electron spins, and ultimately, the magnetic field acting on the vapour.

3 Steady State Solutions of the Bloch Equation

Felix Bloch's 1946 paper 'Nuclear Induction' usefully proposes rate equations to describe the evolution of the macroscopic magnetisation of a spin ensemble upon application of a static DC field and an orthogonal RF field [41]:

$$\frac{d\mathbf{M}}{dt} = \gamma \mathbf{M} \times \mathbf{B} - \frac{M_x \mathbf{i}' + M_y \mathbf{j}'}{T_2} - \frac{M_z - M_0}{T_1}\mathbf{k}' \ , \tag{I.33}$$

where $\mathbf{M}$ is a vector describing the macroscopic magnetisation of the sample, $\mathbf{B}$ is the overall magnetic field acting upon the sample, $M_{x,y,z}$ are the magnetisation components in their respective axes, M_0 is the magnetisation along the z-axis at equilibrium when the RF field is turned off, T_1 is the longitudinal relaxation time constant and T_2 is the transverse relaxation time constant.

The T_2 term in equation I.15 refers to the transverse relaxation of the atoms in the x-y plane, or phase decoherence of the spins, mainly due to spin-wall or spin-spin collisions. The T_1 term describes the longitudinal relaxation of the ensemble towards M_0.

The steady state solutions of the precessing magnetisation are easier to derive in the rotating frame, which is achieved by using a transformation, whereby the x-y plane is rotating around M_0 at a frequency ω_{rf}, which is the RF field frequency. In the rotating frame, the effective field is

$$\mathbf{B}_{\text{eff}} = \left(B_0 + \frac{\omega_{rf}}{\gamma}\right)\mathbf{k} + B_1\mathbf{i} \ , \tag{I.34}$$

where B_1 is the magnetic field imposed on the sample by the RF source.

Since in the rotating frame $B_0 = \dfrac{\omega_0}{-\gamma}$, and $B_1 = \dfrac{\omega_1}{-\gamma}$,the Bloch equation becomes:

$$\frac{d\mathbf{M}}{dt} = \gamma\mathbf{M} \times \left(\frac{\Delta\omega\mathbf{k} - \omega_1\mathbf{i}}{\gamma}\right) - \frac{\tilde{M}_x\mathbf{i} + \tilde{M}_y\mathbf{j}}{T_2} - \frac{M_z - M_0}{T_1}\mathbf{k} \ , \tag{I.35}$$

where $\Delta\omega$ is $\omega_{rf} - \omega_0$.

Setting $\dfrac{d\mathbf{M}}{dt} = 0$, we quote the steady state solutions of the Bloch equation for each component of the magnetisation vector, $\mathbf{M}$ [41]:

$$\tilde{M}_x = \frac{\Delta\omega\gamma B_1 T_2^2}{1 + (T_2\Delta\omega)^2 + \gamma^2 B_1^2 T_1 T_2} M_0 \ , \tag{I.36}$$

$$\tilde{M}_y = -\frac{\gamma B_1 T_2}{1 + (T_2\Delta\omega)^2 + \gamma^2 B_1^2 T_1 T_2} M_0 \ , \tag{I.37}$$

$$M_z = \frac{1 + (\Delta\omega T_2)^2}{1 + (T_2\Delta\omega)^2 + \gamma^2 B_1^2 T_1 T_2} M_0 \ , \tag{I.38}$$

Transforming back into the laboratory frame, the x and y components of the magnetisation vector may be recovered [41]:

$$M_x = \tilde{M}_x \cos(\omega t) - \tilde{M}_y \sin(\omega t) \ , \tag{I.39}$$

$$M_y = \tilde{M}_x \sin(\omega t) - \tilde{M}_y \cos(\omega t) \ , \tag{I.40}$$

In the case of the RF magnetometer, $\Delta\omega = 0$ at exact resonance since the RF frequency must be tuned to the Zeeman splitting set by the static DC field (See Chapter III 2.9 Induction Coil). Substitution of I.18 and I.19 into I.21 and I.22 respectively generates components of the magnetisation in the laboratory frame in terms of the magnetic field due to the RF field:

$$M_x = \frac{\gamma B_1 T_2}{1 + \gamma^2 B_1^2 T_1 T_2} M_0 \sin(\omega t) \ , \tag{I.41}$$

$$M_y = \frac{\gamma B_1 T_2}{1 + \gamma^2 B_1^2 T_1 T_2} M_0 \cos(\omega t) \ , \tag{I.42}$$

$$M_z = \frac{1}{1 + \gamma^2 B_1^2 T_1 T_2} M_0 \ , \tag{I.43}$$

When a spin polarisation is created and an orthogonal RF field of frequency ω is applied the magnetisation vector rotates away from the z-axis by an angle ωt. The total magnetisation changes thanks to the now non-zero M_x and M_y components, which precess at the Larmor frequency about M_z.

4 Sensitivity of Atomic Magnetometers

Atomic magnetometer sensitivity is ultimately limited by sources of quantum and background/ mechanical noise, dependent on vapour density, and, as can be seen in subsequent equations, affected by spin relaxation mechanisms. The sensitivity of the device may be determined by considering five types of dominant noise acting on the atoms:

- Photon Shot Noise
- Spin Projection Noise
- AC Stark Shift
- Spin Exchange Collisions
- Environmental Noise

4.1 Photon Shot Noise

Photon shot noise is the variance in the number of photons arriving at different parts of the detector. One such theory for why this occurs may be attributed to the Hanbury Brown-Twiss effect, where photons do not arrive at the detector randomly, but in intermittent clusters [42]. Projections of the spin polarisation of the atomic sample are detected using a linearly polarised probe beam directed at a balanced polarimeter. The probe beam is transmitted through the atomic sample causing its polarisation vector to rotate; the photon shot noise is the uncertainty on the measurement of this angle [43]. This uncertainty translates as follows into a reduced version of the equation describing the limitation on the magnetic field sensitivity [44]:

$$\delta B_{\text{psn}} \propto \frac{1}{\sqrt{\delta N/\delta t \cdot \tau}} , \tag{I.44}$$

where N is the photon count at the diode and τ is the measurement time.

In practical terms, this source of noise may be mitigated by increasing the acquisition time.

4.2 Spin Projection Noise

Spin projection noise (sometimes referred to as atomic projection noise) is the uncertainty on the quantum measurement of the remaining total angular momentum components when an atom is polarised along one of the projections [45]. The subsequent contribution to the error in magnetic field measurement due to spin projection noise is [46]:

$$\delta B_{\text{spn}} = \frac{1}{\gamma}\sqrt{\frac{8}{F_z \text{n}_{\text{ad}} V T_2}} \tag{I.45}$$

where n_{ad} is the atomic density in volume V, the overlap of the pump and probe beams.

To improve sensitivity here, the spin relaxation time T_2 and atomic density should be optimised. The atomic density in the active measurement volume, V, can be increased by heating the cell. T_2 for the atoms can be increased with the addition of a buffer gas mixed in with the atomic vapour (see section III.2.4 Sensor), which slow down atom-wall collisions which would otherwise result in a random polarisation of the atomic ensemble [47]. Application of antirelaxation coatings to the cell wall, the first notable example of which being paraffin [48], allow the atom to bounce off the cell wall many times before losing spin coherence.

4.3 AC Stark Shift (Quantum Back Action)

The AC Stark shift can be considered as a 'virtual' magnetic field that arises from the interaction between the electrical field of a beam of transmitted near-resonant pump photons (or imperfectly linear polarisation of the probe) and the atomic sample [49]. The atoms behave as if this field were real and indeed precess about the total field from the contributions from both the bias field and the Stark shift, which introduces noise into the pure magnetometer response. This effect vanishes when the pump beam is on resonance or the probe beam fluctuations in linear polarisation are minimised [50].

4.4 Spin Exchange Collisions

Spin exchange collisions are so-called because they occur when the electron spin of two colliding atoms flips but their total electron spin [51] and individual nuclear spins are con-

served [52]. After the collision, the ground state hyperfine populations are redistributed, leading to a loss of spin coherence [53]. Spin exchange collisions have the effect of broadening the magnetic resonance line [54] since in the quantum picture, the different hyperfine states correspond to a different spin orientation.

4.5 Environmental Noise Sources

Compared to quantum sources of noise related to the hardware used in the experiment itself, external noise sources have the potential to affect the operation and sensitivity of the magnetometer much more strongly. Random mechanical vibrations from, for example, people walking around the lab during a period of measurement-taking can disturb the sensitive optical equipment, but this may be mitigated by using optical benches with structures in the tabletop that can damp the oscillations.

Noise from neighbouring experiments may be also considered if they are situated within a couple of metres of the magnetometer. In the case of the present work, an experiment requiring the switching on and off of high amplitude radio-frequency pulses and magnetic gradients notably reduced the magnetometer signal and distorted images.

Chapter II

Survey of Current Weak-Field Magnetometry Technology

Magnetometers may be classified, for example, according to their sensitivity, whether they provide scalar or vector measurements, or if their mechanism is based upon classical or quantum processes. This brief survey describes some of the main features of current state-of-the art technology (aside from optical atomic magnetometry) in weak-field magnetometry. Weak-field magnetometers are devices that can measure magnetic fields on the order of 1 mT or less [55]. As such, they are highly suited to a variety of applications which require measurements of extremely small magnetic fields compared to stray magnetic fields or magnetic background noise, and are employed extensively in the defence industry, geophysics and diagnostic medical imaging in particular. Some of the most sensitive magnetometers are discussed below.

1 Inductive Coil Magnetometer (ICM)

Inductive or Search Coil magnetometers are based on Faraday's law of induction. When the surface of the search coil is subjected to a magnetic field with a varying magnetic flux, an electro-motive force (EMF) is induced in the coil, which is dependent on the rate of change of flux and the number of turns in the coil [56]. Consequently, ICMs are capable of only detecting AC magnetic fields. From Faraday's law of induction, the EMF induced in the coil caused by a change in flux is [56]:

$$V = -nA\frac{dB}{dt} \ , \tag{II.1}$$

where V is the EMF induced, n is the number of turns in a coil of area A, and B is the magnetic field.

The sensitivity of the inductive coil magnetometer can be improved by increasing the EMF induced for a given magnetic field strength. This can be achieved by simply using a coil with a larger number of turns, or alternatively installing a metal core with a high relative permeability. The EMF induced in such a coil is [56]:

$$V = \mu_0 \mu_r n A \frac{dH}{dt} \ , \tag{II.2}$$

where μ_0 is the vacuum permeability of free space, μ_r is a dimensionless factor to describe the relative permeability (to the vacuum permeability) of the core material, and H is the magnetic field strength. Soft ferrite cores are usually chosen for this purpose since, depending on the choice of alloy, they can exhibit relative permeabilities of up to 5000 [57].

The sensitivity is variable depending on the geometry and composition of the coil, but modern ICMs have the potential to reach sensitivities on the order of $0.3pT/\sqrt{Hz}$ at 20 Hz [58]. Since sensitivity is limited by coil size, ICMs cannot be miniaturised if they are required to be extremely sensitive. In addition, installing a soft ferrite core manifests a non-linear response in the inductive coil system which eventually magnetically saturates [59]. The ICM is also sensitive to changes in temperature since the permeability of the ferrite core is affected by this.

Applications of the ICM are wide and hugely varied; they may for instance be used for the non-destructive evaluation of conductive materials to assess sub-surface imperfections (see: 'Magnetic Induction Tomography with OAMs'). They are also readily used for geological imaging, surveying and mapping; for example identifying a path of lava flow or charting masses of igneous rock. ICMs may be used to detect concealed metallic objects.

ICMs have also been used in the THEMIS cluster of NASA satellites, whose objective is to ascertain how and where magnetic substorms originate [60]. The device measures three orthogonal components of the field lines associated with a substorm in the Earth's magnetosphere.

2 Fluxgate Magnetometer

The fluxgate magnetometer is a classical magnetometer that consists of two parallel ferromagnetic cores with a separate coil wound around each in opposite directions. The first coil has an AC current running through it and is used to drive the ferrite cores through their hysteresis loops. A hysteresis loop plots the magnetic induction, B, of a material as a function of the magnetic field strength, H, it is subjected to. For a soft ferrite material, an initial increase in H due to application of a higher current results in a large

relative amplification in B, which eventually saturates when all the magnetic domains in the ferrite material have aligned [61]. Cycling through a hysteresis loop by increasing and successively reducing current causes the material to change state from magnetisation, to saturation, and then magnetisation in the opposite direction.

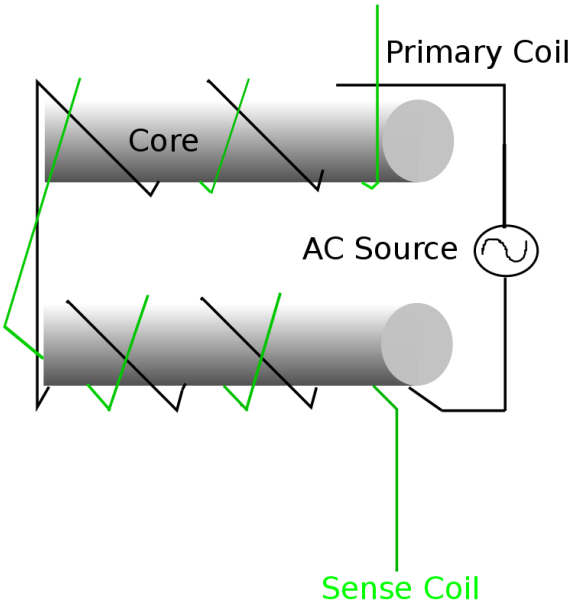

Figure II.1: The fluxgate magnetometer is a device that is capable of measuring both AC and DC magnetic fields. An AC current is applied to the primary coil, which due to Lenz's law, causes an equal current to flow through the sense coil. When there is a nearby external measurable magnetic field, there is a detectable difference in current between the two coils.

The changing magnetic state of the primary coil core gives rise to an EMF between the terminals of the secondary 'output' or 'sense' coil, as a result of the current induced in it by the primary coil [61]. Due to Lenz's law, the current induced in the sense coil will match the current through the primary coil. An external magnetic field acting on the magnetometer has the effect that the EMF of the primary and output coils are no longer balanced. The output EMF is proportional to the derivative of the magnetic flux, so unlike in the case of the ICM, it is capable of measuring DC fields as well as AC magnetic fields.

With the current operational sensitivity of the fluxgate magnetometer being $100\text{fT}/\sqrt{\text{Hz}}$ and the potential to reach $5\text{fT}/\sqrt{\text{Hz}}$ [62], this has recently opened up the possibility of using this device to perform magneto-cardiography (MCG) examinations, which are currently done using SQUIDs (see below). MCG scans are useful for mapping the magnetic fields as a result of the electrical activity of the heart, which can be used to localise cardiac arrhythmias, detect physical abnormalities and assess chest pain amongst other cardiac-related health complaints [63]. Other applications of the fluxgate magnetometer

are in a similar vein to the ICM, with the THEMIS mission also employing this type of magnetometer in its investigation.

The fluxgate magnetometer has the advantages that it is is robust, is operable at room temperature and can continuously record measurements. Both the ICM and fluxgate magnetometer can measure 3-dimensional components of magnetic fields by using a set of 3 coils on 3 orthogonal axes. However, as with the ICM, measurements with the fluxgate magnetometer are affected by temperature changes.

3 DC SQUID

A Superconducting QUantum Interference Device (SQUID) is a quantum magnetometer that comprises a thin-film metal alloy loop, which is bathed in liquid helium (at 4.2 K) or nitrogen (at 77 K) [64]. At this temperature, the loop becomes a superconductor and there is virtually no electrical resistance in the film.

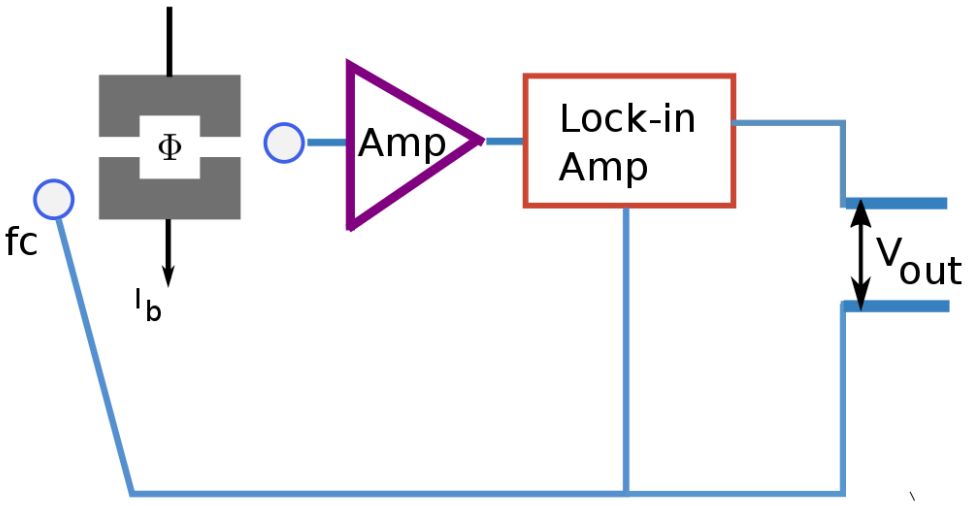

Figure II.2: Schematic simplified diagram of a DC SQUID magnetometer. A bias current, I_b is applied across the square coil leading to a phase change across the Josephson junctions. The flux across the coil is stabilised by means of a flux-locked loop, which is facilitated by a lock-in amplifier and feedback coil (fc). Small changes in flux can be determined by the voltage required to oppose the change.

In a DC SQUID, there are two parallel gaps, known as Josephson junctions, in the superconducting loop, which are usually constructed from Nb-AlOx-Nb for increased junction robustness [65]. Electrons may tunnel, even in the absence of a voltage, across the gap, resulting in a 'Supercurrent' flowing through the medium. There is a voltage difference across the junction when the current, I, through it passes I_c, the critical current.

The magnetic flux enclosed within the superconducting loop, Φ, is quantised in units of $\hbar/2e$ [64]. Upon application of a bias current I_b, to the loop, changes in magnetic flux result in a phase change across the junction, leading to an oscillating voltage with a period of Φ. The bias current is chosen to maximise the voltage amplitude so that the SQUID is able to detect smaller changes in magnetic flux.

A flux-locked loop is usually used to linearise the response of the SQUID to small changes in flux. An oscillating flux with an amplitude of $\Phi/2$ is applied to the SQUID by means of a coil and referenced to a lock-in amplifier. Integrating the signal and routing this back to the flux-producing coil creates a feedback system where small changes in flux are opposed, keeping the flux in the SQUID constant [65]. Hence, the SQUID measures flux, and the voltage output in response to measured changes in flux must be calibrated.

SQUID magnetometry has long been considered the gold-standard in ultra-sensitive magnetometry, with typical sensitivities of $5\text{fT}/\sqrt{\text{Hz}}$ [58]. However, there are many practical difficulties arising in design for use in the field. Aside from the cryogenic cooling requirement, another challenge that arises when operating SQUIDs is that due to its extreme sensitivity, there is significant magnetic noise affecting the quality of the output signal. These factors limit the potential of the SQUID.

SQUIDs have applications in medicine, one of which is magnetoencephalography (MEG). The SQUID is inductively coupled to around 300 second-order gradiometer coils, or sensors, attached to a helmet to be placed on the head [64]. This measures the change in flux as a a function of position. This is particularly useful to map brain function prior to tumour resection, or to localise the spikes in brain activity that cause seizures in some forms of epilepsy.

Similarly, SQUID gradiometer systems may be used to take magnetocardiography (MCG) measurements, which provide a picture of the magnetic field of the heart due to its electrical activity. Such recordings may be used to diagnose arrhythmias and ischaemia, but SQUID-based MCG devices are not widely used due to the need for magnetic shielding and their high operational costs [65].

SQUID magnetometers may also be used to measure the susceptibility of materials, for example for geophysical applications where this information is useful for determining how rocks or minerals were formed [66].

4 Giant Magneto-Resistive Sensor (GMRS)

The Giant Magneto-Resistive Sensor (GMRS) is a quantum sensing device based upon the mechanism by which it is named after. In a multi-layered ferromagnetic structure, the electronic spin polarisations between adjacent layers lie in anti-parallel directions. Cross-layer electron transport is hampered by increased probability of scattering due to the spin exchange, giving the structure magneto-resistance [67]. They have not been coined 'giant' because of their physical size, but rather due the strong magneto-resistive effect of the material. In the case of the GMRS, an external magnetic field is used to overcome the spin exchange between electrons in adjacent layers, aligning the magnetic domains [68]. The change in ohmic resistance can be used to detect an external field.

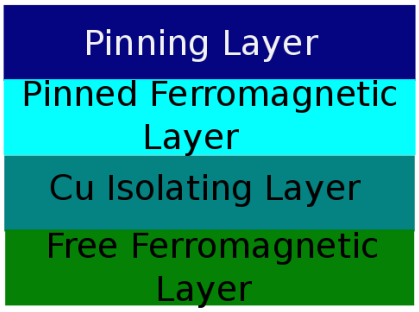

Figure II.3: Spin-valve Giant Magneto-resistive layer stack, with anti-ferromagnetic pinning layer to fix spin of adjacent ferromagnetic layer. The remaining ferromagnetic layer is free to rotate and able to align easily with the external magnetic field, reducing the electrical resistance between layers.

The most sensitive of this type of GMRS is the Spin-Valve sensor. It consists of a repeating stack of thin non-magnetic isolating layers sandwiched by a 4-6 nm thick layer of a ferromagnetic alloy (e.g. Fe-Co-Ni), with an anti-ferromagnetic 'pinning' layer on either face of the stack [69]. The pinning layer fixes the spins in the adjacent ferromagnetic layer, leaving the remaining ferromagnetic layer able to rotate to align easily with the external magnetic field. Electrons are able to tunnel through the thin layer with a higher probability when the magnetic domains are alligned parallel to each other. This changes the resistivity for a given magnetic field by around 200% for a MgO isolating layer [70],

compared with the relative change in resistivity of 10-20% for GMR sensors that do not utilise a spin-valve [71].

Spin-Valve GMR sensors are able to measure magnetic fields on the order of $10\text{pT}/\sqrt{\text{Hz}}$ [70]. They have successfully been used to detect super-paramagnetic nanoparticles; a result which could have an application in imaging brain function similar to the way that functional Magnetic Resonance Imaging (fMRI) is used. The nanoparticles could be used as a magnetic label to image the uptake of it by various tissue types [72]. This is particularly useful for providing evidence of neurological conditions

Commercial use of the GMR sensor is most common as a chip-scale integrated current monitor as an alternative to conventional ammeters. However, they are also being investigated for their viability to detect concealed conductive weapons. A 2-dimensional array of GMR sensors separated by 15 mm was used to discriminate between a handgun and other objects that are commonly carried about ones person. As a stand alone walk through detector, it was able to distinguish between the two objects but identification of the object from the GMR image alone was not possible [73].

5 Overhauser Magnetometer

The Overhauser Magnetometer is another quantum device that operates in a similar manner to proton precession magnetometers. In this type of magnetometer, the atoms of a proton-rich liquid such as methanol are used as the sensor [74]. The initial proton spin populations are randomly oriented, but upon application of a magnetic field, the fluid gains a macroscopic magnetisation as the spin-up population (spins parallel to the external field) is saturated. An RF 'deflection pulse' in an orthogonal direction is then applied, causing the proton spins to precess about the vector which is the sum of field due to the RF field and the external magentic field, at a frequency proportional to the total field strength [75].

The ratio of spin-up to spin-down protons is related to the sensitivity of the device. If there is a higher proportion of spin-up protons, the macroscopic magnetisation of the sensor fluid is larger for a given applied magnetic field. Consequently, the sensitivity improves since smaller changes in magnetic induction can be detected. The proton spin ratio is

$$\frac{N_+}{N_-} = \exp\left(-\hbar\,\omega_p / k_\text{B}\,T\right) \tag{II.3}$$

where ω_p is the proton resonance frequency.

The Overhauser magnetometer exploits the dipolar coupling between free electrons

and protons; the 'Overhauser effect'. In this case, the RF coil excites the electronic spin states, which, due to the weak coupling, in turn excite the nuclear spins [76]. This prepares the sensor fluid in a spin state which has the $\frac{N_+}{N_-}$ ratio of

$$\frac{N_+}{N_-} = \exp\left(-\hbar(\omega_e - \omega_p)/kT\right) \ , \tag{II.4}$$

where ω_e is the electron resonance frequency.

This ratio is larger in the Overhauser magnetometer compared with the up-down spin ratio in the absence of electron-nucleus coupling. The Overhauser magnetometer is around ten times more sensitive than a standard proton-precession magnetometer, with the capability of measuring fields on the order of 1 pT [76].

Owing to the low power consumption of the Overhauser magnetometer, long term unmanned deployment is possible. This is a particularly useful step towards operation of marine observation stations on the seafloor, which could be used to monitor tectonic plate movement and to probe beyond the Earth's mantle [74].

6 NV Centres in Diamonds

The Nitrogen Vacancy (NV) centre in diamond lattices is a point defect that consists of a nitrogen atom in place of a carbon atom neighbouring a vacancy. The NV centres may be neutral, negatively charged, or positively charged [77]. Only the NV^- vacancy is used since it has a magneto-optical spin triplet ground state, with a zero-field microwave splitting between the $m_s = +1, -1$ and $m_s = 0$ states [78]. The zero-field splitting arises due to the spin-spin interaction between electrons in the lattice.

When an external magnetic field B_{NV} acts on the defect, the $m_s = +1, -1$ states gain an energy separation of [79]

$$\Delta E = 2g\mu_B B_{\mathrm{NV}} \ , \tag{II.5}$$

where ΔE is the separation between the two previously degenerate states, g_J is the Landé g-factor, μ_B the Bohr magneton and B_{NV} the magnetic induction felt by the NV centre.

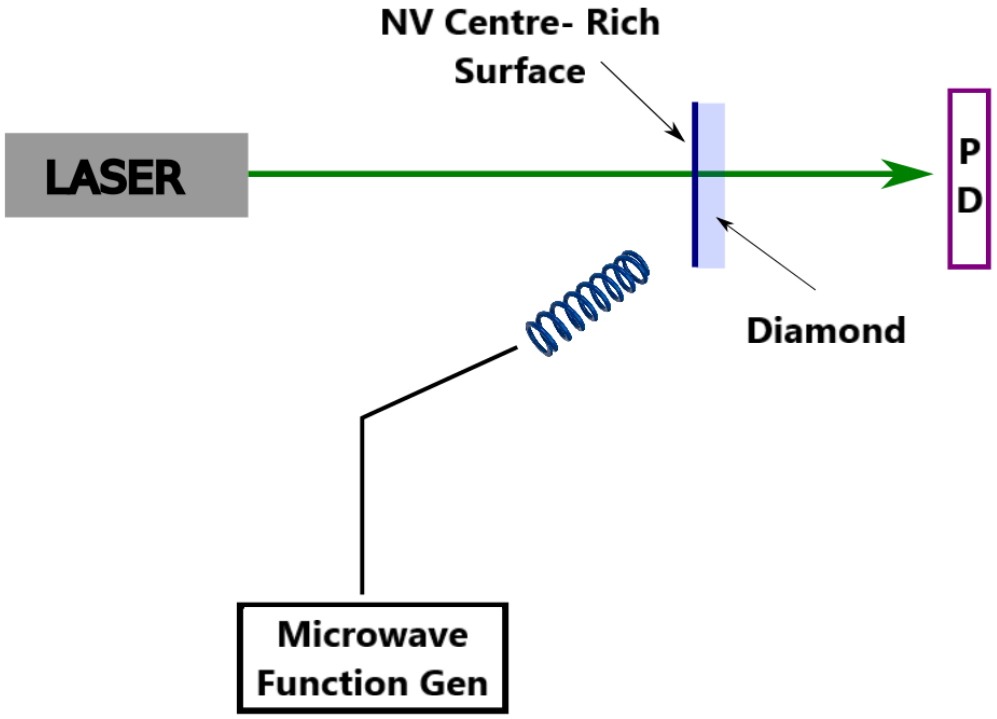

Figure II.4: Schematic Diagram to show how NV centres in diamond lattices may be used with Optically Detected Magnetic Resonance (ODMR) to detect magnetic fields. The sample is prepared in a magnetically active spin state by the green laser and irradiated by a microwave field sweep provided by the coil. A low noise, high-bandwidth photodiode is used to monitor the beam intensity.

The energy separation may be probed using a technique called Optically Detected Magnetic Resonance (ODMR) whereby the sample is irradiated with a microwave-frequency sweep. As the frequency reaches a resonance for either the $m_s = +1$ or $m_s = -1$ excitation, there is a corresponding dip in the green laser beam intensity [80], monitored using a low noise, high bandwidth, photodiode. Measuring the separation of the two dips in the spectrum may be used with equation II.5 to find B_{NV}.

The NV centre as a magnetometer is best suited to sensing at the nano-scale and has applications in individual spin detection and imaging single molecules [78]. It has a sensitivity anywhere between $30 \rightarrow 4.3$ nT/$\sqrt{\text{Hz}}$ [81].

7 Practical Applications and Advantages of OAMs

Since the mechanism of the RF-OAM operation was dealt with in the previous chapter, here the merits of OAMs will be discussed. One of the main draws of alkali-metal vapour magnetometers is that they have been shown to reach sensitivities between $1 fT/\sqrt{Hz}$ and

$0.01fT/\sqrt{Hz}$ [10]. This outperforms SQUID magnetometry [13] which, until recently, was the state-of-the art detection system for weak magnetic fields.

The potential for miniaturisation of OAMs with the advent of micro-fabricated vapour cells is an additional merit of their use. Chip-scale magnetometers (CSAMs) developed at the National Institute of Standards and Technology (NIST) have a sensor unit volume of just 1 cm^3 [82]. They are constructed using a technique which sandwiches a thin wafer of borosilicate between plates of silicate; using wet chemical etching to make a hole in the borosilicate layer a sealed cavity for alkali atoms is formed between the wafers [83]. Construction of micro-fabricated CSAMs in smaller and more portable configurations makes remote imaging more accessible.

Other practical advantages include the possibility of operation of OAMs at room temperature with no need for shielding, at least for specific classes of OAMs such as the radio-frequency (RF) OAMs described in subsequent chapters. The relationship between the Larmor precession of the atoms and the magnetic field strength (see equation I.1) relies only on a fundamental constant – the gyromagnetic ratio. Hence, the device does not require calibration.

OAMs may be configured to operate in a similar manner to conventional MIT (see chapter III.1), with the pickup coil being replaced by an alkali vapour cell that behaves as a sensor. The bandwidth of the OAM is not limited in the same way that using pickup coils used for MIT are. In fact, the OAM device used in the MIT modality (OAMMIT) was successful in obtaining images between operational frequencies of 300 Hz $\rightarrow$ 1 MHz. This may be credited to the fact that the precession of atoms in the Rb cells occurs with practically no inertia.

OAMs may be up to 10^7 times more sensitive in the low frequency regime (when driving the system at frequencies below 50 MHz) than a pickup coil of the same volume [84]. Along with the ability to physically down-scale the magnetometer to micro-sizes, OAMs also have improved function at this scale compared with MIT.

OAMs, when operated in the MIT modality, do not require background subtraction post data acquisition or image processing. In fact, the build up of data as the image is being acquired can be viewed immediately. This is particularly advantageous for real time imaging, potentially for airport security imaging.

7.1 Applications in Industry and Defence

Remote detection has much potential in the defence industry; one such example being the localisation of buried unexploded objects (landmines and improvised explosive devices). OAMs have also been shown to be effective at through-wall detection of rotating machinery

[85], so can be used to remotely determine if there is operational machinery inside a building. This information may be particularly valuable in defence and security. For generic industrial monitoring, this attribute of the OAM may be exploited to check the functionality and performance of motors.

The operating frequency of the OAM is also tunable, and thanks to the high bandwidth, can penetrate a wide range of materials at variable depths, which lends itself well to the task of discriminating between different materials. This can be used by security agents to determine whether banned or dangerous materials are being transported or held [86].

In the gas and oil industry OAMs are invaluable from a safety point of view. Magnetometers are currently employed to avoid drilling near fault zones, gas pockets, or old rigs. They are also used to check for cracks and fissures in pipelines in a procedure known as Non-Destructive Evaluation (NDE), which is extensively carried out across many other industries, for example, in aerospace engineering [87].

7.2 Biomagnetic Imaging

OAMs also have a promising future in biomagnetic imaging, with a view to eventually replacing SQUID in Magneto-Encephalography (MEG) or Mageneto-Cardiography (MCG) recordings [88]. Another possible application of MIT is to map spatially the conductivity of the heart in order better to understand diseases or pathologies as a result of conduction anomalies, and looks to be a useful tool when used with OAMs [89].

OAMs can also be used to detect Nuclear Magnetic resonance (NMR) signals in place of pickup coils. However, large magnetic fields are needed since the signal is proportional to B^2 [90] and due to issues with chemical shift in identical nuclei (discreprancy in measured precessional frequency). With this comes the caveat that the strong field will exert a force on ferromagnetic implants, replacement joints or pacemakers, causing further damage.

OAMs are an exciting candidate as a detector for low-field NMR thanks to the earlier point about good sensitivity in the low frequency regime. This paves the way for improvements in existing applications of NMR in medicine [87]- Magnetic Resonance Imaging (MRI) to map the brain structure and depict underlying pathologies where these are associated with the presence or absence of iron. Examples of this include providing evidence of neurological conditions such as brain trauma, haemorrhages, cerebral stroke and Parkinson's disease.

7.3 Earth and Space

The detection of slowly varying terrestrial magnetic fields is best achieved by a satellite-mounted magnetometer with extreme sensitivity to avoid local noise contributions [91]. Microfabrication techniques for OAMs ensure low power consumption and the ability to maintain high accuracy at low frequencies making them suitable candidates for measuring magnetic fields in space (interplanetary magnetic fields being typically on the order of 1 Hz) [92].

Of specific interest in this area, and becoming increasingly relevant since it can provide indicators for climate change [93], is the monitoring of ocean currents from space [94]. Ocean currents generate secondary magnetic fields as a response to the magnetic field experienced as they flow across Earth. However, satellite based magnetometers present a number of additional challenges – the OAM must be able to withstand exposure to increased radiation levels, temperature changes, and variation in orientation.

A cheaper and more accessible technique to monitor diurnal geophysical magnetic fields is remote terrestrial magnetometry using OAMs [91]. A ground-based telescope is used to optically pump mesospheric sodium atoms so that they become spin-polarised perpendicular to the local geomagnetic field. The polarisation results in a dramatic increase in fluorescence intensity of the D2 line, which is detected approximately 100 km from the pumping laser.

Chapter III

Magnetic Induction Tomography with OAMs

1 Magnetic Induction Tomography

Magnetic Induction Tomography (MIT) is a non-destructive technique to map the electromagnetic properties of a material by means of a magnetic field generated by an 'induction' coil.

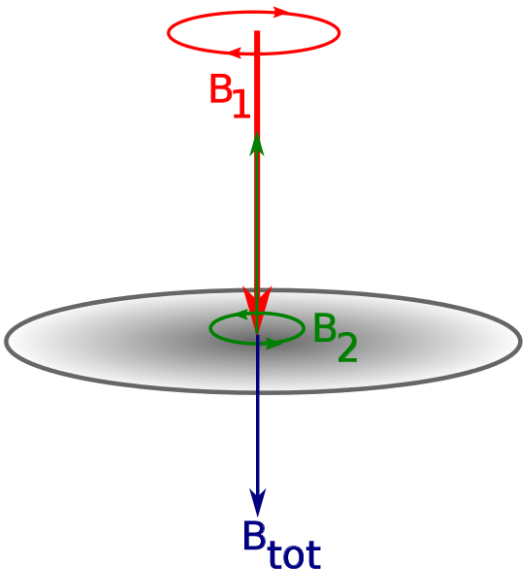

Figure III.1: The red current loop illustrates how the induction of a magnetic field, $\mathbf{B}_1$, by means of a coil with an AC current passed along it, induces eddy currents (shown in blue) in a conductive object.

The induction coil, with magnetic field $\mathbf{B}_1$, excites eddy currents in the target, which circulate on its surface. In response, a magnetic field $\mathbf{B}_2$ is generated by the eddy currents. Pickup coils placed in the vicinity of the target detect $B_{\mathbf{tot}}$ which is a vector sum of the two magnetic fields. The driving field and the field induced by the target are related by equation III.1 [95],

$$\frac{B_2}{B_1} \propto \omega(\omega\epsilon_0\epsilon_r - j\sigma) \tag{III.1}$$

where ω is the frequency supplied to the induction coil and applies when the skin depth is larger than the thickness of a target object which is composed of non-magnetic material. The skin depth is a measure of the distribution properties of current density in a conducting material and in this case is largely dependent on the inherent properties of the material itself and the frequency supplied to the induction coil. The eddy currents circulate mainly on the surface of the material for a certain width- this is the skin depth. The skin depth is explored more in equation III.8.

The phase lag of this signal and the magnitude of $\mathbf{B}_2$ give information about the conductivity (σ) and relative permittivity (ϵ_r) of the sample and can be mapped by taking position-resolved measurements. Since the conductivity measurement is purely imaginary, it is most accurately represented by mapping the phase retardation of $\mathbf{B}_2$.

There are some limitations that arise from using coils to both induce eddy currents and detect them; one of which is that they can exhibit a low sensitivity at low frequencies when the coil size is a restriction on the device design. Furthermore, capacitive coupling of pickup and induction coils in close proximity results in measurements that do not accurately reflect the properties of the sample [95]. Another drawback due to the use of pickup coils is their limited tunability, which reduces the range of frequencies and, by extension, materials that can be explored.

2 Optical Components and Electronics

We propose to overcome such limitations with the use of OAMs, whose characteristics allow one to outperform conventional MIT systems, as demonstrated in the following chapters. A diagram of the components required to build the OAMMIT, by using an RF optical magnetometer, is shown below, in figure III.2. All of the optical components are bolted onto an optical table shown by a large square rectangle with electrical devices securely positioned in the vicinity.

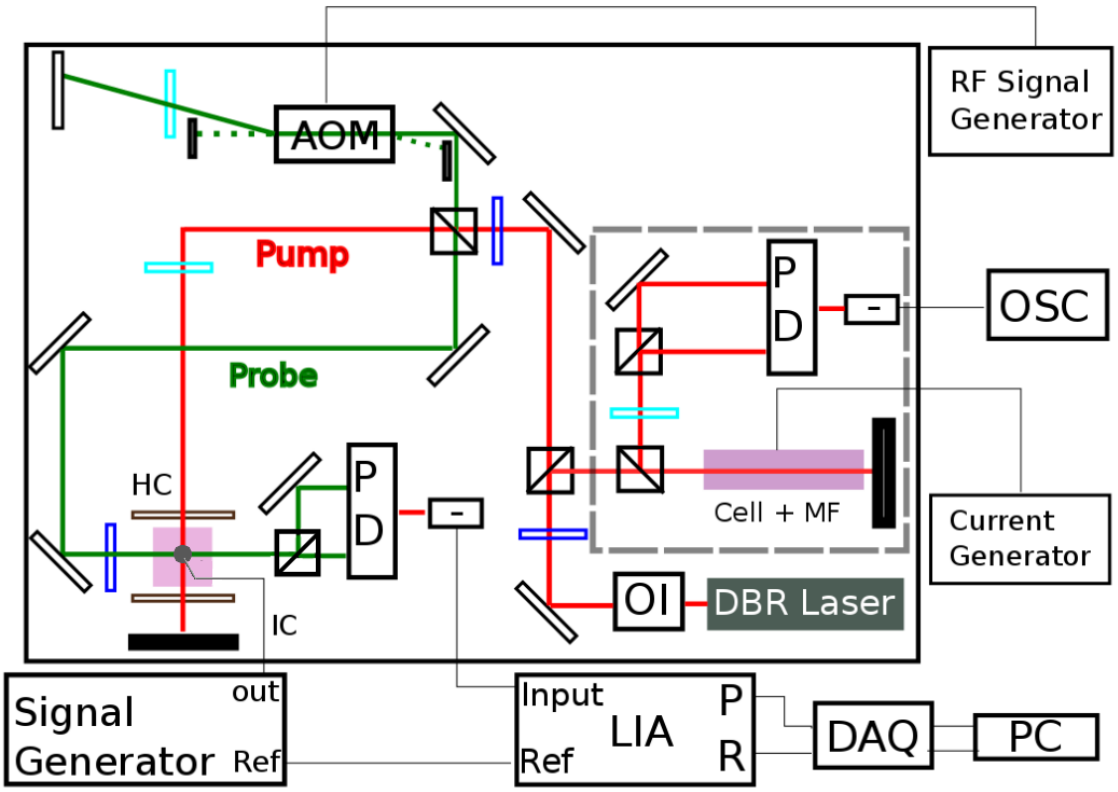

Figure III.2: Arrangement of optical components on table, the electronics, and the connections between them. Key: OI is an Optical Isolator, MF is a magnetic field, PD is a balanced Photodiode, OSC is an oscilloscope, AOM is an Acousto-Optical Modulator, IC the 'Induction Coil', HC a Helmholtz Coil pair, LIA is a Lock-In Amplifier and the DAQ is the Data Acquisition device connected to a Personal Computer (PC). The turquoise and dark blue structures in the beam path refer to $\frac{\lambda}{4}$ and $\frac{\lambda}{2}$ waveplates respectively. The sensing cell filled with a natural mixture of ^{87}Rb and ^{85}Rb is in the location of the intersection of the pump and probe beams, sandwiched between the Helmholtz coils. The DAVLL is the area bounded by the grey dashed square; there is a second cylindrical Rb cell encircled by a coil that is connected by a current generator in order to supply a magnetic field to the area surrounding this cell.

The laser output (red line) is provided by a Distributed Bragg Reflector (DBR) laser (replaced at a later stage) and is the same laser source for the Dichroic Atomic Vapour Laser Lock (DAVLL), pump beam, and probe beam. The constituent parts of the DAVLL system are bounded by a grey dashed square. The probe and pump beams are split using a polarising beam splitter and their intensities are controlled by $\frac{\lambda}{2}$ waveplate. The functions of the hardware and their mechanism will be explained further in subsequent sections.

2.1 DBR Laser

A Distributed Bragg Reflector (DBR) Laser is a short cavity laser with a Bragg mirror at one or both ends of the optical gain section of the laser. The short cavity of the DBR laser provides a wide tunability [96], with the Bragg mirrors responsible for a relatively low insensitivity to external vibrations compared with Extended Cavity Diode Lasers [97].

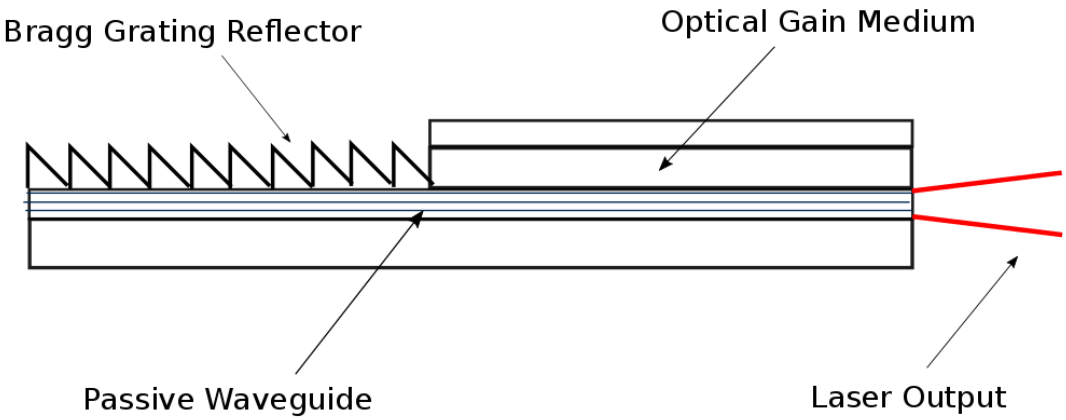

Figure III.3: Diagram illustrating optical components as part of a Distributed Bragg Reflector Laser module.

The Bragg mirrors are spaced regularly so that upon exiting the laser cavity the wave-fronts have constructively interfered; with the dominant wavelength being the Bragg Wavelength. This wavelength is characterised by [97] the equation

$$\lambda_b = \frac{2\Lambda\eta_{\text{eff}}}{M} \,, \tag{III.2}$$

where λ_b is the Bragg wavelength of reinforced reflections along the waveguide, Λ is the spacing between the Bragg reflector 'teeth' and η_{eff} is the effective refractive index throughout the waveguide.

The reinforced Bragg reflections result in a single frequency output of the laser which is highly stable. The laser can be tuned to select frequencies over a range of 40 GHz [96] by changing the injection current provided to the laser or the temperature of the laser

module. This changes the refractive index in the waveguide medium which in turn alters the Bragg wavelength [97].

2.2 Optical Isolator

The optical isolator is installed just after the DBR laser output to prevent unwanted feedback into the laser cavity. The premise behind this is that light of a certain polarisation can be transmitted in one direction but not back through the other [98]. The optical isolator installed in this scheme relies on the Faraday effect to achieve this.

The isolator works because only polarisation of a certain direction may be transmitted initially through it. When the beam is propagated in the forward direction, it is vertically polarised by the Isolator, then the plane of polarisation is rotated by an angle [99]

$$\theta = VHL \tag{III.3}$$

where V, the Verdet Constant is a constant related to how effective the Faraday rotation is for a material, H is the magnetic field applied along the length of the isolator and L is the path length i.e. the distance travelled by the beam through the optical isolator. For ease, this is usually chosen so that θ is 45^o.

The plane rotates counter-clockwise in this direction and is allowed to exit the optical isolator normally. Any reflections entering the isolator from the other side, towards the laser, are rotated a further 45^o by the rotator, so are blocked by the vertical polariser.

2.3 Dichroic Atomic Vapour Laser-Lock

The lasing frequency of lasers, including DBR lasers, are prone to slight drifting due to changes in the ambient temperature and current supply. The Dichroic Atomic Vapour Laser-Lock (DAVLL) is a tool to stabilise the chosen laser frequency and its components are bounded by the grey dashed line in figure III.2. The DBR laser is able to remain at a chosen frequency for around 10 hours with the DAVLL [10].

After passing through the optical isolator, a small fraction of the beam (of power 2 mW) is directed towards and passed through a cylindrical glass cell filled with rubidium vapour, with a magnetic field applied along the axis of beam propagation by means of a coil wrapped around the cell. The beam is reflected back through the cell along the original beam path in order to resolve the hyperfine structures using Doppler-free spectroscopy.

Linearly polarized light can be alternatively imagined to be a superposition of right-circularly and left-circularly polarised light. The polarising beam splitter cube placed just after the quarter waveplate in the DAVLL section of the optical table decomposes the linearly polarised beam into two orthogonal counter-rotating circularly polarised beams.

This linearly polarised beam interacts with the atoms in different ways depending on the handedness of the polarisation, and absorption can excite atoms since the degeneracy in the hyperfine levels is lifted thanks to the applied magnetic field. Absorption of σ_+ circularly polarised light provides $g\mu_B B$ of energy to an atom causing a transition from |F,m$_F$> $\rightarrow$ |F',m$_F + 1$>[100].

The two beams are directed at a balanced photodiode, measuring the two orthogonal components of the light's polarisation. The two components are separated by $2g\mu_B B$. The output of the difference channel of the photodiode is illustrated in figure III.4.

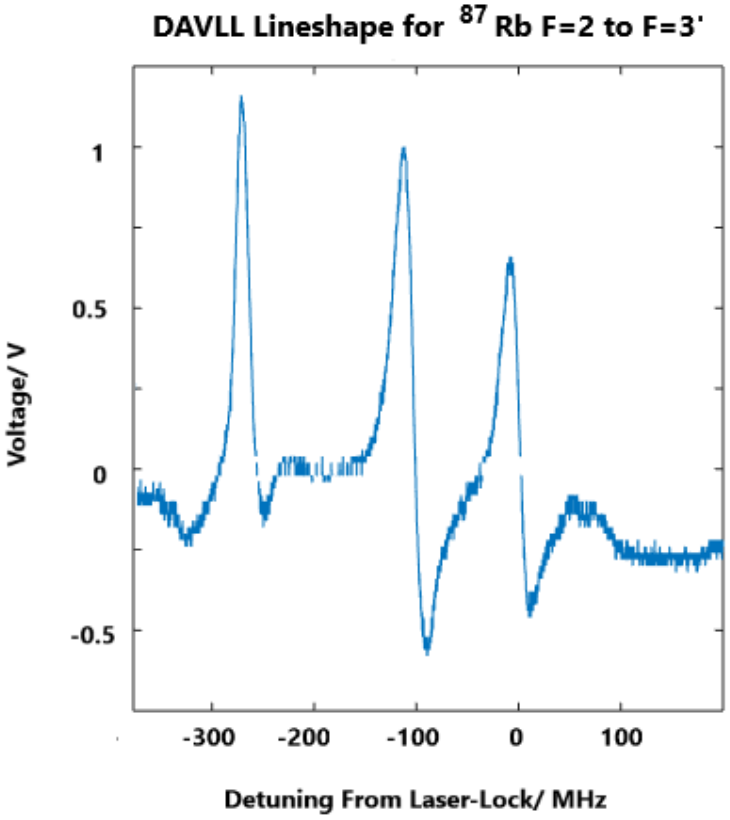

Figure III.4: Doppler Free DAVLL signal ^{87}Rb. This error signal is fed back to the laser module in order to stabilise and lock the frequency to a transition.

This is the error signal for the laser reference. As the ramp of the laser current sweep is reduced, so the gradient of the straight line between the peaks decreases. The chosen transition should be 'locked' to the zero crossing of the DC voltage at the centre of the line. This stabilises the wavelength of the emitted laser beam to the desired hyperfine component of the 780 nm transition (see figure I.6), in this case, the F=2 $\rightarrow$ F'=3 transition. This transition is chosen since it has the largest transition probability and therefore the greatest pumping efficiency. The straight line peaks are necessary for good feedback facilitation since a straight line provides a simple, linear relationship between the measured

frequency and the required frequency.

2.4 Sensor

The rubidium cell surrounded by the Helmholtz coil pair acts as the sensor. The one used in this experiment is a 25 - mm - sided quartz cube, containing a natural mixture of ^{87}Rb and ^{85}Rb at room temperature, which corresponds to a density of 7x10^{10}cm^{-3}. The cell also contains 20 Torr of Nitrogen gas, which acts as a buffer gas.

Figure III.5: Cubic Quartz Rubidium Cell. Shape allows for cross-configuration of pump and probe beam.

Nitrogen serves to reduce the speed of atomic diffusion and reduce the number of atomic collisions with the cell wall, increasing the lifetime of the spin state of the atoms. Consequently, the laser-atom interaction time is increased, improving the signal to noise ratio of the OAM.

2.5 Helmholtz Coils

A hand-constructed circular Helmholtz coil pair made from 0.5 mm diameter copper wire with dimensions:

- Average Radius R= 4.25 cm
- N=50 turns
- Separation= 4.25 cm

are used to generate the static homogeneous magnetic field source for the optical pumping stage. From the Biot-Savart Law, one can determine the distance at which the Helmholtz coils should be separated in order to achieve a uniform magnetic field between them. Symmetry is achieved as long as the current through both coils is flowing in the same direction. The magnetic field through a current-carrying loop of wire, with z chosen to be

the axis along the optical pumping axis, is

$$B(z) = \frac{\mu I}{2} \frac{R^2}{(R^2 + z^2)^{3/2}} \tag{III.4}$$

For a set of Helmholtz coils with N turns which are a distance R apart, with the point bisecting the line along $\mathbf{B}_z$ at exactly half way between the coils being $z = 0$, the total field is the sum of the contributions from both coils:

$$B_{tot}(z) = \frac{1}{2} R^2 \left(\frac{1}{R^2 + \left(\frac{-R}{2} + z^2\right)^{3/2}} + \frac{1}{R^2 + \left(\frac{R}{2} + z^2\right)^{3/2}} \right) \mu N I \tag{III.5}$$

The second derivative of this function gives information about where the minimum of this field gradient lies (i.e where it is most homogeneous), and from figure III.6 it is clear that this is at z=0.

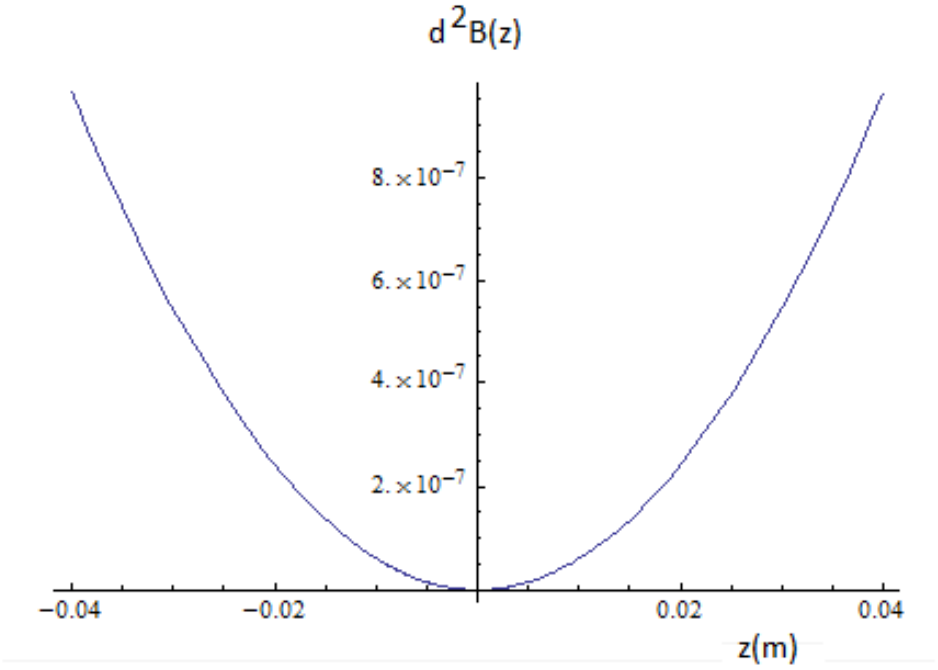

Figure III.6: Function to describe the second derivative of the magnetic field lines between a Helmholtz coil pair with it N=50 and Radius= 0.0425 m, where z=0 is the point equidistant between the coils.

The homogeneity of this field can be illustrated by figure III.7 which plots the magnetic field strength at a point along z compared to the maximum field strength at z=0. The magnetic field is fairly uniform at approximately 2 cm either side of z=0. As the Rb cell has L= 2.5 cm, carefully centering it on z=0 ensures that the field variation within the cell is minimised.

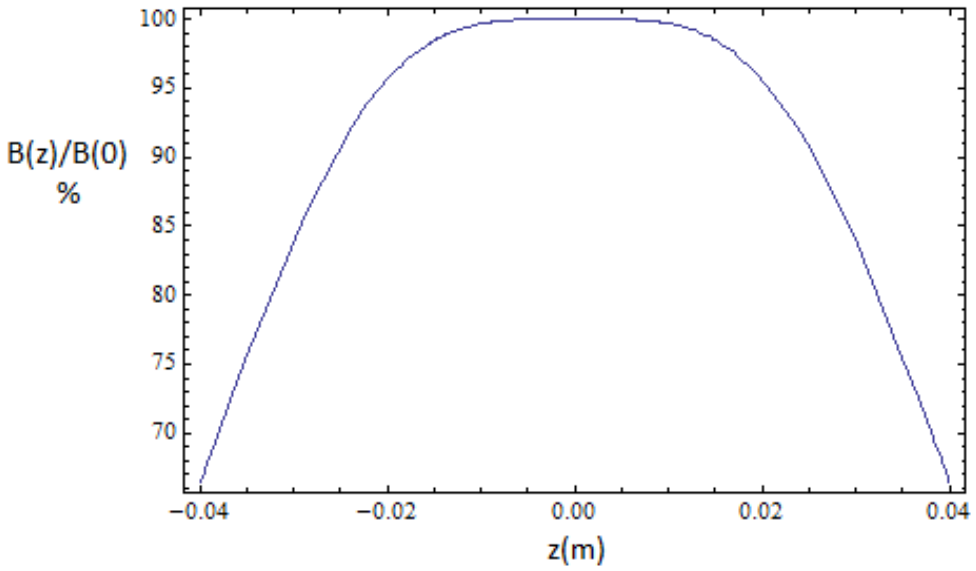

Figure III.7: Variation of the Magnetic field along the z-axis between the Helmholtz coils.

2.6 Pump Beam

The pump beam is directed along the z-direction (parallel to the DC Helmholtz field) for efficient optical pumping and locked to the F=2 to F'=3 transition on the D_2 line at 780 nm. It is 5 mm in diameter with a power of 15 mW, and it is circularly polarised to a >95% degree using a $\frac{\lambda}{4}$ waveplate. The best positioning for effective homogeneous polarisation of spins is to illuminate the cell in the centre where the field gradient is minimised (see figure III.7).

2.7 Acousto-Optical Modulator

By passing the probe beam through an acousto-optical modulator (AOM), the beam may be detuned from its resonant frequency thanks to the acousto-optic effect. This begins with a piezo-electric transducer (PZT), which vibrates, compressing and stretching, when an electric field is applied [101].

The PZT is in contact with a Lithium Niobate crystal, whose refractive index changes under an applied strain [102]. As a result of the propagation of sound waves from the PZT to the crystal, the refractive index of the crystal varies between alternating peaks and minima.

Once the probe beam is aligned properly through the crystal, it is diffracted by the sound waves by an angle [103]

$$\sin\theta_d = \frac{n\lambda}{2\Omega}\ , \tag{III.6}$$

where θ_d is the diffraction angle, n is the order, λ is the optical wavelength and Ω is the acoustic wavelength.

The diffraction of order n, due to the conservation of energy, destroys n phonons, and the frequency, f, of this order is given by [103]

$$\Delta f = \frac{mE_{\text{phonon}}}{h} \tag{III.7}$$

where E_{phonon} is the energy of the phonon and h is the planck constant.

2.8 Probe Beam

The probe beam is linearly polarised and the orientation of polarisation is controlled using a $\frac{\lambda}{2}$ waveplate. The probe beam must avoid pumping the medium or destroying optical pumping, to improve the signal to noise ratio [104]. There are two ways to reduce the influence of the probe beam; the first is to reduce the actual power in the probe beam. The second method reduces the interaction probability of the beam by detuning; in this case this is achieved by using an AOM, which diffracts the laser beam frequency. The beam is passed through the AOM once and the first order diffracted wave is reflected and directed back through the AOM a second time; this is called a double pass configuration [105]. This returns the first order of the double-passed beam to the original beam path. The AOM is set to diffract each order by 210 MHz, so that the total detuning of the probe beam is 420 MHz after it has passed through the AOM twice. The advantage of using the double pass configuration is that changing the detuning frequency does not alter the beam path, negating the need for realignment.

The pump and probe beams intersect orthogonally in a cross configuration. This means that their area of overlap is minimised. This smaller overlap potentially increases the spatial resolution of the MIT system since only local atomic spins are being interrogated by, or are sensitive to variations in $\mathbf{B_{tot}}$ at any one time. Ultimately, the spatial resolution of a magnetometer is limited by its size.

Once the probe beam has propagated through the cell, it contains information about the AC magnetisation of the sample from the precession of the atomic spins. There is an asymmetry in the extent to which the two circular polarisations are refracted when they interact with the atoms. This phenomenon is called circular birefringence and is responsible for a shift in the phase velocity between the two components of the beam, which is observed as a rotation in the plane of polarisation of the light [106]. The rotation can be measured using a half waveplate and polarising beamsplitter to observe the transverse

and longitudinal components of the beam separately, and from this information, find the phase difference between them NEED PAGE NUMBER [107].

2.9 Induction Coil

The Induction, or driving coil, has two main functions. The first is to drive the spin precession of atoms coherently. This is achieved by applying an AC magnetic Radio-Frequency field (RF) in a perpendicular plane to the static Helmholtz field (B_0), and has the strongest effect if the frequency of the RF field matches the Larmor frequency of the atoms [108]. If so, the atomic magnetic spins begin to rotate like a spinning top in an ever increasing circumference towards the axis along which the RF field is applied. The spin coherence is recovered when the atoms absorb a photon from the pump beam and are forced back towards the z-axis. This results in precession about a vector that is the sum of the B_{textrf} and B_0.

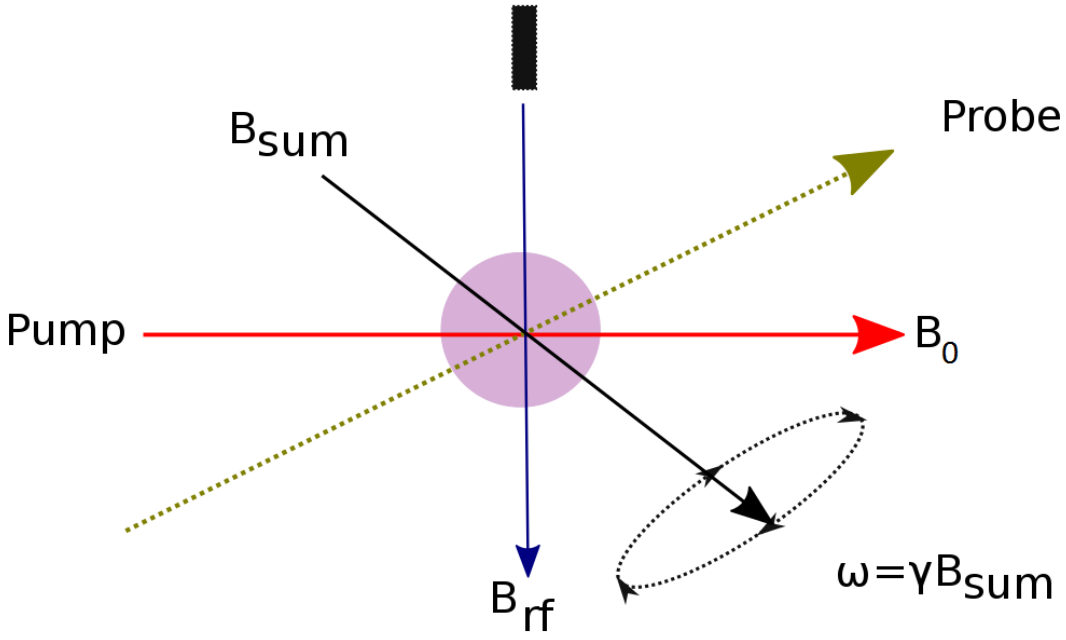

Figure III.8: Role of Induction coil in maintaining spin coherence of atomic population.

The second function of the driving coil is to induce eddy currents in the object of interest, much like an induction coil in conventional MIT configurations. The coil is placed in the vicinity of the target object with an AC current field supplied to it (see II.I for further detail).

A 'Multicomp' ferrite core coil was used with:

- Height= 7.80 ± 0.5 mm
- Coil Diameter = 9.50 ± 0.5 mm
- DC Resistance = 1.4 Ohm

The skin depth δ for conductive materials can be calculated using the following equation [109]:

$$\delta = \sqrt{\frac{2}{\omega \mu_0 \sigma}} \,, \tag{III.8}$$

where σ is the conductivity of the material at 273 K, μ_0 is the permeability of free space and ω frequency of the AC field affecting the object.

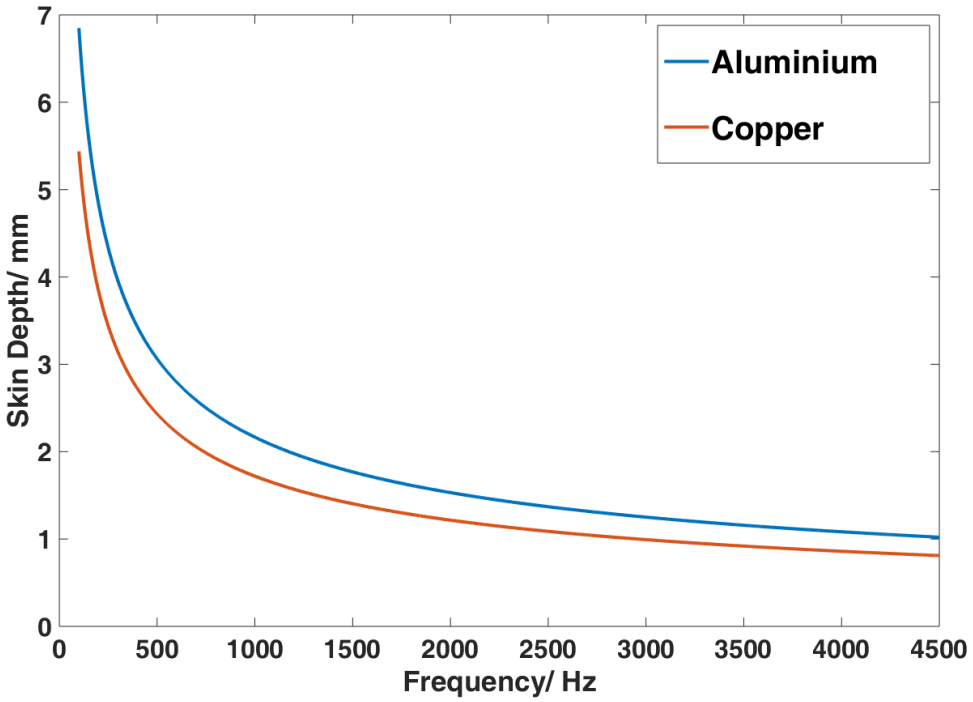

Figure III.9: Penetration depth through conductive materials as a function of frequency supplied to induction coil for copper ($\sigma = 63.694{*}10^6$S/m) and aluminium ($\sigma = 41.322{*}10^6$ S/m) samples [57].

The penetration depth through the object is larger at smaller frequencies. This may be used as a guide for finding the the correct operation frequency for a range of object thicknesses, and for objects concealed under metal sheets. Once the induction coil frequency has been selected, the correct current should be supplied to the Helmholtz coil.

2.10 Lock-in Amplifier

The signal from the probe beam at the photodiode is due to the total magnetic field acting upon the OAM unit; that is to say it contains information about the driving field due to the induction coil, the static field due to the Helmholtz coils and, finally, the signal due to eddy currents circulating in the target itself. A lock-in amplifier (LIA) can be used to extract the useful information in the signal. The LIA extracts a signal at a particular frequency and amplifies this. In this instance, the reference frequency (or frequency that the LIA is 'locked to') is the frequency supplied to the driving coil.

Once the signal has been fed to the LIA, a bandpass filter is used to reduce the bandwidth of the signal in order to improve the signal processing capabilities of the LIA [110]. This signal is then mixed with the reference input.

To see how this works, consider an input signal:

$$V_{\text{in}} = A\cos(\omega_i t) \tag{III.9}$$

and a reference signal

$$V_{\text{ref}} = B\cos(\omega_r t + \phi) \tag{III.10}$$

Mixing these signals yields

$$V_{\text{in}}V_{\text{ref}} = \frac{AB}{2}\big[\cos(\omega_i t + \omega_r t + \phi) + \cos(\omega_i t - \omega_r t - \phi)\big] \tag{III.11}$$

$$V_{\text{in}}V_{\text{ref}} = \frac{AB}{2}\big[(\cos(\omega_i + \omega_r)t + \phi) + (\cos(\omega_i - \omega_r)t - \phi)\big] \tag{III.12}$$

Locking the signal input to the reference sets $\omega_r = \omega_i$, leaving

$$V_{\text{in}}V_{\text{ref}} = \frac{AB}{2}\cos 2(\omega_i t + \phi) - \frac{AB}{2}\cos\phi \tag{III.13}$$

Passing this signal through a low pass filter removes the $2(\omega_i t)$ component to leave a DC component of the form $\frac{AB}{2}\cos\phi$, where A is the magntiude of the signal of interest and ϕ is the phase lag with respect to the driving field.

3 OAM Characterisation

3.1 Helmholtz Coil Calibration

Functional operation of the OAMMIT is dependent on carefully matching the magnetic field provided by the DC field needed for optical pumping and the magnetic field due to the RF induction coil. These conditions can be set by operating the OAMMIT in a passive mode to find a known magnetic field, generated by a nearby square coil of sides $l = 150mm$.

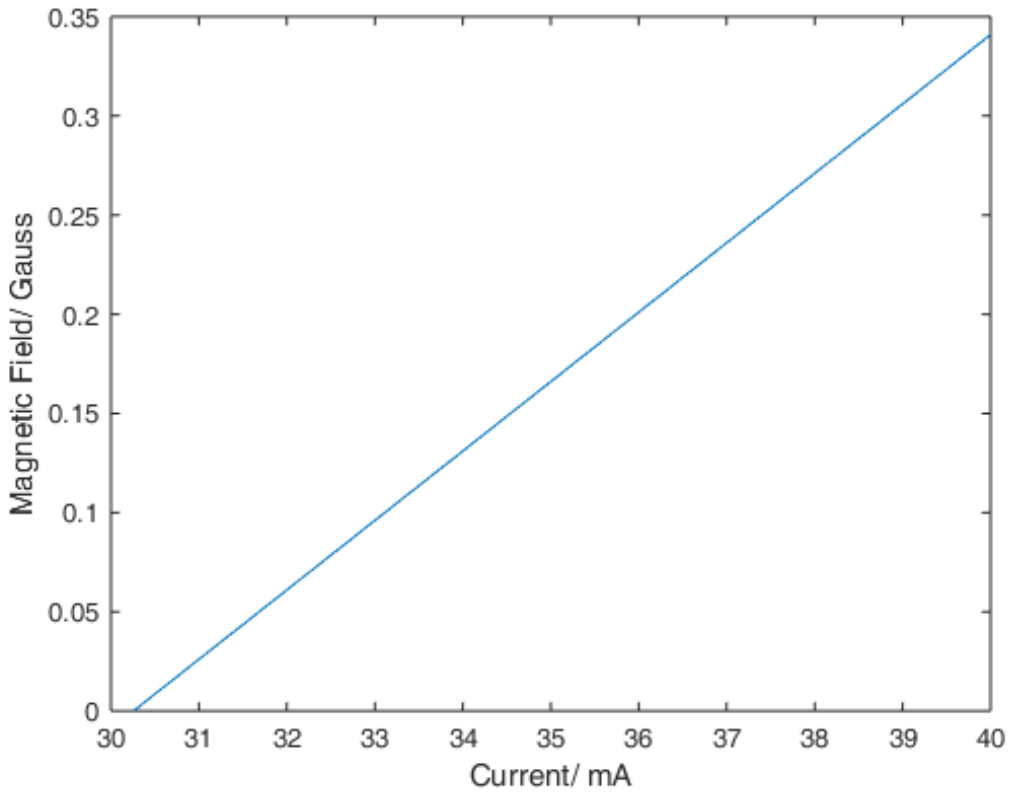

Figure III.10: Graph to show how Magnetic Field strength at centre of Helmholtz coils changes as a function of DC current supply.

By carefully changing the current supply and measuring the generated magnetic field using a hall probe, the linear nature of the response of the system is shown in figure III.10. In this way, once the current to be supplied to the Helmholtz coils has been set, the DC magnetic field acting upon the atoms can be inferred. Looking at III.10, there is a 'negative' magnetic field present when the coils are off. In real terms this indicates a stray magnetic field acting in the opposite direction to the one intended to be supplied by the Helmholtz coils, which is cancelled when the current supplied is set to 303.3 mA.

3.2 Resonant Frequency Response

After setting the static field, the frequency of the AC driving magnetic field is determined by the fact that the gyromagnetic ratio of the F=2 line is 0.7 MHz/G [28]. This constant sets the proportionality of the splitting between F=2 and neighbouring lines. So, application of magnetic field of $1.4 * 10^{-5}$ T (when the current through the Helmholtz coils is 35 mA) corresponds to a Zeeman splitting of 99 kHz between the F=2 and F'=3. To interact with this transition the driving frequency of the induction coil must also be set to 99 kHz.

To test the response of the OAM unit in this configuration, an additional coil whose

frequencies are swept, ν_{test}, is placed in the vicinity of the OAM and the polarimeter output at the lock-in amplifier is recorded. If the OAM is working correctly, the polarisation rotation or phase retardation of the probe beam should be at a maximum when the frequencies of both coils are at 99 kHz.

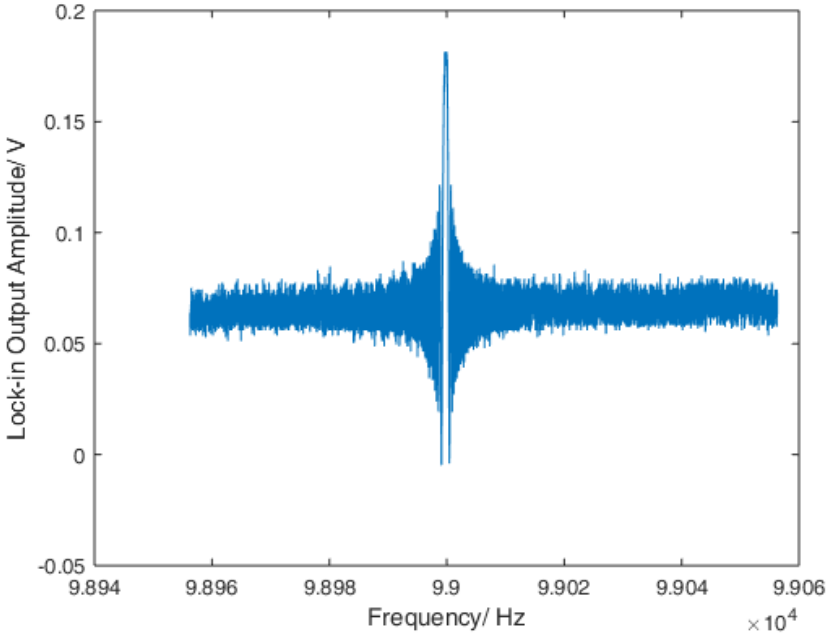

Figure III.11: Radio Frequency OAM resonant response when a known 99 kHz driving field is applied to the system and a 'test' coil sweeps a range of frequencies in order to 'find' the resonance.

When the frequencies of the driving coil and test coil are not matched, there is a small constant output at the LIA. When υ_{test}= 99 kHz there is a dramatically increased output at the LIA, suggesting that two AC fields at the same frequency behave like a single coil with a much larger amplitude than each individual coil. This demonstrates that the OAM can detect AC fields which may be generated by conductive objects.

3.3 Optimisation of Power Ratio Between Pump and Probe

The amplitude of the OAM response can be maximised by setting the ratio of the power between the pump and the probe beam; the pump must have sufficient power to saturate the excitation of the Rb atoms and the pump beam must have an intensity such that it does not perform any optical pumping. The beam intensity can be measured by a commercial photodiode powermeter. The relative intensities of the beams may be controlled by a $\frac{\lambda}{2}$ waveplate placed before a polarising beam splitter which can be rotated to change the power in the beams. The response of the OAM was monitored for a range of power ratios upto a point where the pump beam was 140 times more powerful than the probe beam.

The chosen ratio was set so that the intensity of the pump beam was increased by a factor of 10 compared with the probe beam as this elicited the strongest response from the magnetometer.

The probe beam detuning was set in a similar manner. By varying the frequency supplied to the AOM and monitoring the response of the OAM, the ascertained optimum detuning was 420 MHz. Since the setup is in a double pass configuration the actual frequency to the AOM is 210 MHz.

4 Outcomes and Images

Once the 'correct' working point for the OAMMIT has been identified and properly set, the OAMMIT's mode of operation is changed from 'passive' to 'active', in order to test whether detection and imaging of conductive objects is possible. The diagram below, figure III.12, illustrates the relative arrangements of the induction coil, test object and OAM unit. The aluminium test object has dimensions:

- Diameter = 37.00 mm
- Thickness = 1.98 mm

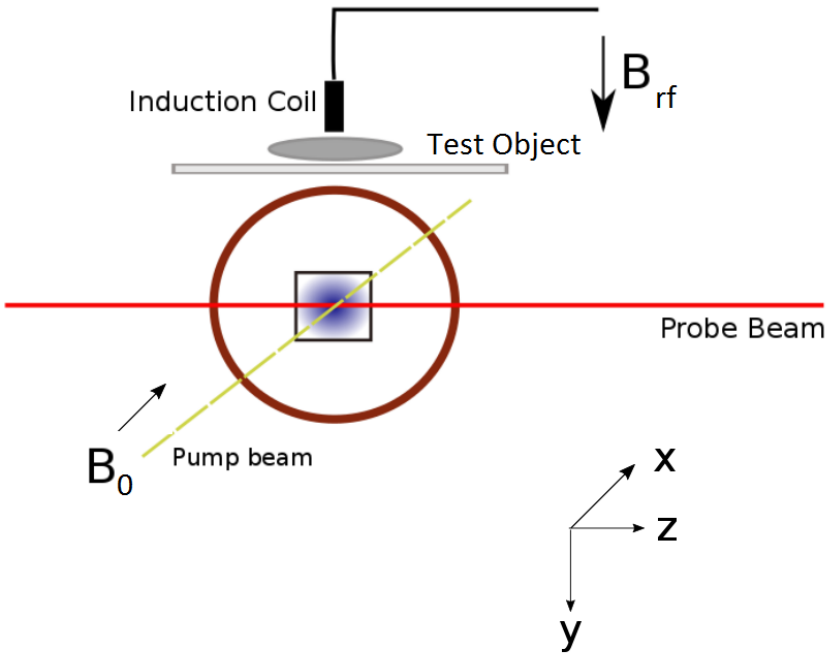

Figure III.12: Arrangement of OAM unit to describe position of components under test conditions; an aluminium disk is placed on a perspex support above the Rb cell. The induction coil is placed in the same line connecting the centrepoint of the aluminium disk to the central region of the cell where the pump and probe beams cross.

Initial investigations showed that the OAMMIT was able to detect the moving aluminium disk and clearly discriminate between absence and presence of the object. This is shown by the changing response of the magnetometer when different sections of the aluminium disk are positioned directly above the sensing region of the OAM i.e. where the pump and probe beams intersect. [1]

[1]Subsequent images and data collected in conjunction with Cameron Deans and Luca Marmugi.

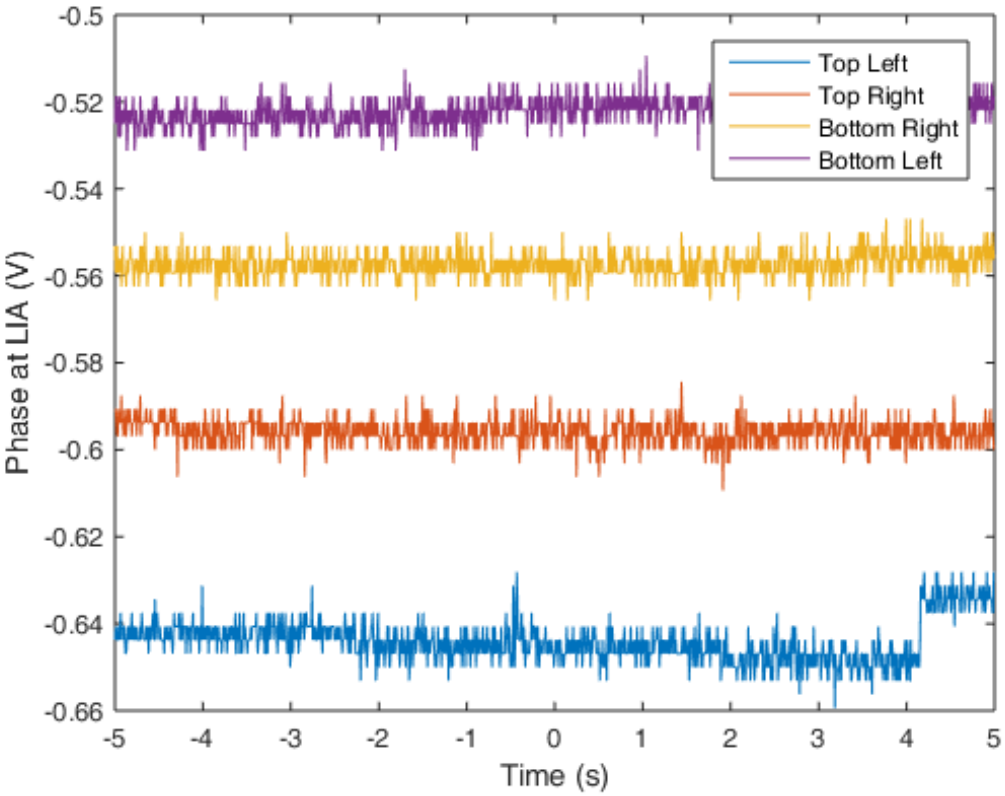

Figure III.13: Voltage changes at the Lock-in Amplifier output when the aluminium disk is moved so that different quadrants of it are being interrogated by the magnetometer

To generate a 2D image of the object, the frequency supplied to the induction coil can be varied to image thicker or thinner objects, or to choose between imaging the surface or subsurface. The relative position of the object and sensing region in the x-z plane is varied by using a perspex mount attached to a translation stage whose movements are controlled by hand rotation of micrometer screws. The object can also be moved in the y plane by adjusting the height of the perspex mount.

At each position of the object (determined by a small camera attached to a laptop), 1000 averages are taken of the voltage measurement at the LIA and recorded and displayed in a 2D array of predetermined size. Two matrices are acquired in a single measurement; one image for the amplitude data (radius images) and another for the phase lag data (phase images). Data are then processed using a nearest neighbour filter which smooths the matrix by averaging a ring of pixels around each element and replacing the element with the averaged value. The radius of the filter (depth of ring surrounding element) may be varied but in this instance a radius of 2 was chosen as it resulted in the best image quality. The image is colour coded using a scale which runs between the maximum and minimum vales for the data set.

4.1 Initial Images of Simple Shapes

The first MIT images were of the aluminium disk used in the characterisation process and of an aluminium triangle of dimensions

- Sides = 26.42 x 29.84 x 49.86 mm
- Thickness = 0.86 mm

The OAMMIT device was driven at 1 kHz, with an integration time at the LIA of 500 ms and a sensitivity of 5 mV. The integration time is chosen such that the opportunity cost between the Signal-to-Noise Ratio (SNR) and the time taken to acquire the image is satisfactory.

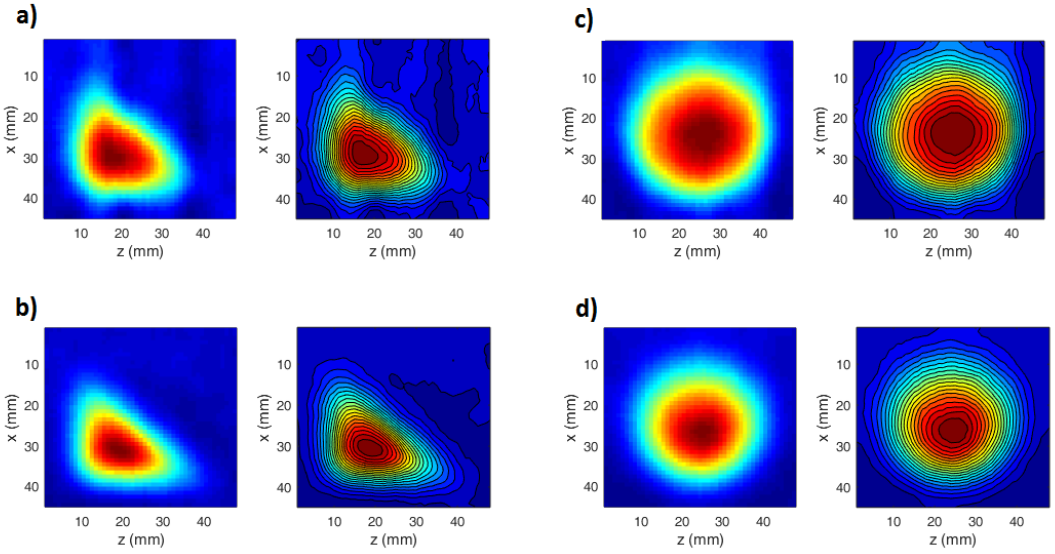

Figure III.14: Preliminary MIT images using MATLAB to generate conductivity map from raw data in a 60 x 60 array. The data are smoothed with a nearest neighbour filter and colour coded. Colour coding is not absolute but varies for each image along a sliding scale which is dependent on the maximum and minimum values present in the array of data which constitutes the image. The image a) is a radius image of the aluminium triangle and b) is the corresponding phase data obtained simultaneously. c) and d) are the radius and phase images of the aluminium disk respectively. Both images were taken when the system was driven at 1 kHz.

Both phase and radius images for the triangle compare well to actual length; but the radius image is more rounded at the sharp corners so the phase data is a better representative of shape. In the images of the disk, the radius image appears larger and 'blurrier' than the phase image, with some dragging artifacts that are more prominent

than in the phase images. The fact that the phase data more accurately represents size is consistent with the expression in equation III.1 where the conductivity contribution is purely imaginary and related directly to the driving frequency. The radial data may be influenced more strongly by spurious external fields.

The dragging artifact where the image appears to be smudged along the x-axis could be attributed to the fact that the image was acquired by taking successive measurements in this direction and in alternate directions for each column. If the translation stage was moved before the data was fully acquired, averaged, and entered into the correct element in the array, it is possible that the data were entered into pixels that represent the object further down the acquisition path.

To compare image quality, the Contrast (C) [111]

$$\mathrm{C} = \frac{\max - \mathrm{BG}}{\mathrm{BG}} \tag{III.14}$$

where the 'max' is the maximum value in the image and 'BG' is the background (i.e the values contained in array elements where there is no object present), may be computed. This gives an indication of the absolute differences in conductivity between parts of the image. Another indicator for quantitative comparison purposes is the Signal-to-Noise Ratio, which we define as

$$\mathrm{SNR} = \frac{\mathrm{Average}_{\mathrm{centre}} - \mathrm{Average}_{\mathrm{edge}}}{\max - \min} \tag{III.15}$$

where the difference between the average values at the centre of the object and at the edge of the object is divided by the difference between the maximum and minimum at the centre of the object for a three pixel radius. In real terms, this value can provide information about image sharpness and how visible the object of interest is compared to the average noise power.

Image Type	Shape	C	SNR
radius	Δ	0.0058	2.31
phase	Δ	0.67	4.35
radius	◯	0.0092	4.56
phase	◯	1.12	6.01

Table III.1: Summary of SNR and C for images of aluminium triangle and circle

The phase image for the triangle exhibits 115 times more contrast than the radius image and this is increased to 121 times more contrast for the disk. This suggests that conductive objects are more easily detected using the phase data, with the possibility of

detection of smaller objects. There is an improvement of 1.3 of the SNR in phase data compared with radius data for the disk, and the SNR of the phase image of the disk is twice that of the triangle. Although the disk had improved contrast, its SNR improvement was smaller than that of the triangle. The average signal is much higher for phase images, but they also exhibit increased noise with respect to radius images; the implication of this is that this noise is generated by the object itself rather than the OAMMIT device.

4.2 Imaging of a Cracked Ring

The assessment of the condition of machinery, parts and vehicles is essential to ensure the safety of users, and non-destructive evaluation methods can achieve this whilst rendering the item intact and usable post imaging. The ability to resolve millimetre-scale features in the material is important to image tiny cracks, small patches of corrosion or rust and thinning of object walls in order to gauge the extent of fatigue or wear; and in turn determine if the object is fit for purpose.

Non-destructive evaluation methods employ a wide range of techniques such as X-ray imaging, eddy current testing and ultrasonic frequencies, but these techniques have a menagerie of limitations associated with them. X-ray imaging, of course, requires radiation protection, can be costly, and requires specific geometries of the object relative to the sensor to be able to image successfully. Eddy current testing only works if the object is conductive and ultrasound methods require physical contact between the sensor and target.

The following cracked ring was used to demonstrate how the OAMMIT might be a useful candidate for non-destructive testing and imaging objects with small fractures present. The ring had dimensions:

- Inner Radius = 44.24 mm
- Outer Radius = 50.8 mm
- Thickness = 2 mm
- Width of Cut = 0.72 mm

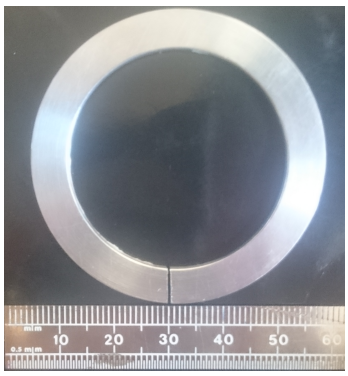

Figure III.15: Photograph of aluminium ring with a 0.72 mm cut. The cut completely severs the ring so that it is discontinuous.

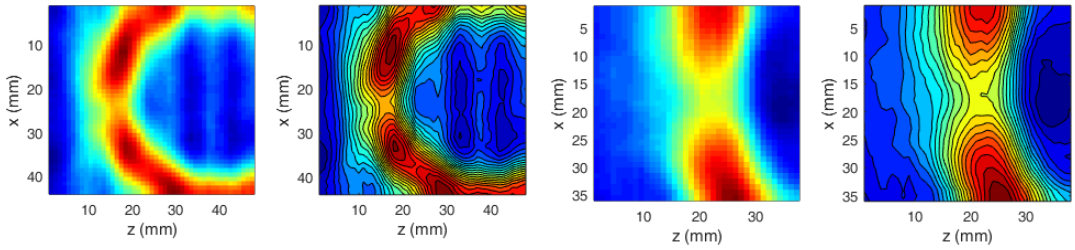

Figure III.16: Radius images and contour maps of a non-continuous aluminium ring. The images on the right are zoomed in and focused on the crack. Images obtained with a 10 kHz driving frequency with an amplitude of 20 V peak-to-peak, corresponding to $\mathbf{B}_{\mathrm{rf}} = 1.9 \times 10^{-8}$ T. LIA was set to a 2 mV sensitivity with a 500 ms time constant [111].

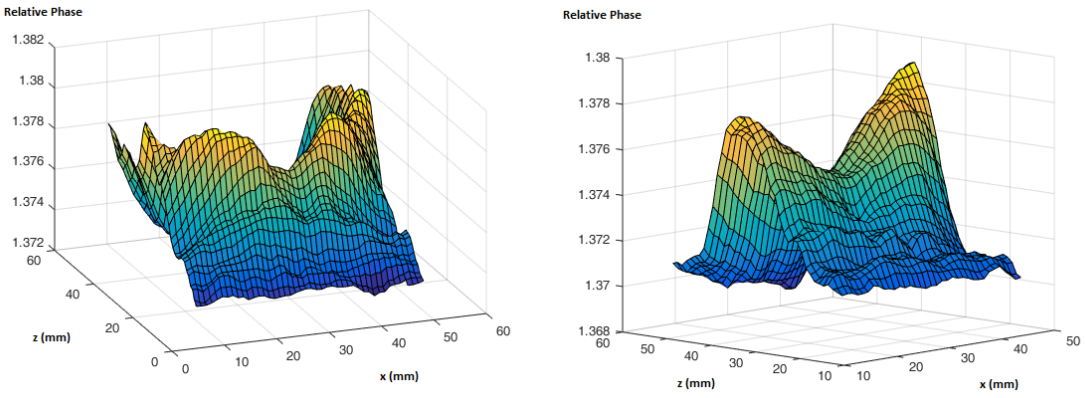

Figure III.17: Smoothed 3D surface maps of the radius data for the full ring (left) and the zoomed image (right).

Data for the cracked ring are shown in figures III.16 and III.17 as 2D images of the phase and radius measurements, 3D surface maps of the radial data. Both 2D images

of the ring are contained in a 60 x 60 array with a driving frequency of 10 kHz whose amplitude was 20 V peak-to-peak, resulting in a 1.9×10^{-8} T magnetic field generated by the induction coil. The size of the ring is well represented and the shape is symmetrical about the crack in the unzoomed image. The crack is also seen in figure III.16 in the same position as in figure III.15, around 20 mm from the furthest end of the inside edge of the ring along the x-axis. The blurring seen with the disk and triangle above is also present here. Nevertheless, this does not spoil the overall effect of the image.

The zoomed image shows the fracture very well, with the boundaries defining the the areas with the most intense signal (in red) completely separated in the contour plot. This is especially evident in the 3D surface plot.

'Ripples' along the z-axis are seen in the unzoomed image which was also observed in a similar position to the radius image of the triangle, but is not so prominent in the disk image. The ripples may be due to a signal coming from the rails that hold the test object platform, which overhangs the sensing region as it moves the object and is in the same orientation as the ripples.

4.3 Imaging Shielded Conductive Objects

Travellers may pass through an airport several times a year, and if they were subject to scanners that employed ionising radiation, this could have an adverse affect on health. Currently, full body passive millimetre wave (PMMW) scanners are used in some UK airports to detect weapons, drugs, and other items that pose a security threat which may have been concealed under clothing. Images taken indoors with a commercial PMMW of a traveller show that the contrast between a gun tucked into a belt and the skin of the person are sufficient for identification of the concealed weapon [112], but since a pair of cotton jeans absorbs just over half of the millimetre wave radiation then additional clothing or layers could fool the scanner. These scanners have a very poor spatial resolution since they only make use of the ambient thermal signature. As such, they are mainly used to determine if a body search or pat-down is required and if so, is time consuming.

These passive millimetre wave scanners are also used at Channel Tunnel ports between Calais and Dover to replace outlawed x-ray scanners. These high-dose ionising-radiation scanners were used to detect illegal items as well as stowaways and people trying to enter the UK illegally. As these people cannot, or will not provide written permission to be irradiated the scanners have since been banned. Non-ionising radiation capable of penetrating very thick (perhaps up to 20 cm) metallic screens with the possibility for real time scanning is needed.

Here the OAMMIT's suitability is explored for such a scanner. A copper square with

sides $l = 25.24$ mm and thickness of 1 mm was shielded by a larger aluminium square with sides $l = 37$ mm and thickness also of 1 mm. Since copper has a higher conductivity than aluminium, in theory, shielded copper square should be easily visible to the magnetometer should the right frequency at the driving coil be selected.

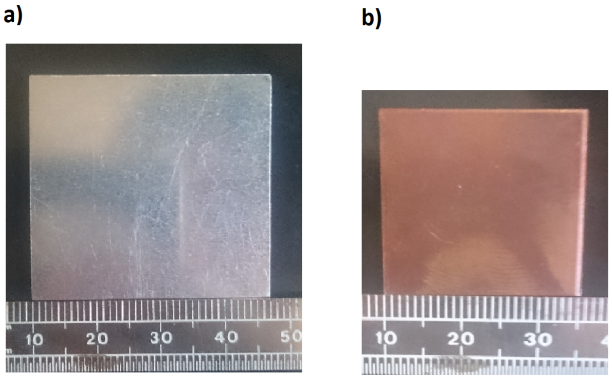

Figure III.18: Aluminium and Copper squares used in investigation, with scale.

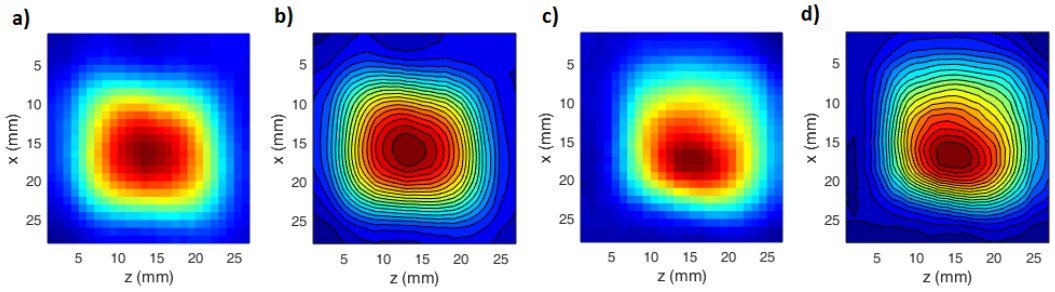

Figure III.19: From left to right; a) is a radius image of the copper square with contrast C=0.0268 and SNR= 3.375, and b) the corresponding contour map, with c) and d) being phase images. The contrast in the phase image = 0.6 and SNR = 1.682. Images were taken with a 1 kHz driving field which has a skin depth of 2.061 mm in Copper.

The unshielded copper square images in III.19 reproduce the square shape fairly effectively even if the corners are not so sharp. The radius image has C=0.0268 and SNR= 3.375, and for the phase images these quantities are C=0.6 and SNR=1.682. The lower SNR for the phase image is surprising since this is not consistent with the previous phase images for the aluminium disk and triangle.

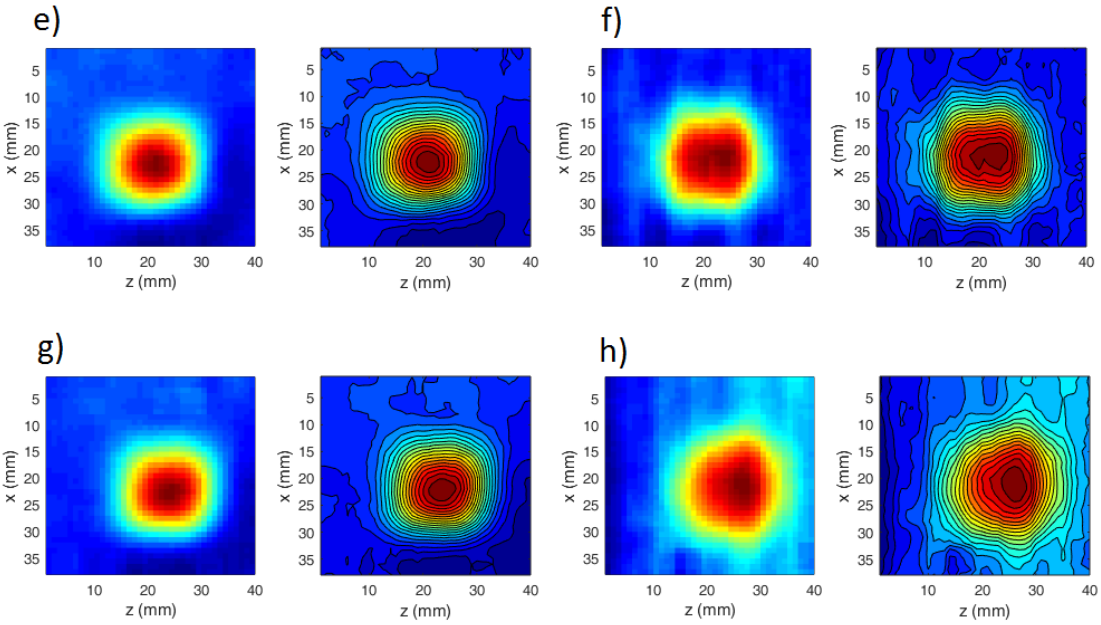

Figure III.20: MIT images of copper square shielded from induction coil with a larger aluminium square. e) and f) are phase and radius images respectively of the shielded square with a paper barrier between the metals. g) and h) are phase and radius images of the copper square when there is no barrier.

The copper square was then shielded from the induction coil using an aluminium square, with a piece of paper between them to prevent eddy currents being induced and passed between the copper and aluminium. The images were taken with a driving frequency of 500 Hz which corresponds to a skin depth of $\delta_{\mathrm{Al}} = 3.7$ mm and $\delta_{\mathrm{cu}} = 2.9$ mm, which penetrates both materials completely. These images are shown in e) and f) in figure III.20 for the phase and radius data respectively. It is immediately obvious that the phase data is a much better representative of shape, with the radial data exhibiting artifacts similar to those seen earlier in the radial data of the cracked ring, which may be due to the overhanging rails. The length of the shielded images of the copper square in both the phase and radius images compares well with the unshielded images of copper. The change in driving frequency between the unshielded images (1 kHz) and the shielded ones (500 Hz) does not appear to have affected image quality.

In figure III.20, g) and h) are phase and radius images when there is no barrier between the two squares. The data plot and contour map of the phase is almost exactly reproduced compared with e); this is expected again because of the explicit dependence of phase lag on conductivity. The radius image h) is of poorer quality, even compared to the image in f). The image is particularly asymmetrical along the z-axis with signal leakage to the right of the image and a large degree of overall distortion. The leakage and

distortion may be attributed the presence of the aluminium square, which could affect the DC field homogeneity acting on the rubidium atoms. Upon closer inspection, there is some signal 'shading' or 'leakage' at the bottom right of e) and g), and the bottom of f) which may be also caused by the presence of the aluminium, since it has a larger area than the copper square. Considering also equation III.1, the radius has a stronger dependence on the atomic precessional frequency than the phase component, so any field inhomogeneieties would be amplified in the radius data.

Comparing f) and h), the absence of the paper barrier worsens distortion and signal leakage, which suggests that eddy currents are able to circulate and pass between the aluminium and copper, which may be degrading the image quality in this instance.

4.4 Doubly Concealed Copper Square

To truly shield the copper square from the magnetometer, it was screened from the induction coil and the sensor OAM unit by 'sandwiching' it between aluminium squares. The aluminium square used in the previous investigation was placed underneath the copper square and a new aluminium square of thickness 2 mm was placed on top of it. This particular arrangement serves to potentially simulate the detection of conductive objects inside conductive enclosures. Images were acquired when the induction coil frequency was varied between 200-350 Hz.

Frequency (Hz)	δ_{al}(mm)	δ_{cu}(mm)	Total Penetration Depth (mm)
200	5.79	4.61	16
250	5.19	4.12	14.5
300	4.73	3.76	13.22
350	4.38	3.48	12.24

Table III.2: Table to summarise the penetration depth through aluminium and copper when the frequency used to induce eddy currents in them was varied.

Even at the highest frequency explored (350 Hz), penetration depth is much larger than the total thickness of the materials (4 mm) so in theory the copper square should be visible to the magnetometer since it is able to interrogate the full width of the metallic structure. As the images below show, even if the square shape is not perfectly recovered, detection of an object with a different conductivity is possible.

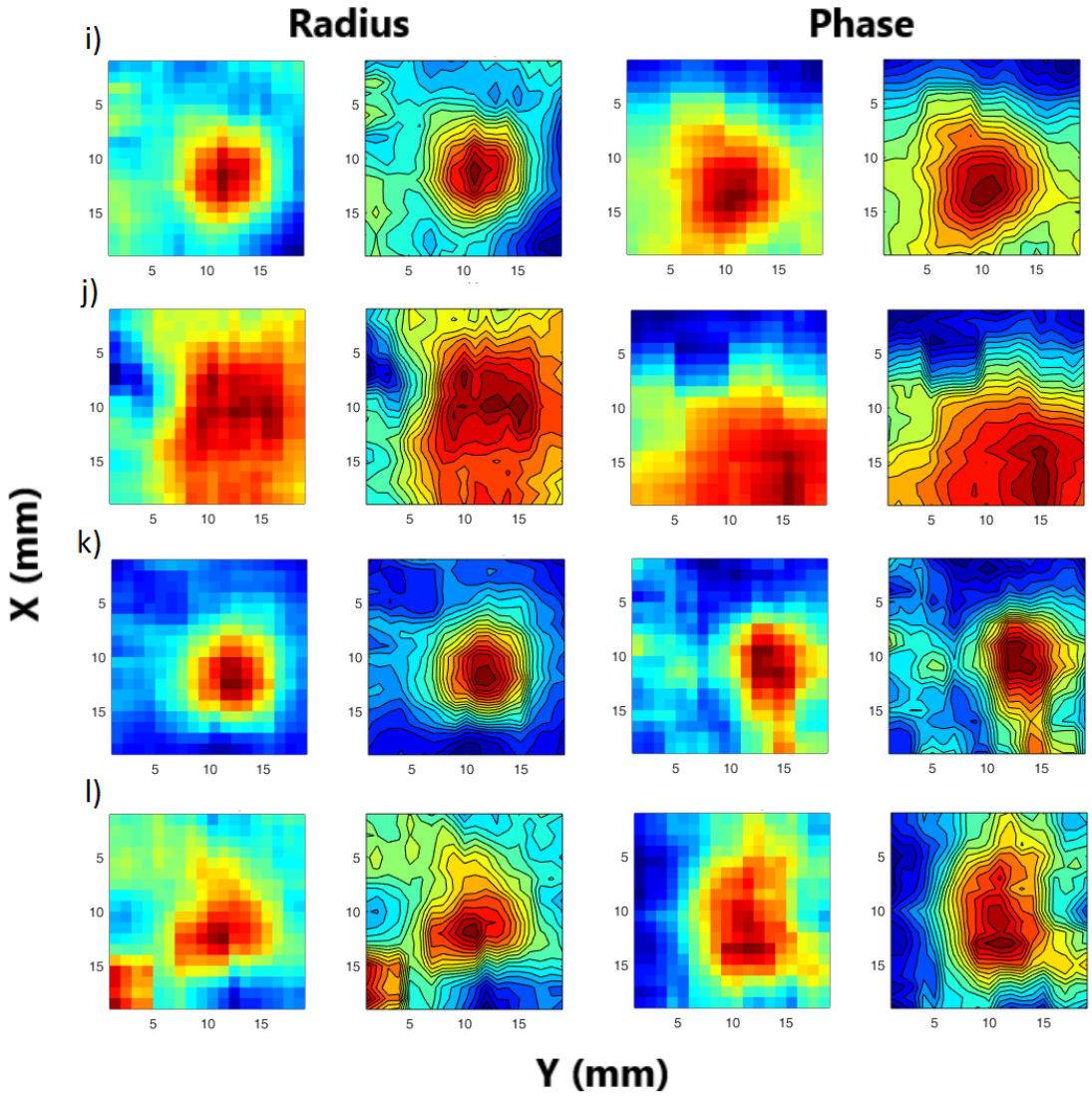

Figure III.21: Phase and radius images of a copper square sat between a 2 mm and a 1 mm aluminium set of screens when different frequencies are supplied to the induction coil. Key: i) 200 Hz, j) 250 Hz, k) 300 Hz and l) 350 Hz.

It appears that changing the frequency changes the 'snapshot' acquired of the image. At 200 and 300 Hz (images i) and k)) the copper square signal is more localised to the known physical relative position of the square and less as if there is signal 'leakage'. Driving frequencies at multiples of 50 have significantly worse image distortion; if this is a significant effect due to the driving frequency selection this should be explored more. The blurriness in j), however, could be attributed to external vibrations and RF noise from nearby experiments, where a Bose Einstein Condensate experiment was in operation, especially since the phase image has incorrectly positioned the copper at the bottom of the field of view.

It seems that the optimum image was acquired at 300 Hz which is a total penetration

depth of 13.22 mm. Since all the frequencies explored have a much higher penetration depth than the thickness of the combined widths of the two aluminium shields and the copper, but exhibit drastically different images, then this suggests that the frequency could affect the image resolution also.

The severity of the distortion in the images may be a consequence of the DC field contribution from the aluminium shield, effectively changing the resonant frequency of the system, the optimum working point of the magnetometer and ultimately the sensitivity. This could also account for the reduction in apparent size of the copper square to around 7 mm.

In the bottom right corner of the radius images in l), there appears to be a small object or corner of an object. In reality, this area is where the aluminium samples are located, since the field of view in the images is 20×20 mm and the aluminium squares have sides l=35 mm. The 'object' has a square shape and straight lines, and is not present in the phase map, which suggests that this is not an anomaly in the detection of the field, but a mathematical error in the image processing stage.

5 Conclusions

The OAMMIT has successfully demonstrated the possibility of a real time, remote scanning device for imaging and detection of conductive objects. Images generally compare well in size and shape, with phase images being a better representation of size due to the direct link between the phase data and conductivity of the object. The first takeaway message from looking at the initial images is that the translation stage must be moved slower than the time taken to average the data and enter this number into the correct element of the matrix, or there will be artifacts in the picture. These can be see in figure III.14 as pixels dragged vertically along the image.

Most high resolution images were taken in around 40 mins but acquisition time can be significantly reduced by using an automatic translation stage and using an array of sensors, i.e. 40 x 40 array. Spatial resolution of <1 mm is achievable with the OAMMIT with the ability to identify cracks of this size in materials. Whether the device is able to distinguish between foreign materials in an object or if it sees this as a hole or crack should be investigated to assess its suitability for non-destructive testing.

The system imaged the copper square at successive penetration depths, providing different images at different induction frequencies, indicating potential for operation in a tomographic mode. Further exploration is required, however, into the possibility of this and to characterise the effect of penetration depth and frequency on image quality,

expected content, and resolution. Another line of enquiry in this vein is to consider whether using lower frequencies, to increase penetration depth through a material images a single slice, or if the OAMMIT system is imaging a slice of the object plus the cumulative signal of the object before the skin depth is reached. In addition, the conclusion that can be made from the copper square investigation is that the OAMMIT has the potential to penetrate conductive shields.

Chapter IV

Detecting Rotating Machinery

A promising application of the OAM is the remote detection of industrial machinery, which has advantages in continuous monitoring of turbines and generators for safety, defence and security applications. A feasible device for this kind of monitoring would have to be portable for true remote detection, requiring small modifications to the setup used for MIT described in the previous chapter .

1 Towards a Portable Device

This section describes the construction of an OAM built using an Extended Cavity Diode Laser (ECDL), almost identical to the one described in the previous chapter, with the beam taking the same path through optical components (squeezed onto an area of 65 x 40 cm) onto a breadboard sitting on a wheeled trolley for ease of transportation. For magnetic signature detection, the output of the photodiode is re-routed to an Anritsu MS2718B Spectrum Analyser (SA) instead of an LIA (see figure IV.1). The OAM sensor unit was redesigned so that the Helmholtz coil pair, RF coils, and cell are more stable and robust.

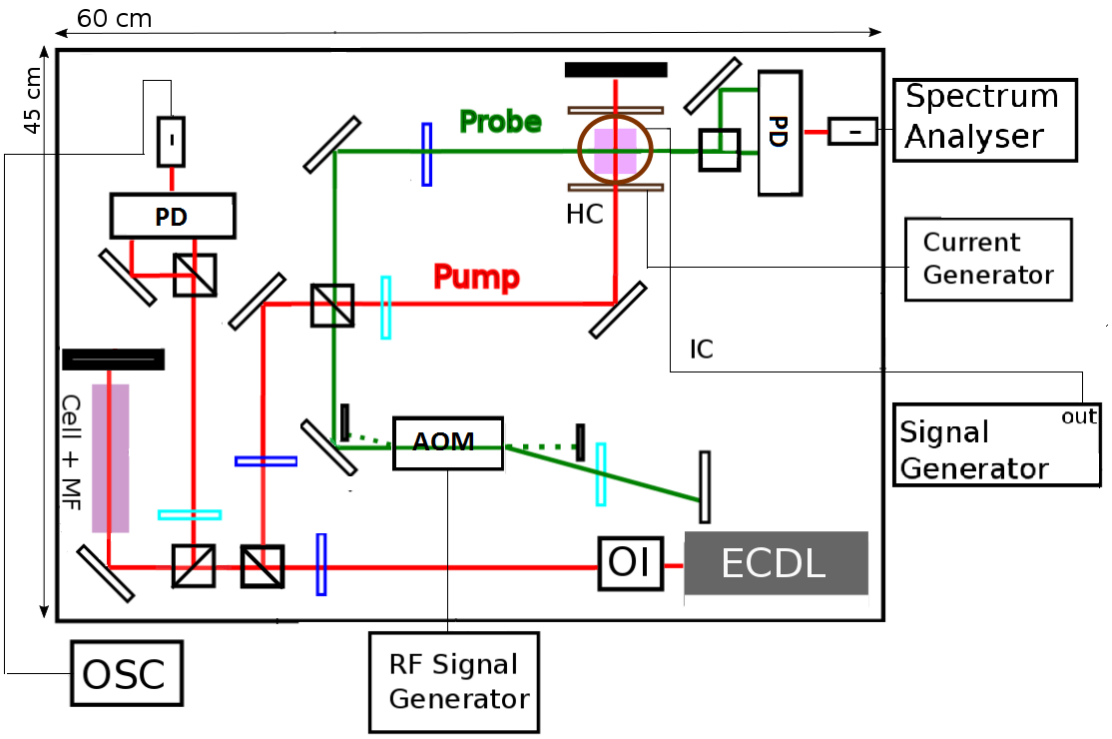

Figure IV.1: Optical and electronic OAM scheme for the detection of rotating machinery. Arrangement of optical components on table, the electronics, and the connections between them. Key: OI is an Optical Isolator, MF is a magnetic field, PD is a balanced Photodiode, OSC is an oscilloscope, AOM is an Acousto-Optical Modulator, IC the Induction Coil and HC a coil pair to provide a DC field. The turquoise and dark blue structures in the beam path refer to $\frac{\lambda}{4}$ and $\frac{\lambda}{2}$ waveplates respectively. The sensing cell filled with a natural mixture of ^{87}Rb and ^{85}Rb is in the location of the intersection of the pump and probe beams, sandwiched between the Helmholtz coils. All optical components are bound by an area measuring 45 x 60 cm.

1.1 Interference Filter-Stabilised ECDL Laser

Usually, ECDLs employ a movable diffraction grating for wavelength selection. A disadvantageous consequence of this is that the output beam direction varies according to the grating angle, which can be time consuming to realign [113]. This type of ECDL laser can also be relatively unstable since the grating may undergo deformation due to changes in the ambient pressure [114].

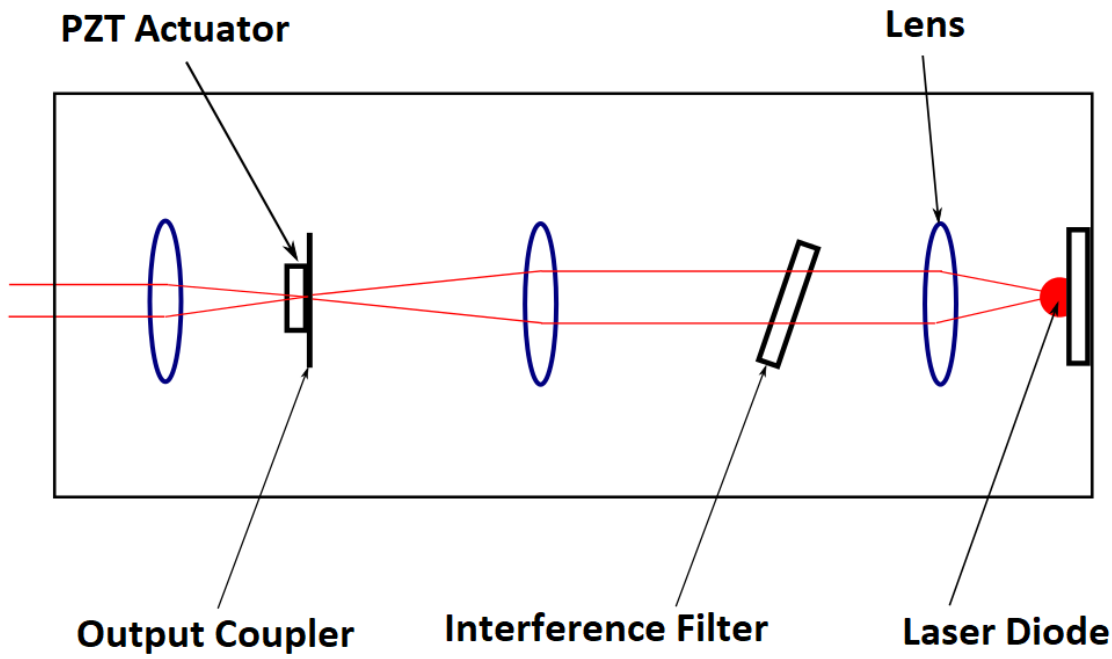

Figure IV.2: Schematic diagram to illustrate arrangement inside cavity of commercial *Radiant Dyes* interference filter- stabilised ECDL Laser. The beam from the laser diode passes through an interference filter whose angle with respect to the incident beam may be varied by adjusting attached screws, in order to select the wavelength. The beam then passes through the output coupler, a partially reflective mirror, whose angle is changed by the PZT actuator. This adjustment effectively varies the cavity length for fine tuning of the spectrum and provides optical feedback to the laser.

In light of this, an interference filter-stabilised ECDL laser is used thanks to its high stability and robustness. Light output is provided by a semiconductor diode chip and directed through a collimation lens towards an interference filter which has multiple dielectric coatings. The transmitted wavelength is given by [114]

$$\lambda = \lambda_{\max} \sqrt{\frac{1 - \sin^2 \theta}{\eta_{\text{eff}}^2}} \,, \tag{IV.1}$$

where λ is the transmitted wavelength, $\lambda_{\max}$ is the maximum transmittable wavelength, θ is the angle of incidence and η_{eff}^2 is the effective refractive index of the combined dielectric coatings on the interference filter.

Focusing the resulting beam onto the output coupler (a partially reflecting mirror that provides optical feedback into the laser diode) by means of a lens guards against excessive optical alignment. The angle of the output coupler may be adjusted by an attached PZT, which has the effect of varying the cavity length for fine tuning. A second lens after the output coupler restores the beam collimation. Since the interference filter

and output coupler are independent, the output beam direction is fixed regardless of wavelength selection.

1.2 Sensor Unit Design

The new OAM sensor was re-modelled to house the cell, induction and DC field coils in an entirely plastic unit, and realised using a 3D printer. From figure IV.3 two sets of Helmholtz coils are visible; the DC coils used in the optical pumping process (brown wire), whose magnetic field is aligned along B_0, and a second set arranged perpendicularly to the first. This second set of coils plays the role of the RF induction coil in the OAMMIT configuration (blue wire).

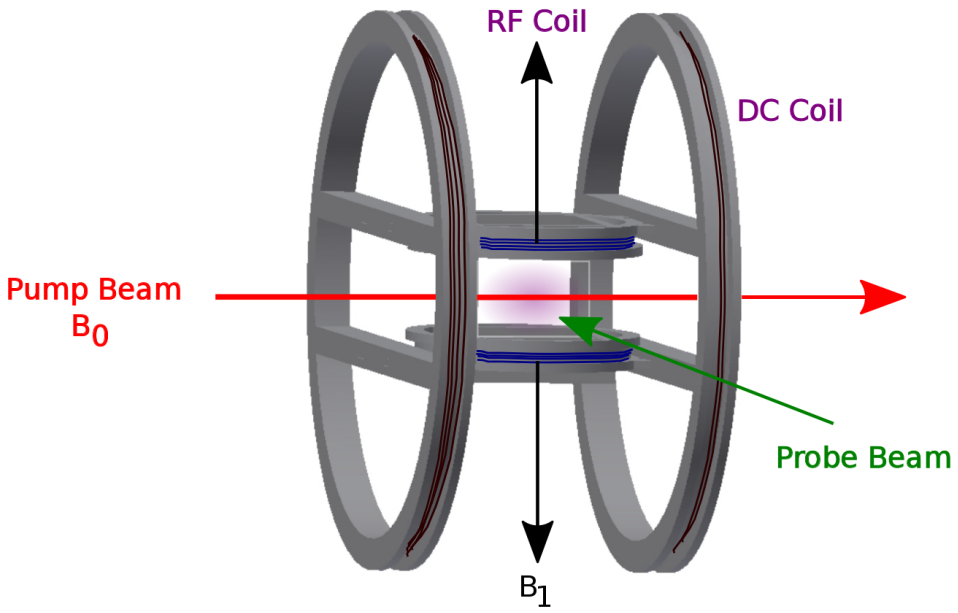

Figure IV.3: Model of updated 3D printed sensor unit for OAM. The new design differs from the previous unit in that the single induction coil is replaced by a Helmholtz coil pair which is attached to the large DC field coils, and is able to securely hold and contain the Rubidium vapour cell.

The DC coil set has dimensions:

- Average Radius= 6.8 cm
- N=30
- Separation= 6.8 cm

The RF induction coils were constructed to encase the Rb vapour cell and as such have dimensions:

- Average Radius= 2.7 cm
- N=30
- Separation= 2.7 cm

2 Electromagnetic Signature Detection

The Rb atomic sample is able to detect the field due to a rotating object/motor (call this field B_2) since such a field introduces a perturbation on the atomic precession. This manifests itself on the frequency spectra obtained by the SA as m sidebands of the central peak, which appears at the driving frequency, f_{RF}. This coupling of B_1 and B_2 permits tuning of f_{RF} away from noisy bands.

The ECDL is locked to the F=3 $\rightarrow$ F=4' transition of ^{85}Rb using the DAVLL, then the probe beam is slightly blue-detuned off-resonance by 195 MHz. As with the OAMMIT, the pump beam together with the DC coils aligns the atomic spins along the DC field direction. The AC field due to the IC drives the spin coherences through the Zeeman sublevels, so that the atoms are precessing at the Larmor frequency. The polarisation of the probe beam is modulated at this frequency, and the signal is fed to a spectrum analyser via a photodiode.

Systematic measurements were made with an Allen key with residual magnetisation, steel samples, a small plastic DC fan, and an AC drill at 40 cm away from the centre of the sensor. Traces were also compared with measurements taken using a fluxgate magnetometer in the same conditions.

2.1 Rotating Objects

To test the concept, small commercial steel samples (EN24T, EN19T, and AISI420) all cut to the same size of (25 x 25 x 1.5) mm with residual magnetisation were mounted on an all-plastic manual motor to demonstrate the effect of rotating magnetic objects and for direct comparison. Their electrical conductivity properties are summarised in table IV.1, but a reliable conductivity value for EN19T was unpublished. The hand operated motor was situated 40 cm away from the centre of the vapour cell. The driving frequency, f_{RF}, here supplied by the IC was set to 100 kHz. The frequency spectra for five different orientations of the rotation plane of the motor, depicted in IV.4, were recorded for each steel sample, and averaged over 20 of such traces under continuous manual rotation of the

motor (at a rate of 1 trace per second). As with the OAMMIT measurements, here the OAM was operated at room temperature and without magnetic compensation.

Sample	Conductivity ($\times 10^6$ S/m)	Applications
EN24T	5.26 [115]	Gears, shafts, studs and bolts in the automotive and aircraft industry.
EN19T	N/A	Automotive gear boxes.
AISI420	1.8 [116]	Knives and surgical equipment.

Table IV.1: Conductivities and applications of EN24T, EN19T and AISI420 steel. Reliable conductivity info for EN19T was not readily available.

For the EN24T sample, the only significant visible difference compared with the background spectrum is the presence of peaks at orientation E. These sidebands are 10 dBm higher than the background, at a detuning of $\pm(17 \pm 0.1)$ Hz from f_{RF}, the large central peak at 0 Hz detuning. Similar is seen for the EN19T sample. With the AISI420 sample, the sidebands are less clear but there are barely visible peaks at $\pm(18 \pm 0.1)$ Hz at orientation C. This is expected since the EN24T grade is much more conductive than the AISI420.

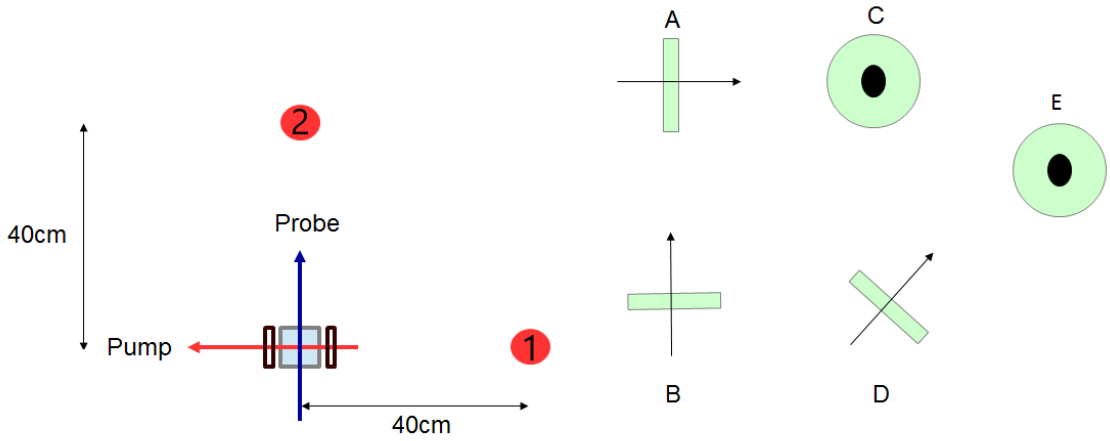

Figure IV.4: Labels to illustrate in which orientation relative to the OAM the steel sample rotations, bicycle wheel and M6 Allen key were detected. The red circles indicate two measurement positions- orientations A to D were taken at measurement position 1. E is technically a rotation of the object in the same orientation as C but performed at measurement position 2; it is assigned a separate label to avoid confusion. C and E rotate the object in the plane parallel to the surface of the optical table, with A, B, and D in the perpendicular plane facing along the direction of the arrow.

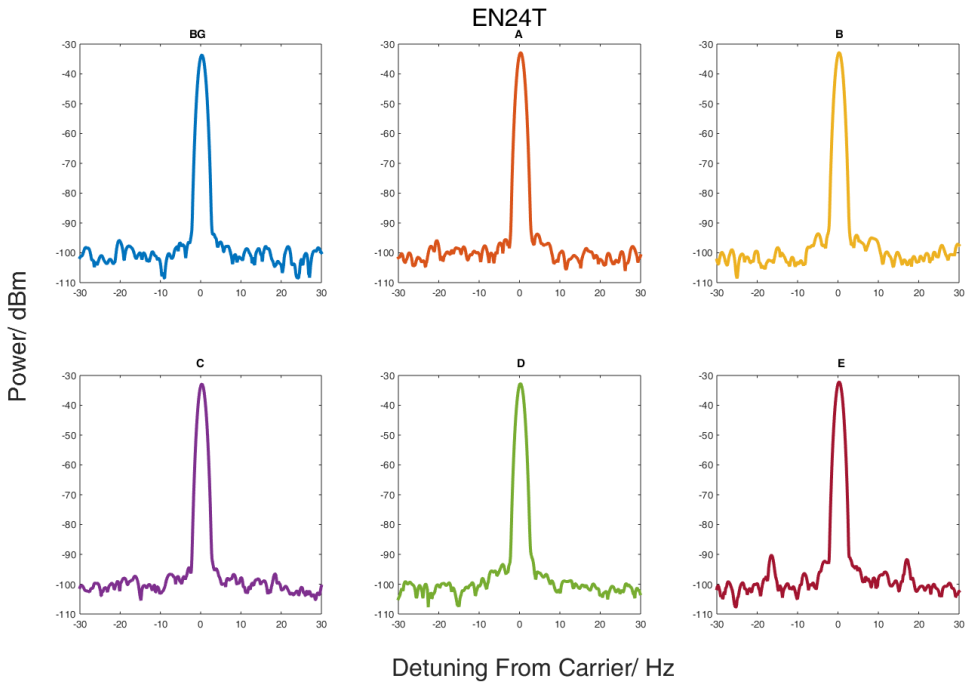

Figure IV.5: 20 Averages of Frequency Spectra of rotating square sample of EN24T steel for five different positions relative to the OAM, and a background trace for comparison. The large central peak is the RF signal at 100 kHz. Clear sidebands of 10 dBm are visible at a detuning from f_{RF} by $\pm(17 \pm 0.1)$ Hz for orientation E only.

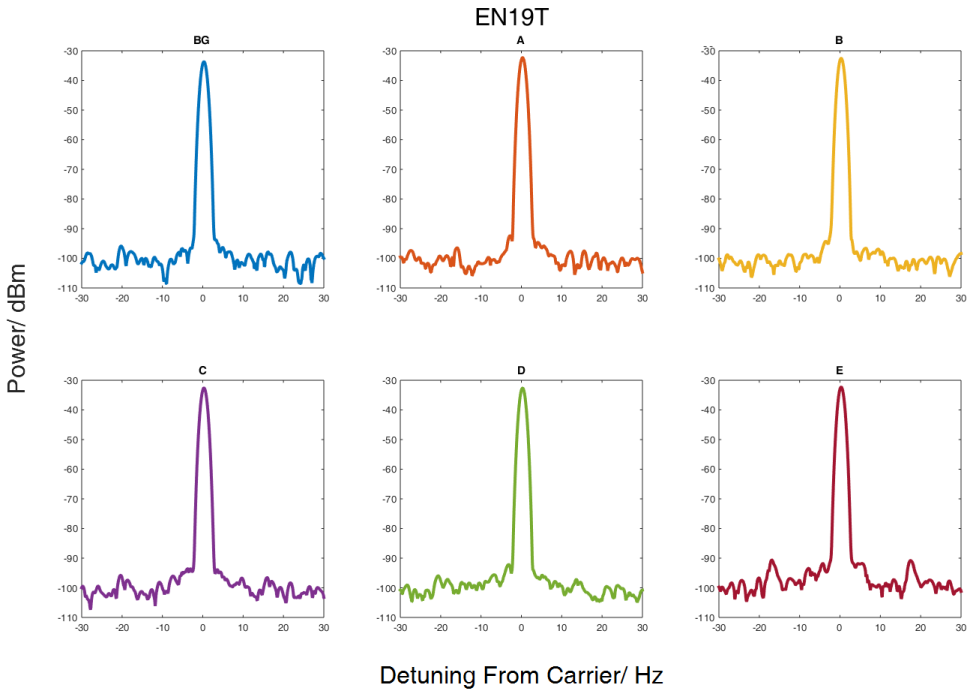

Figure IV.6: 20 Averages of Frequency Spectra of rotating square sample of EN19T steel for five different positions relative to the OAM, and a background trace for comparison. The large central peak is the RF signal at 100 kHz. Here clear peaks are visible at $\pm(18 \pm 0.1)$ Hz detuning from f_{RF} at position E.

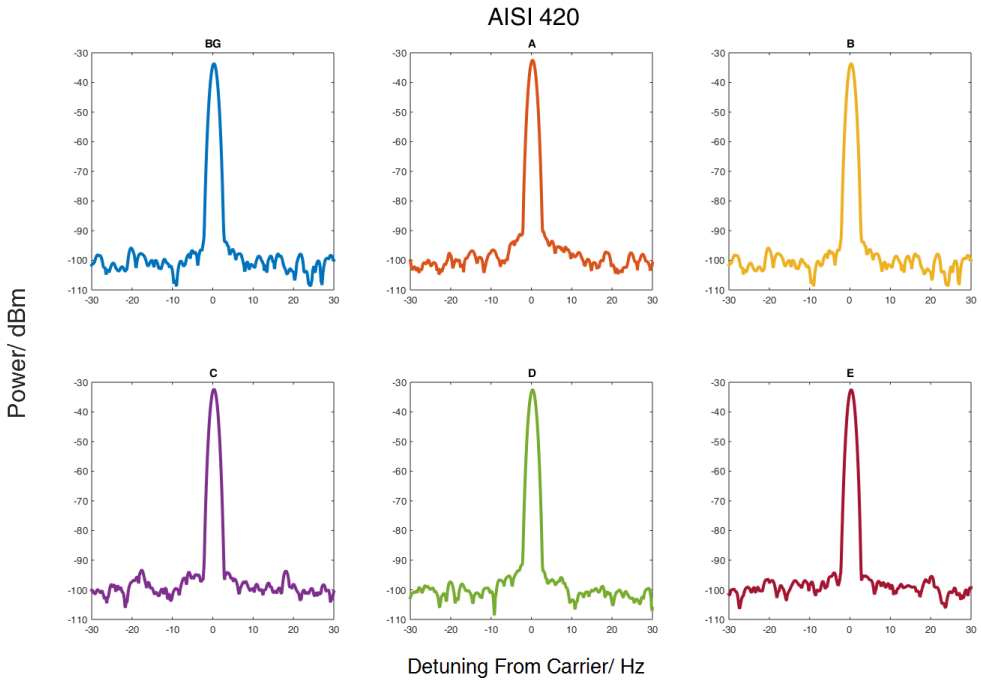

Figure IV.7: 20 Averages of Frequency Spectra of rotating square sample of AISI420 steel for five different positions relative to the OAM, and a background trace for comparison. The large central peak is the RF signal at 100 kHz. For this sample of steel there are noticeable peaks when the sample was placed at orientation C (in contrast to the other samples whose presence was detected at E) and a detuning of $\pm(18 \pm 0.1)$ Hz.

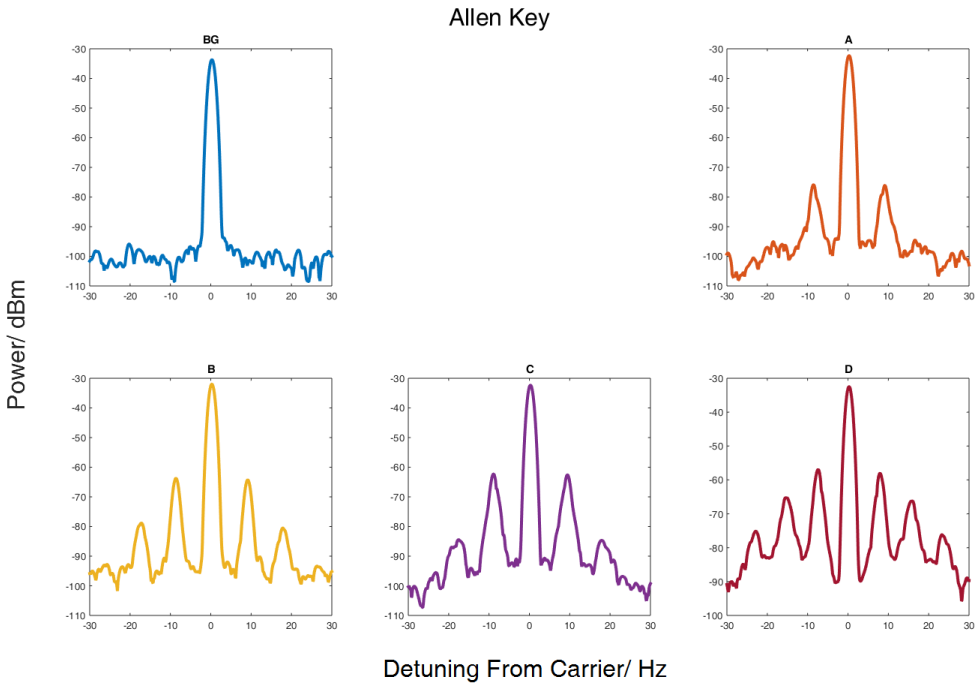

Figure IV.8: 20 Averages of Frequency Spectra of rotating M6 Allen Key for four different positions relative to the OAM, and a background trace for comparison. f_{RF} is seen clearly as the large central carrier peak, with m$\pm(10\pm0.1)$ Hz sidebands due to the rotating Allen key.

An M6 Allen key was mounted to the manual motor and measured in four positions (E is not measured as this position was inaccessible at the time). The clear multiple sidebands are unsurprising since allen keys are magnetised for easier manipulation of screws, with the largest sidebands being 40 dB higher than the background. The sidebands are separated by approximately 10 Hz since the rotation frequency varies due to the hand rotation of the motor.

The spectrum below was obtained by spinning a bicycle wheel in position A at 80 cm away from the vapour cell centre, with the axis of rotation lying along the optical pumping direction. The peaks show the detection of the wheel at $\pm(3.3\pm0.1)$ Hz with the largest sidebands appearing around 35 dB above the background. Additional sidebands are visible at $\pm(6.7\pm0.1)$ Hz and $\pm(10\pm0.1)$ Hz [1].

[1] With assistance in data collection from Cameron Deans due to heaviness of wheel

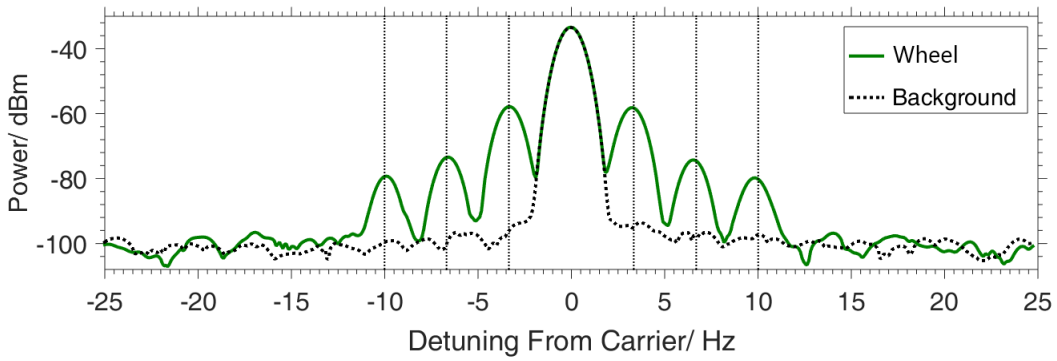

Figure IV.9: 20 Averages of Frequency Spectra of rotating bicycle wheel at orientation A. There are three clearly visible sidebands at 3.3 Hz detuning intervals.

2.2 Heading Errors in Atomic Magnetometers

Heading errors are the variations in absolute magnetic field measured by atomic magnetometers when the relative angle between them changes; it is noticeable in the traces of the rotating allen key and steel samples when looking at the differing peak heights between positions A-E. This is especially problematic on submarine mountable magnetometers where the orientation of the magnetometer is rotated very frequently. For commercial magnetometers, the error is estimated by comparing measurements from a test sensor mounted on a rotational stage with fixed sensors around the perimeter. The difference between these measurements is quoted as a function of angle [117].

2.3 Electric Motors

Electric motors exhibit magnetic signatures, so their visibility on frequency spectra were also tested for both AC and DC motors. To model these types of motor, a 24 V DC plastic fan (Sunon, model number KDE2412PMB1-6AB) and a 120 V AC drill constructed from a variety of materials (Dumore, model number 37-021) were placed at position A in figure IV.4.

The DC fan was placed 1 m away from the sensor, and a 20 measurement averaged background trace was acquired with the fan off. The fan was turned on and spectra were again averaged over 20 traces. The results are depicted in figure IV.10. When the fan is off (dashed trace), sidebands of f_{RF} are visible every 50 Hz since the mains power magnetic field and RF IC field are coupled. Turning the fan on results in the appearance of two peaks at $\pm(170 \pm 1)$ Hz.

The signature frequency of the DC fan is three times larger than the physical rotational frequency (51.6 ± 1) Hz [118], which reinforces the point that the resultant visible

signal is due to coupling between the magnetic field due to the IC field and the AC magnetic field of the motor.

The Dumore AC drill used to model an AC motor was a variable speed drill which could be adjusted between 10^3 and 1.6×10^4 RPM. Averaging over 20 traces, an increase in the power level can be seen at 100 Hz (and harmonics) compared with when the drill is off, in addition to a in increase in power around the base of the central peak. This appears since the drill head produces low frequency noise. The peak position on the frequency spectrum was independent of the rotational speed.

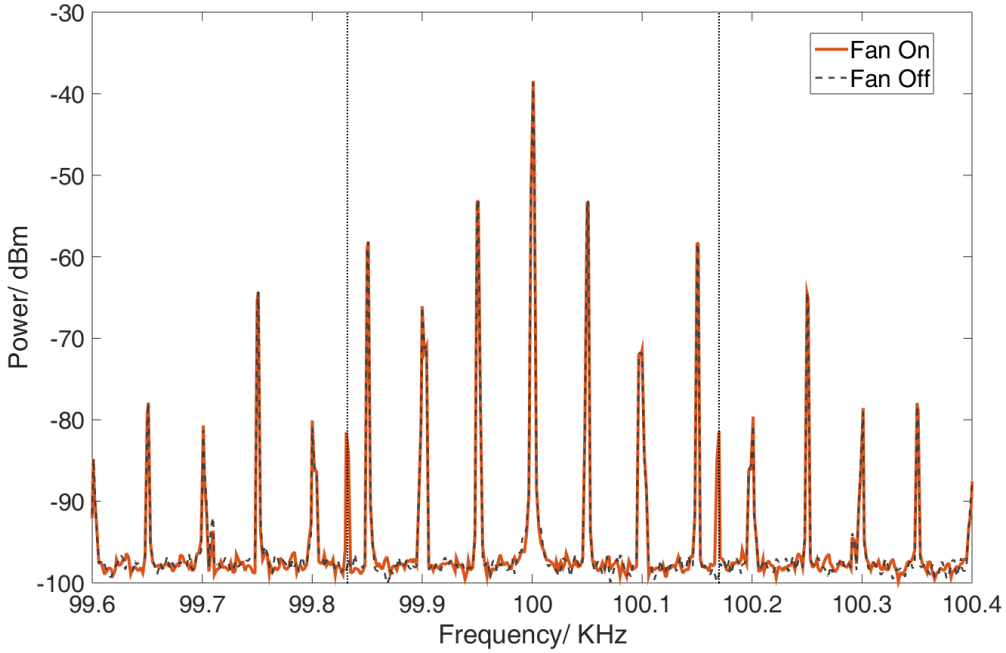

Figure IV.10: Power spectrum averaged over 20 traces to demonstrate detection of rotating motors, obtained using a 24 V DC fan situated 1 m from the sensor centre. The vertical dashed line indicates that the peak of the motor is visible at $\pm(170 \pm 1)$ Hz.

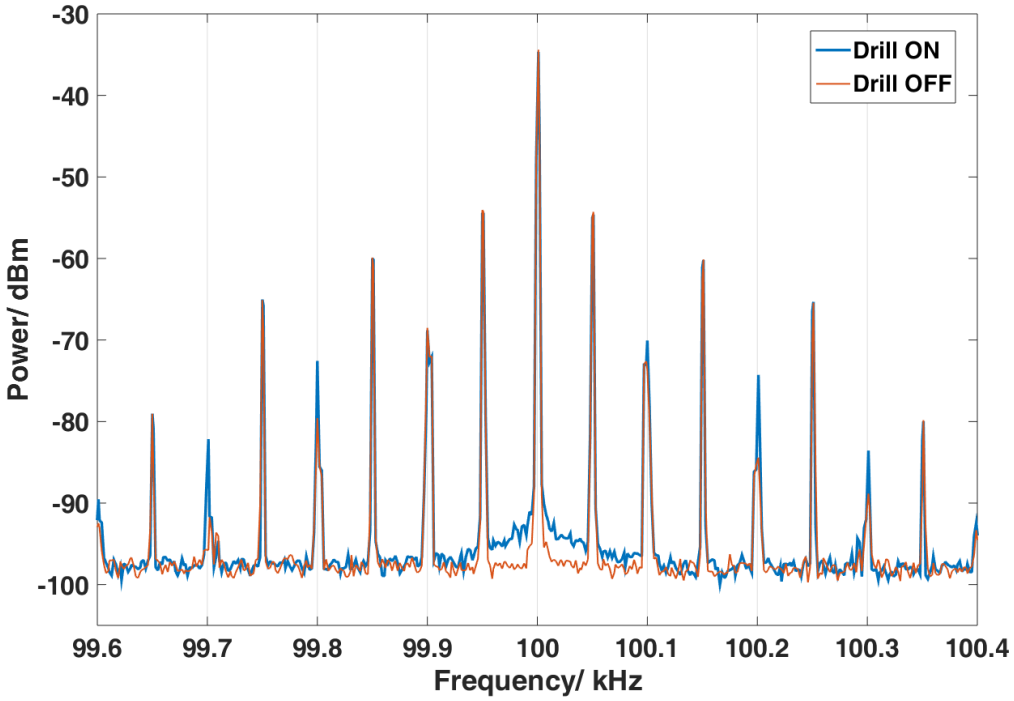

Figure IV.11: Power spectrum averaged over 20 traces to demonstrate detection of rotating motors, obtained using an AC drill situated 60 cm from the sensor centre. The vertical dashed line indicates that the peak of the motor is visible at $\pm(100 \pm 1)$ Hz, with second and third harmonics.

3 Performance Characterisation

In order to further establish the use of the OAM for the detection of rotating machinery, additional performance tests were carried out. The power response at the SA of the motor signal at increasing distances from the sensor was investigated, as well as the real application of detection of motors behind walls. The OAM response was also compared to a commercially available fluxgate magnetometer at extreme low and high-end frequencies.

3.1 Through-Wall detection

The DC fan was turned on and spectra averaged over 20 traces were obtained when the fan was placed at increasingly larger distances from the centre of the vapour cell[2]. The height of the first sideband (at 170 Hz) with respect to the background for each average was recorded and graphed (see fig IV.12) as a function of distance from the cell. The sideband power levels decrease exponentially with an increasing distance, and are visible (noticeable signal above the background) upto 2 m away.

[2]With Lorenzo Gori.

In an investigation to ascertain the feasibility for cross-barrier detection, the DC fan magnetic signature was detected from the other side of a 17 cm thick wall containing concrete, pipes, and mainlines, 70 cm away from the vapour cell. The height of the first sideband of the main RF peak was plotted in dBm as a function of distance from the cell. From figure IV.12, the measurements made beyond the wall are not significantly diminished compared with magnetic fingerprint measurements made with no dividing wall (they both fall within each others error tolerance). The error bars included come from the standard deviation of 20 averages. The sideband power decreases exponentially upto around 80 cm away from the cell. The OAM does not appear to be affected by the wall and potential noise sources (from metal pipes, electrical wiring or even parts of the air conditioning system) contained within it.

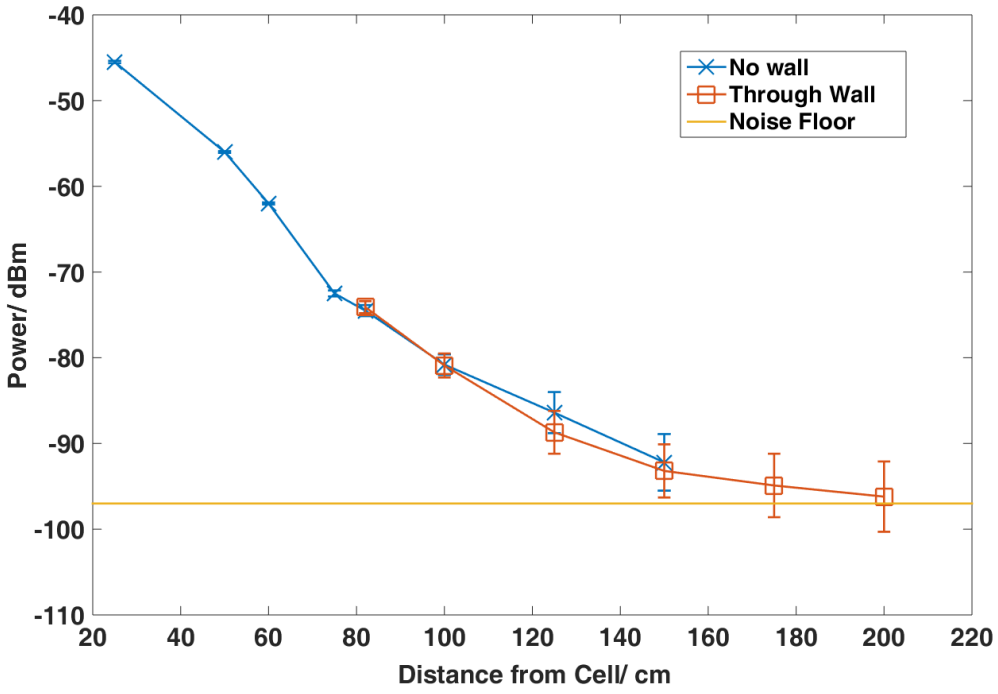

Figure IV.12: Power level of the first sideband for the DC fan spectrum plotted between 20 and 200 cm away from the sensor, with a second set of data for the same distances but separated by a 17 cm thick wall from the vapour cell.

To characterise the optimum voltage supplied to the IC, it was varied between 0 and 20 V (max output) and the sideband power level recorded after 20 averages were made. The results are below in figure IV.13 with examples of the spectra when the driving voltages were 0 and 5 V in figure IV.14. There is no peak nor sidebands when the driving voltage is set to 0 (the voltage supply was on); the sideband power height above the power level at 0 begins to emerge as soon as the voltage is increased. In fact, it increases until the sideband height saturates at a driving voltage of 17 V.

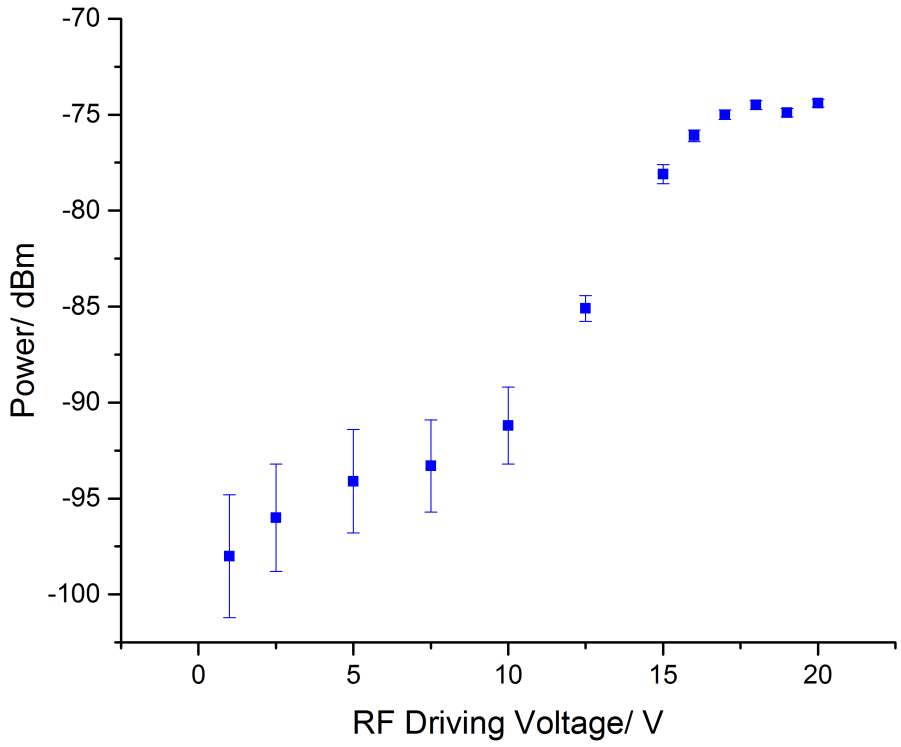

Figure IV.13: The power amplitude of the DC fan (70 cm away from the sensor) for different voltages supplied to the RF coils at 10^5 Hz. The error bars indicate the standard deviation from the 20 averages used before recording the final power for each measurement.

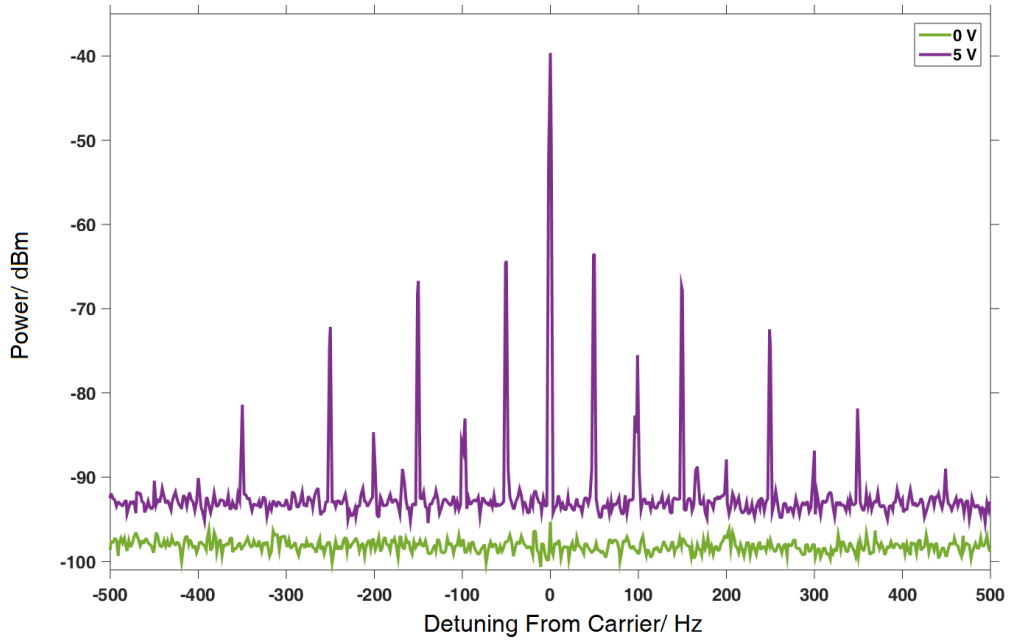

Figure IV.14: For reference, full spectra of the DC fan turned on at 70 cm away from the sensor, when the driving voltage was 0 and 5 volts and f_{RF} was 10^5 Hz. The 5 V spectrum has been upshifted in power on the graph for clarity, with both spectra sharing the same noise floor.

3.2 Direct Comparison With Fluxgate Magnetometer

In place of the atomic sensor, a fluxgate magnetometer (FG) was employed to compare and confirm that the frequency sidebands seen previously under detection of the DC fan were in fact a magnetic signature. The FG replaced the vapour cell in its exact position on the optical bench and was connected to the SA. The DC fan was switched on 50 cm away from the FG and after 20 averages figure IV.16 was generated. The same $\pm(170 \pm 1)$ Hz peak and mainline bands which appeared on spectra obtained using the OAM are apparent on the trace, and easily detectable by the FG. By contrast, however, there is significant $1/f$ noise, particularly below 10 Hz where it drastically increases.

For measurement of high frequency rotating machinery low frequency noise is not a relevant issue. However, for machinery that rotates at a low RPM, these will be difficult or impossible to detect using a commercial FG. See figure IV.15 where there is no signal larger than the background noise for the AISI420 steel sample being rotated at (18.0 ± 0.1) Hz and 40 cm away from the FG. The mains power peak however, is easily picked up.

For direct comparison at a lower arbitrary driving frequency of 3×10^4, the DC fan was detected by both methods and the result is displayed in figure IV.17. Again 20 averages were made with the FG being placed in the same position as the Rb cell.

Detection of the fan as sidebands of the driving frequency are seen on the OAM trace at the now expected $\pm(170 \pm 1)$ Hz peaks, which is in agreement with detection at the 100 kHz driving frequency. However, detection of the fan in this manner is not effective with the FG as sidebands are not detected at the fluxgate- unless the magnetic frequency signature is known, detection of the fan requires scanning for the frequency peak.

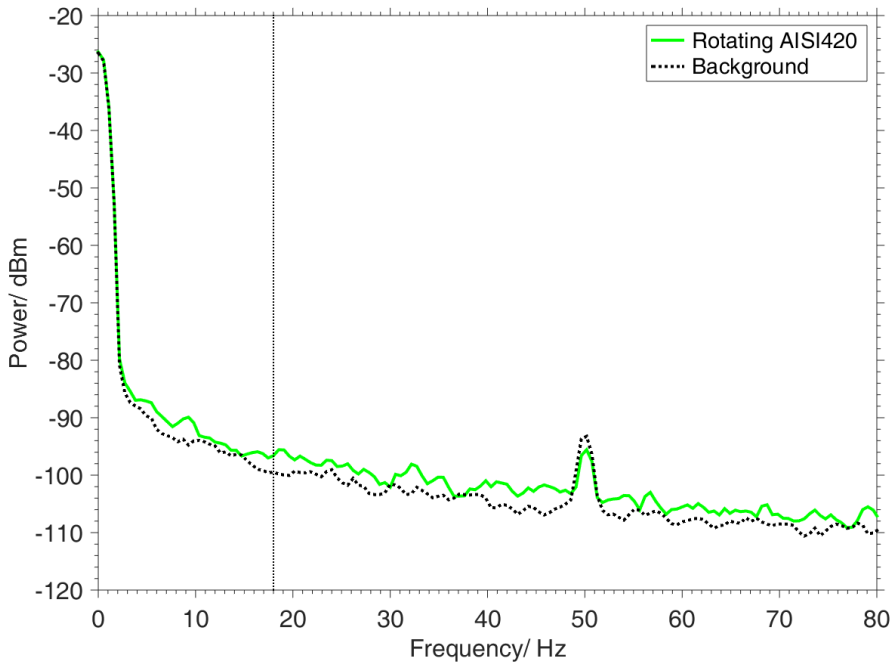

Figure IV.15: Trace of AISI420 steel sample rotating at (18.0 ± 0.1) Hz and placed 0.40 m away from a FG magnetometer, in this case the sensor, at orientation C in figure IV.4. The FG was unable to detect the presence of the rotating steel.

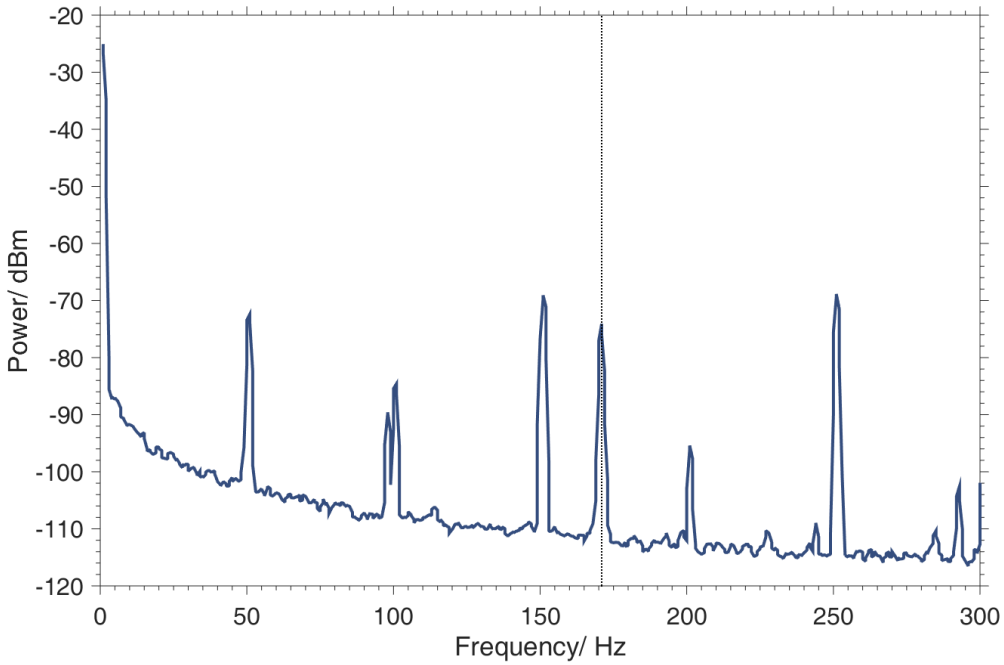

Figure IV.16: DC fan signature detected using a FG magnetometer as the sensor and labelled by the dotted line at (170 ± 1) Hz. It was 50 cm away from the FG.

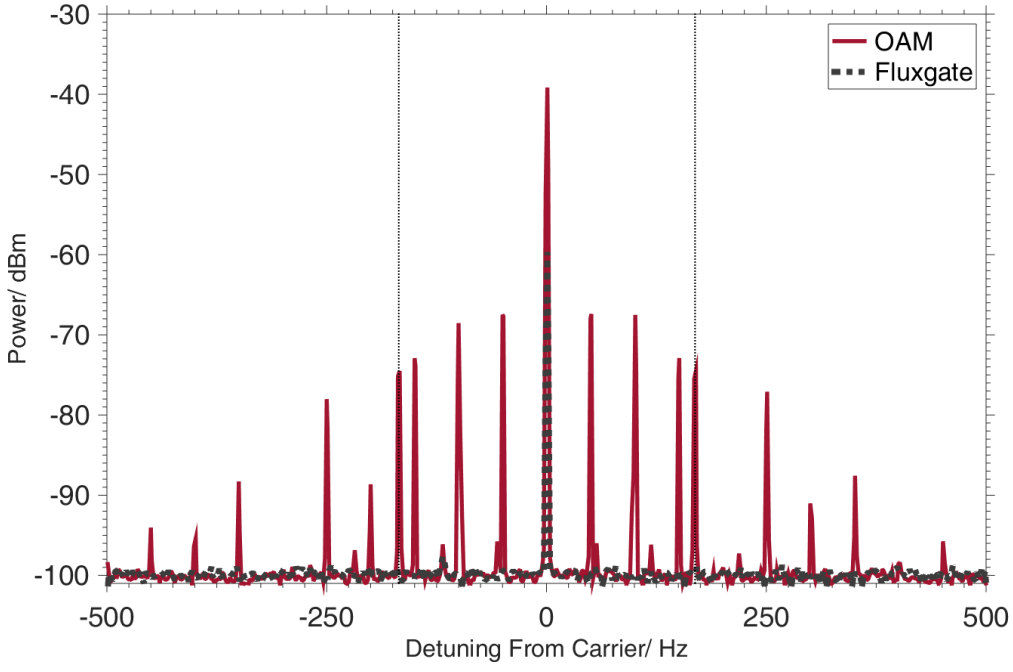

Figure IV.17: Spectra of the DC fan obtained when the OAM was driven at an arbitrary frequency of $3x10^4$, using the OAM (red trace) and FG (grey dotted trace). Only the OAM was able to detect the DC fan at this lower driving frequency as evidenced by the characteristic sideband peaks at $\pm(170 \pm 1)$.

4 Conclusions

Detection of rotating objects was successful in all orientations of the rotating Allen key with respect to the magnetometer, but only in orientation E for the steel EN19T and EN24T samples. The dead zones, or areas where the sensitivity is reduced are proposed to be due to the heading error of the device, the effects of which may be mitigated by building an entirely portable device which can be turned to face different directions. The reduced sensitivity is not so important in the present context here however, since the aim is to be able to detect objects much larger than the samples in the investigation.

The OAM was able to detect both DC and AC motors, and outperformed a commercial fluxgate magnetometer in the low frequency regime (less than 50 Hz). The detection manifested itself as sidebands of the driving peak, detectable at low frequency thanks to frequency mixing, which is especially useful in this regime. The frequency mixing seen in the OAM spectra is due to mixing in the atomic sample itself.

Frequency mixing also offers the advantage of tunability away from noise, which is prevalent in environments where rotating machinery would be in use, without the need for laborious screening methods. This tunability affords a better response in the low frequency regime compared to the commercial FG.

Successful demonstration of through wall detection makes the OAM a good candidate for remote and non-invasive detection of hard to reach or concealed machinery, for industrial or defence applications. The miniaturisation (with potential for further downscaling) and portability is a further advantage, which offers low power consumption as a byproduct.

Chapter V

Underwater Detection Using A Portable OAM

In the context of defence, security, and surveillance, building a completely self contained portable OAM device has distinct advantages over a static detector:

- Smaller and more compact systems tend to have **lower power consumption**, so smaller batteries may be used.
- Surveillance programs are more **cost-efficient** since the detector can be used and transported to several different sites, so fewer need to be purchased.
- Data retrieval can be more **time-efficient** if it is necessary to analyse information from more than one site.
- The use of lightweight materials in construction can be beneficial in building a **mobile** OAM in situations where a large or bulky target is situated in the dead zone. In this instance the OAM can be simply rotated.

In this investigation a light, completely portable and self contained OAM was built and its suitability for in-field marine applications was considered.

1 Modular Breadboard

To meet the specification for a lightweight and cost efficient device, a plastic breadboard was designed. The modular design lends some versatility to the shape of the finished optical bench, which can be constructed by connecting the breadboards with an M6 plastic screw.

Each breadboard has dimensions:

- Sides 200 x 200 mm
- Depth 21 mm
- Screw Holes M6
- Nut Size M6

The top side of the breadboard has evenly spaced non-threaded holes with which to clamp optical components using a plastic M6 screw:

- Hole Spacing 12.5 mm centre to centre
- Diameter 7 mm

On the bottom face, recesses were included in the design to hold hexagonal M6 plastic nuts, directly in line with the thread of the screws from above to secure them in place since the thread could not be printed. In the final construction, 9 breadboards were printed and connected to make a 600 x 600 mm square optical table, with a 600 x 600 mm perspex board attached on the underside for stability.

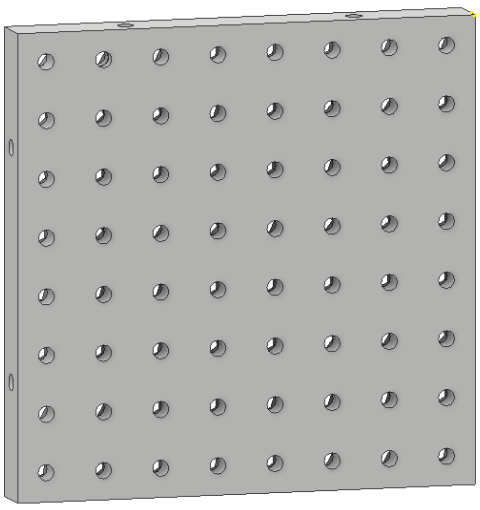

Figure V.1: Top view of single square breadboard part, with sides 200 mm long. Optical components are secured using an M6 screw and clamp, tightened with an M6 nut placed in recesses on the bottom face.

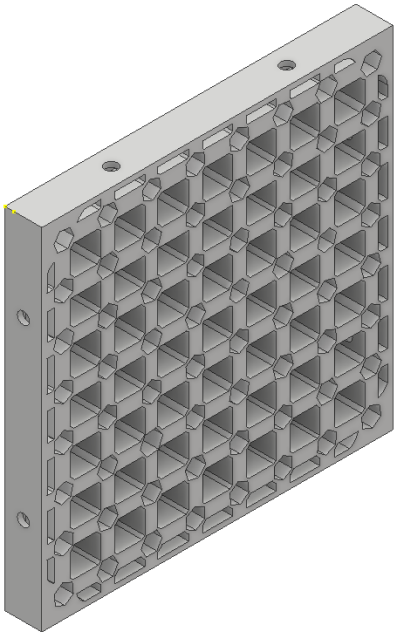

Figure V.2: Rear Face of 200 x 200 mm breadboard. Hexagonal recesses of side length 6 mm are used to secure screws coming in from the top.

2 OAM Sensor Unit With Compensation Coils

An entirely new, self-contained and free-standing OAM sensor unit bounded by an area measuring 165 x 165 x 145 mm was designed. The new unit has the addition of three sets of Helmholtz coils whose current supplies were configured to compensate for stray magnetic fields/ background magnetic noise.

Coil	Average Half-Side-Length (mm)	N Turns	Separation (mm)
Induction	27	20	27
B_0	68	20	68
B_x	60	15	60
B_y	40	10	40
B_z	85	15	85

Table V.1: The average half side length, separation and N turns of wire for each coil on the OAM sensor unit. These coils are the Bias coils (B_0 for optical pumping), the RF induction coil, and three further sets of square Helmholtz coils to compensate for stray magnetic fields in each of the x, y, z vector directions. Since the Bias coil is circular the 'average half-side length' is given by the diameter of this coil.

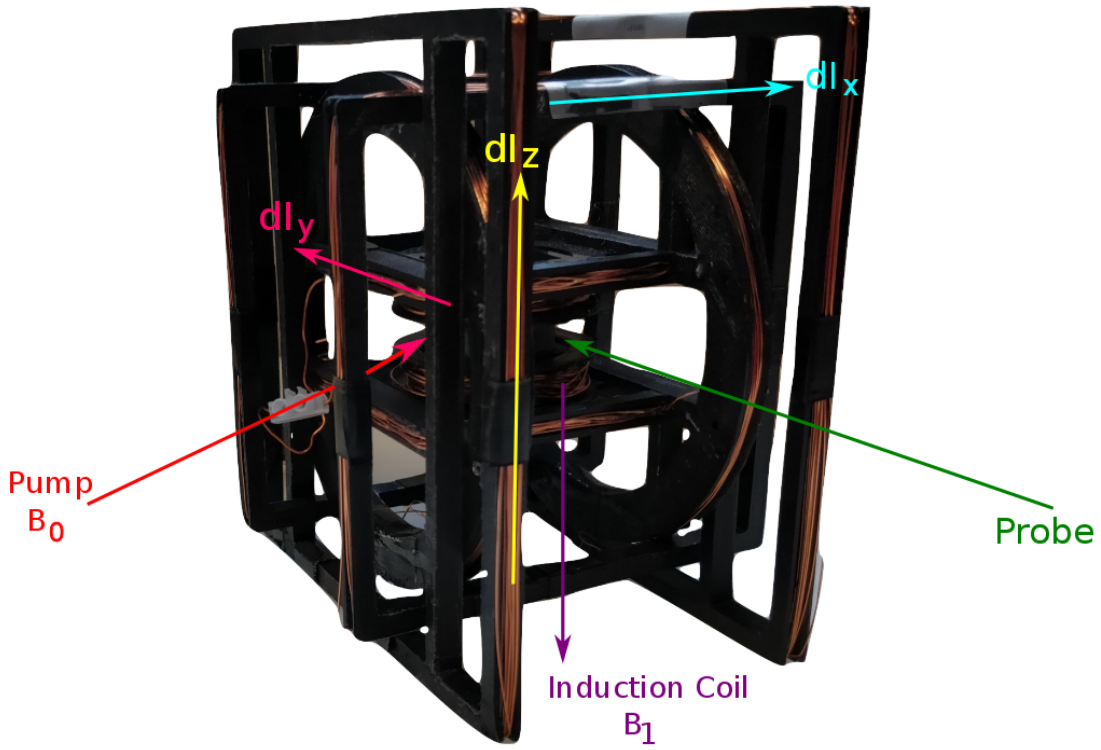

Figure V.3: 3D- printed OAM unit with compensation coils in the x,y and z directions. The unit is contained in an area of 165 x 165 x 145 mm, with the coils mounted as a single structure.

Table V.1 summarises the dimensions and separation of all coils comprising the unit. Square coils were printed for the compensation coils since the interconnection and overlap is more straight-forward to design and the overall unit is more robust and stable. In order to tune the compensation coils, the vapour cell was removed temporarily and replaced with a fluxgate magnetometer, which measured the magnetic field there when all coils, including the DC and induction coils were switched off. The compensation coils were then supplied the current needed to produce a magnetic field to oppose the background, which was calculated using equation III.5.

3 A Self-contained Magnetometer

The OAM sensor unit, ECDL, and optical components required for the DAVLL and setup of correct pump and probe beam intensities and polarisations were arranged in the MIT mode (see Chapter II) on the new breadboard. The whole breadboard was fully sealed with perspex walls and lid, with the electronics being stored separately on a wheeled trolley for ease of transport.

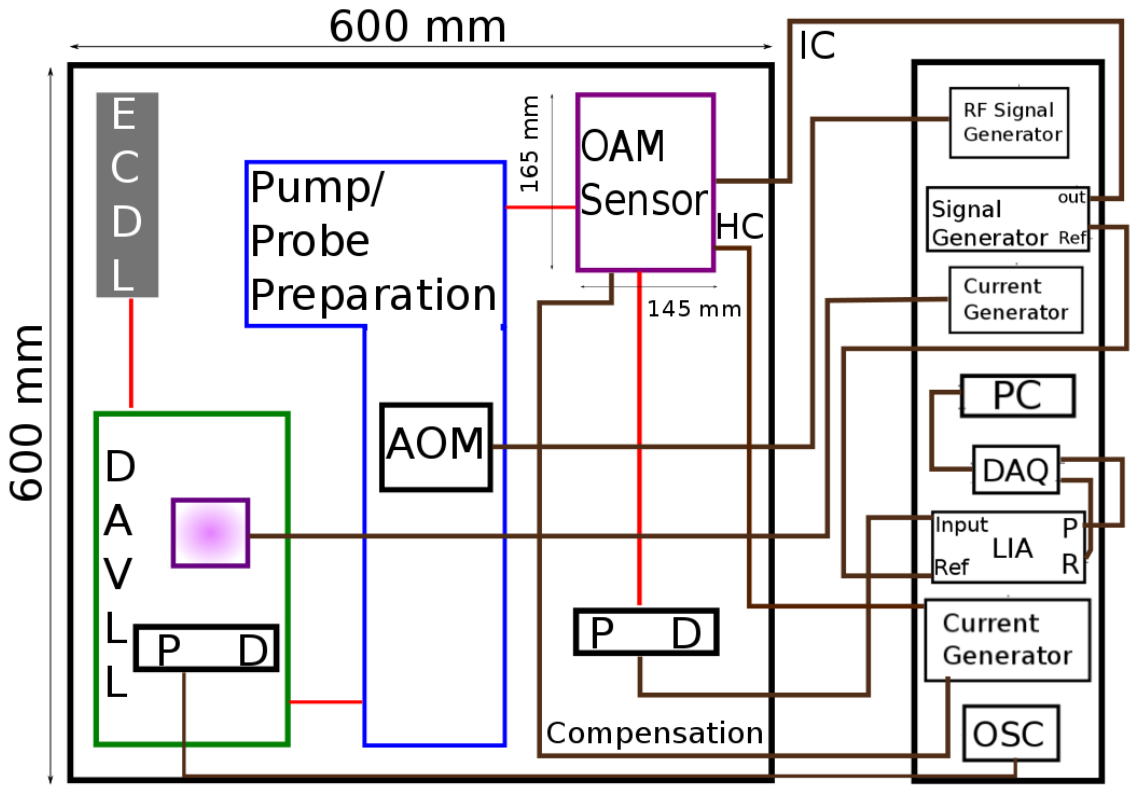

Figure V.4: Diagram to show relative positions of optical components contained on plastic breadboard and electrical equipment on a wheeled trolley. Key: ECDL is the extended cavity diode laser, PD is a balanced Photodiode, OSC is an oscilloscope, AOM is an Acousto-Optical Modulator, DAQ is a data acquisition board, LIA is a lock-in amplifier, IC the Induction Coil and HC a coil pair to provide a DC field. The DAVLL is used to lock the laser to the D2 F=4 $\rightarrow$ F'=4 ^{85}Rb transition and contained by the green boundary. The purple object in this container is a reference cell filled with rubidium, and has a coil wound round it connected to a DC current source in order to provide a DC magnetic field for Zeeman Splitting. Pump and probe preparation steps are as described in previous investigations, to set polarisation and intensity, with the pump and probe beams intersecting at a 90° angle in the centre of the vapour cell in the OAM sensor. Each compensation coil (one each in the x-,y-, and z- vector directions, with the z- being along the pump axis and the y-axis being along the direction of the AC field induced by the AC) is connected to an independent current source and may be set separately.

4 Detection of Submerged Objects

The OAM equipment (optics and electronics) was transported to a test lab in a weather-proof cabin free-floated on a quarry lake. The cabin was accessed via a steel platform from the bank, the position of which was prone to mechanical vibrations and oscillations. The OAM was placed against the inner wall of the cabin and its position is marked by the red dot in figure V.5. At this position the compensation calibration using a fluxgate magnetometer was performed. [1]

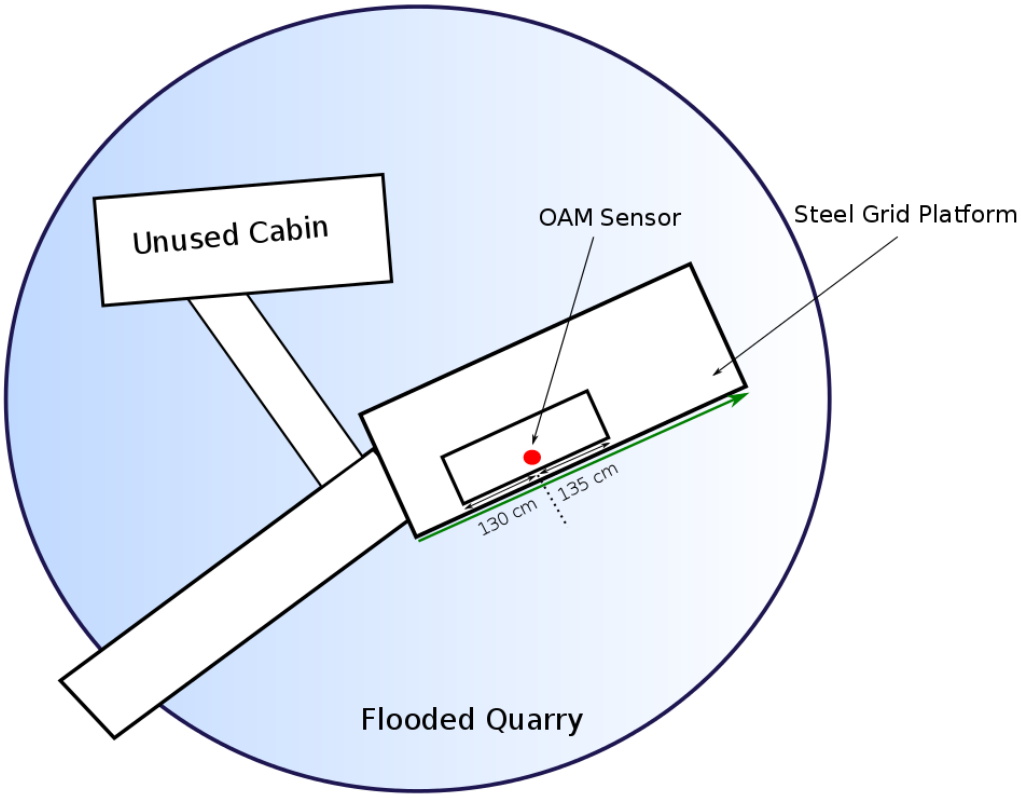

Figure V.5: Not to scale image of relative position of floating lab on quarry lake. The floating lab sits on a steel grid which is free to move along the water but remains fixed to the walkway from the bank. The sensor sits on the inside face of the wall closest to the axis along which a steel drum is dragged under the sensor (path of green arrow), and is (130 ± 5) cm and (135 ± 5) cm from the adjoining sides of the cabin.

[1] This investigation required a team effort and was carried out with thanks to Ferruccio Renzoni, Luca Marmugi, Cameron Deans, and Andrew Bond.

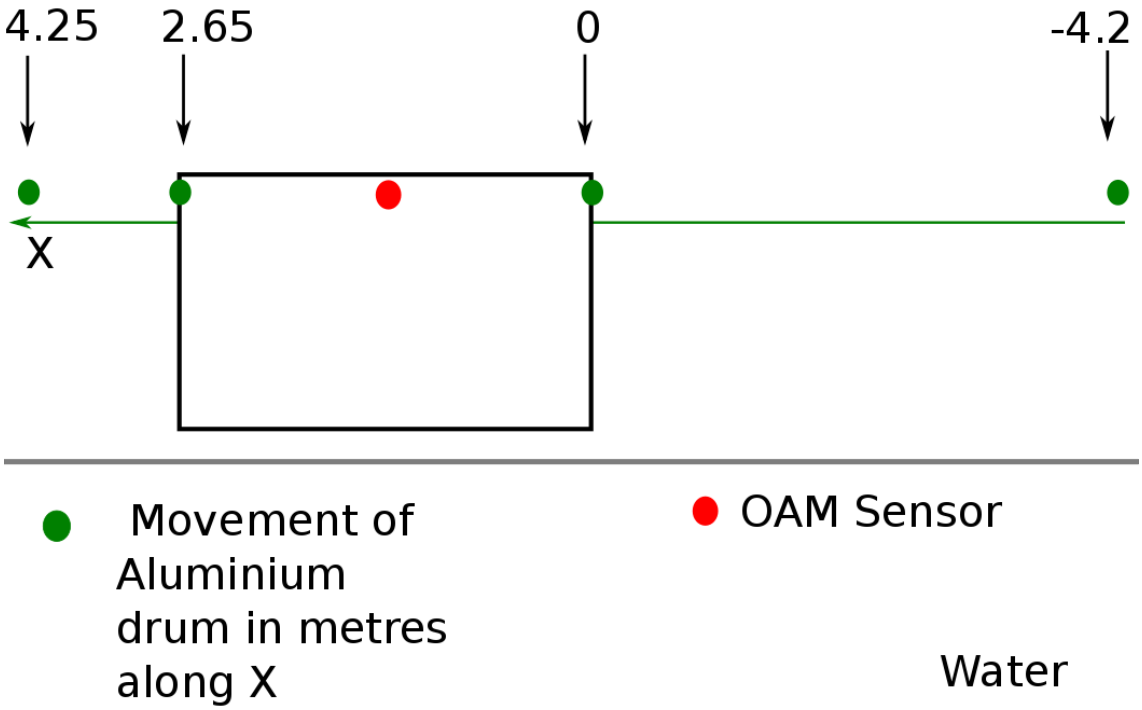

Figure V.6: Schematic to illustrate the relative positions of the OAM inside a floating lab and a floating aluminium drum. The drum was held at positions along green path for 60 seconds whilst the phase and radius from an LIA connected to the OAM was recorded at each position.

At different depths from 0.45 to 10 m (relative to the magnetometer height) an aluminium drum (with approximate dimensions of 1 m in length and radius 25 cm) was held at various positions along the path of the green arrow in figure V.5 in the water. The drum was able to pass directly underneath the magnetometer but it was not logistically possible to hold it in the position marked by the red marker (130 cm from the first wall of the cabin that the drum would pass).

At convenient positions between -4.2 m and +4.25 m from the OAM in the x-direction (see figure V.6) the drum was held for 60 seconds and the phase and radius of the magnetometer response at the lock-in was recorded for this whole period. Since the cabin was not fully fixed in position, it was difficult to take measurements for the same position at each depth. The LIA was configured to take a measurement every 20 ms, and the data were recorded on the laptop and then averaged. As previously, the phase voltage measurement corresponds to the phase lag of the polarimetry signal compared with the reference/ induction coil phase and the radius is the amplitude voltage measurement of the polarimetry signal.

4.1 Results

Phase and radius voltage were recorded for 60 seconds and averaged for a total of 3000 measurements over this period. Figs. V-26 depict the averaged phase and voltage readings when the drum was lowered to depths of 0.43, 0.45, 0.9, 2, 2.5, 3, 5, 7.5, and 10 m (depth measured when the drum was directly below the OAM sensor) and pulled on a pulley rope past the sensor. The error was calculated by taking the standard deviation for each averaged measurement, and a fit line was constructed for measurements outside of the region $0.3 \rightarrow 2.3$ m along x in figure V.6. The graphs are marked with a green dotted line which indicates the position of the sensor i.e. the point where the drum was directly below the sensor.

In tables V.2 and V.3 below, the point at which the magnetometer records the biggest percentage discreprancy with the line of best fit is listed for each depth and its position along x in figure V.6 noted. $\Delta\%$ was calculated by

$$\Delta\% = \frac{y_{\text{fit}} - y_{\text{P}}}{y_{\text{fit}}} \times 100 \ , \tag{V.1}$$

where y_{P} is the voltage measurement at position P, and y_{fit} is the voltage on the fit line also at position P.

Depth (m)	Δ (%)	Position (m)	Figure
0.43	0.79	0.35	V.7
0.45	4.21	0.5	V.9
0.95	1.12	1	V.11
2	0.98	1.85	V.13
2.5	1.17	1.85	V.15
3	0.79	0.5	V.17
5	1.46	0.5	V.21
7.5	1.72	2	V.23
10	1.02	1.85	V.25

Table V.2: Point at which the biggest percentage difference between phase voltage and best fit is elicited at magnetometer when the aluminium drum is detected at depths between 0.43 m and 10m.

Depth (m)	Δ (%)	Position (m)	Figure
0.43	4.65	0.35	V.8
0.45	7.19	0.5	V.10
0.95	2.4	1.85	V.12
2	19.9	1.85	V.14
2.5	0.212	1.5	V.16
3	17.6	0.5	V.18
5	0.5	0.5	V.22
7.5	1.34	2	V.24
10	1.49	1.85	V.26

Table V.3: Point at which the biggest percentage difference between radius voltage and best fit is elicited at magnetometer when the aluminium drum is detected at depths between 0.43 m and 10m.

In figures V.19 and V.20 there is an anomalous data point at $x = 1.85$ m, which has been removed in figures V.21 and V.22. This point is a large voltage drop compared with the surrounding points; a 36% drop in phase voltage and 67% drop in radius voltage, and is most probably an outlier or an error with the measurement software. Unfortunately, there was no time to repeat the measurement so the outlier has been removed to improve comparison between the 5 m and remaining depth measurements.

In general, from tables V.2 and V.3, when the drum is near the sensor (between positions 0 and 2 m), the voltage measurements of both the phase and radius exhibit the biggest deviation from the fit line. This suggests that the OAM is able to sense the presence of the drum, even if it is unable to localise it, with an error of $\pm$ 1 m. The best examples of this is at 0.45 m deep and $x = 0.5$ m in the phase, and 2 m deep and $x = 1.85$ m, and 3 m deep and x= 0.5 m in the radius. However, there is little consistency with this data; it would be expected that the phase and radius measurements both would show closer agreement with regards to the most likely position of the drum at x but this differs; it is either at $x = 1.85$ m or $x = 0.5$ m . This difference in perception of where the drum is located may be due to the fact that the platform, the drum and indeed any noise-inducing structures are all floating about in the water, with varying debris at different depths. The floating platform may also introduce heading errors in addition.

The detection of the drum appears to be clustered around $x = 1.5$ - 2 m or $x = 0.35$ - 0.5 m. This makes sense, but the large voltage changes near $x = 0$ may be attributed to the fact that at there is an unknown object here whose conductive signal is also being

picked up by the magnetometer. In fact, in the graphs for 0.95, 2 , 2.5, 7.5 and 10 m deep there is an additional noticeable voltage drop at around $x = 0$ which could be caused by the object.

Standard deviation generally increases with depth, which is understandable considering the magnetic signal is dampened as z^{-3} for a coil, as per equation III.4. The errorbars are particularly large when the aluminium drum was lowered beyond 5 m. However, the error is also large at a depth of 2.5 m. The 2.5, 5, 7.5 and 10 m depth measurements were taken the day after the remaining ones and this could explain the larger deviation. In part, the weather may have played a role – stronger wind made the surface of the water choppier, moving the cabin more, thus affecting the shallower depth measurement more strongly than the others.

Overall, the Δ% phase data are pretty consistently between 0.79 and 1.46 % with a jump to a 4.21 % change at 0.45 m, with no obvious trend in the data. Similarly there is no definite behaviour model for the radius data (since a reduction in signal change may be expected at lower depths due to the range of the RF coil).

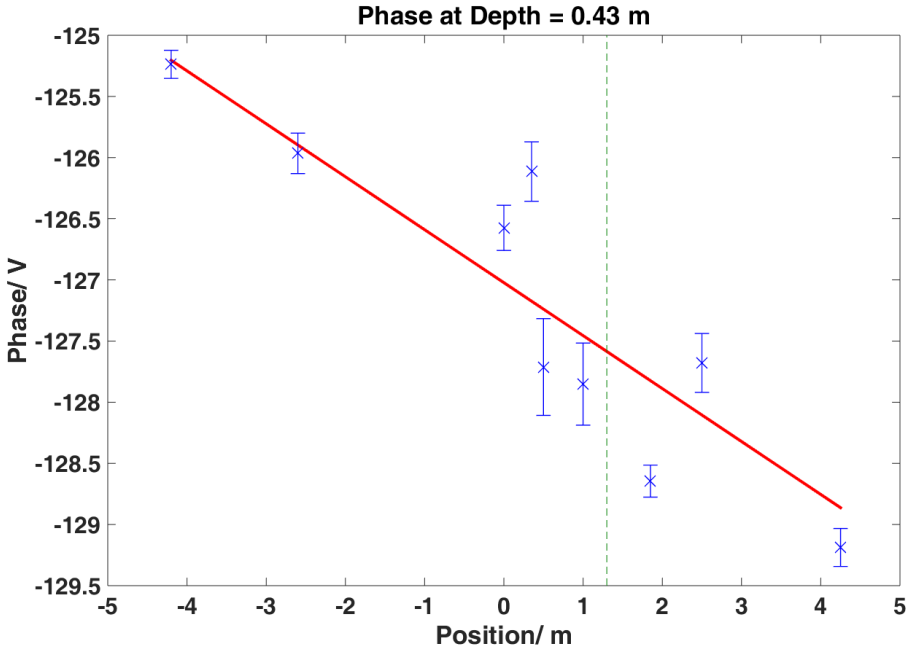

Figure V.7: Graph to show variation in phase voltage measurements when an aluminium drum was dragged in a straight line at 0.43 metres when it was directly below the OAM. The red line indicates the position of the OAM sensor relative to the drum, at 1.3 metres past the first wall of the floating cabin it is contained in that the drum goes under.

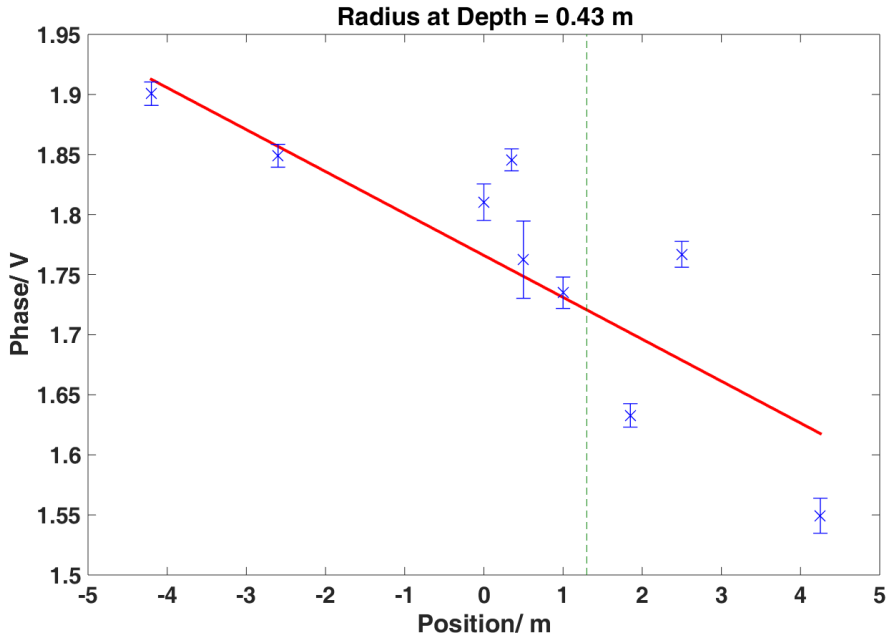

Figure V.8: Graph to show variation in radius voltage measurements when an aluminium drum was dragged in a straight line at 0.43 metres when it was directly below the OAM. The green line indicates the position of the OAM sensor relative to the drum, at 1.3 metres past the first wall of the floating cabin it is contained in that the drum goes under.

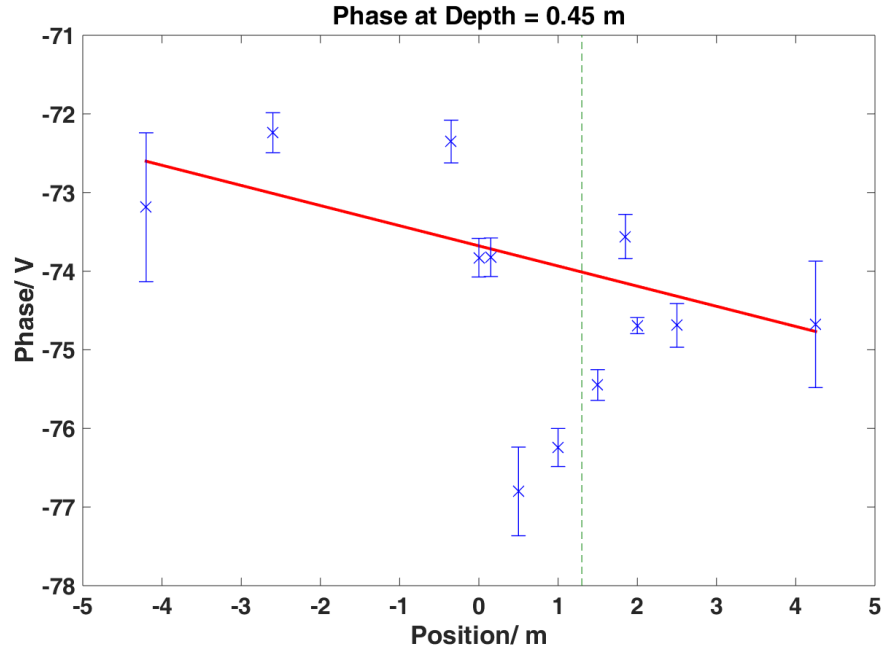

Figure V.9: Graph to show variation in phase voltage measurements when an aluminium drum was dragged in a straight line at 0.45 metres when it was directly below the OAM. The green line indicates the position of the OAM sensor relative to the drum, at 1.3 metres past the first wall of the floating cabin it is contained in that the drum goes under.

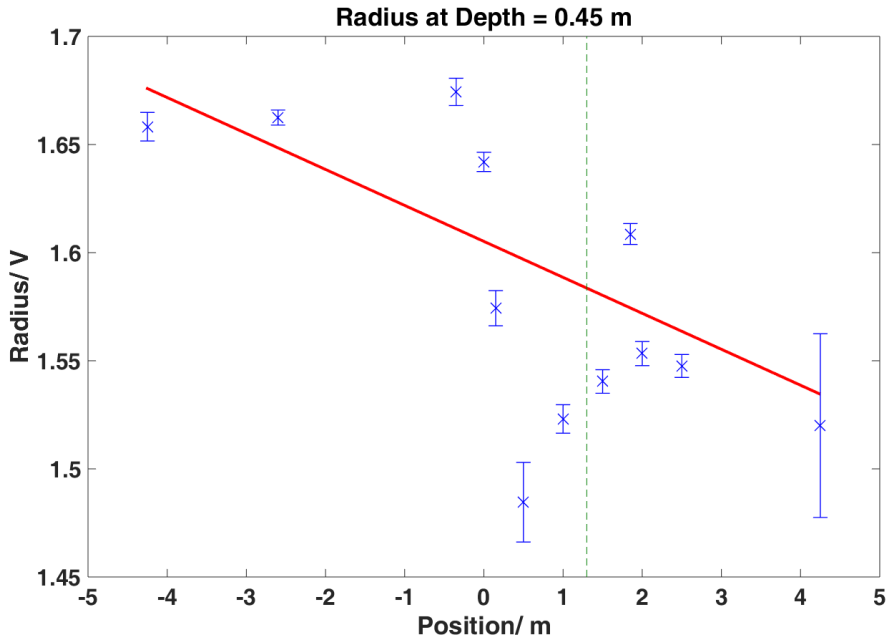

Figure V.10: Graph to show variation in radius voltage measurements when an aluminium drum was dragged in a straight line at 0.45 metres when it was directly below the OAM. The green line indicates the position of the OAM sensor relative to the drum, at 1.3 metres past the first wall of the floating cabin it is contained in that the drum goes under.

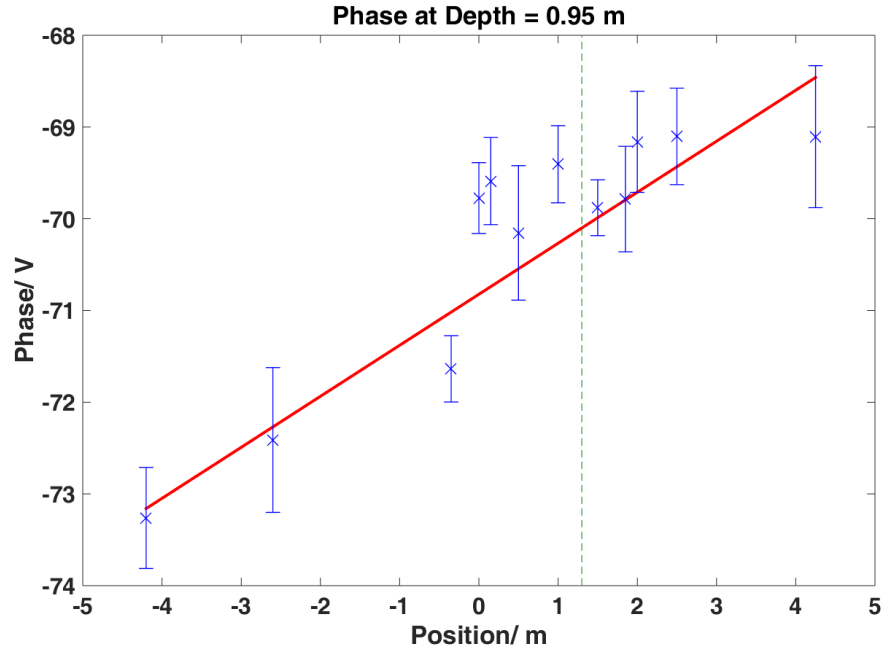

Figure V.11: Graph to show variation in phase voltage measurements when an aluminium drum was dragged in a straight line at 0.9 metres when it was directly below the OAM. The green line indicates the position of the OAM sensor relative to the drum, at 1.3 metres past the first wall of the floating cabin it is contained in that the drum goes under.

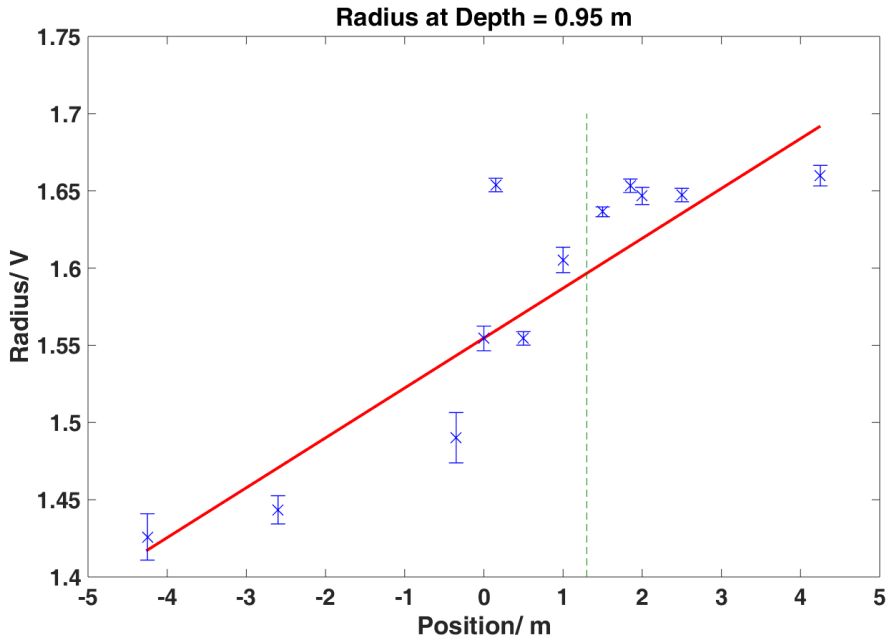

Figure V.12: Graph to show variation in radius voltage measurements when an aluminium drum was dragged in a straight line at 0.9 metres when it was directly below the OAM. The green line indicates the position of the OAM sensor relative to the drum, at 1.3 metres past the first wall of the floating cabin it is contained in that the drum goes under.

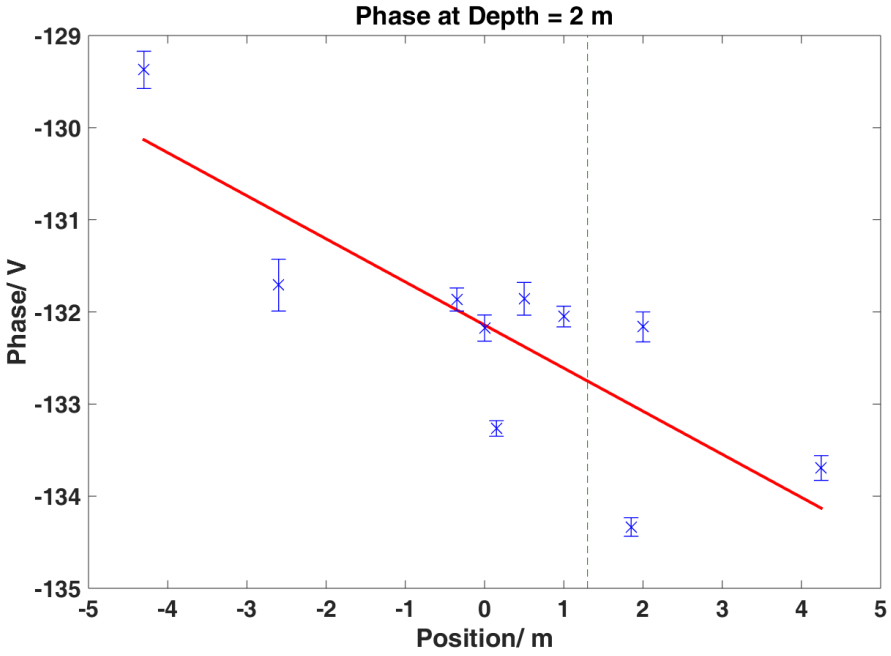

Figure V.13: Graph to show variation in phase voltage measurements when an aluminium drum was dragged in a straight line at 2 metres when it was directly below the OAM. The green line indicates the position of the OAM sensor relative to the drum, at 1.3 metres past the first wall of the floating cabin it is contained in that the drum goes under.

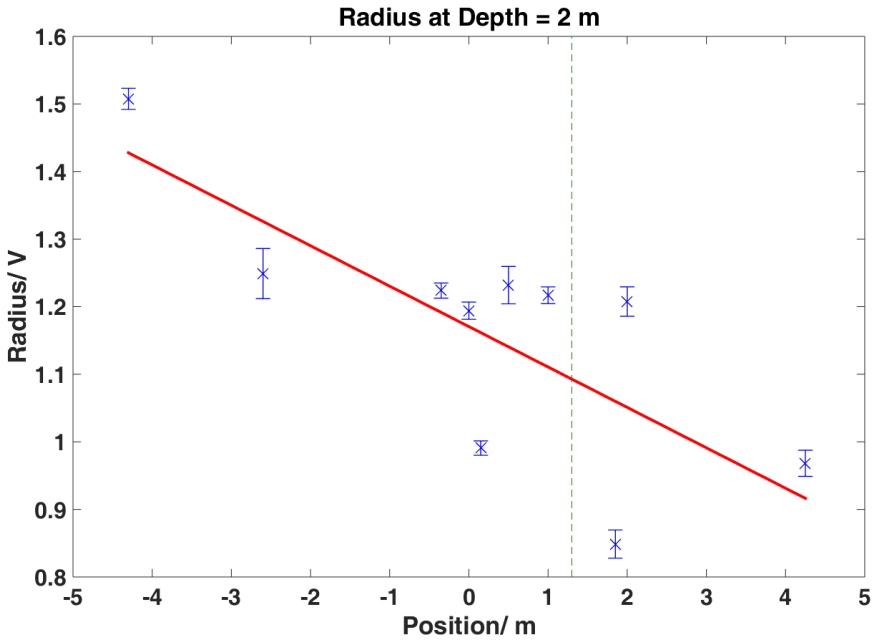

Figure V.14: Graph to show variation in radius voltage measurements when an aluminium drum was dragged in a straight line at 2 metres when it was directly below the OAM. The green line indicates the position of the OAM sensor relative to the drum, at 1.3 metres past the first wall of the floating cabin it is contained in that the drum goes under.

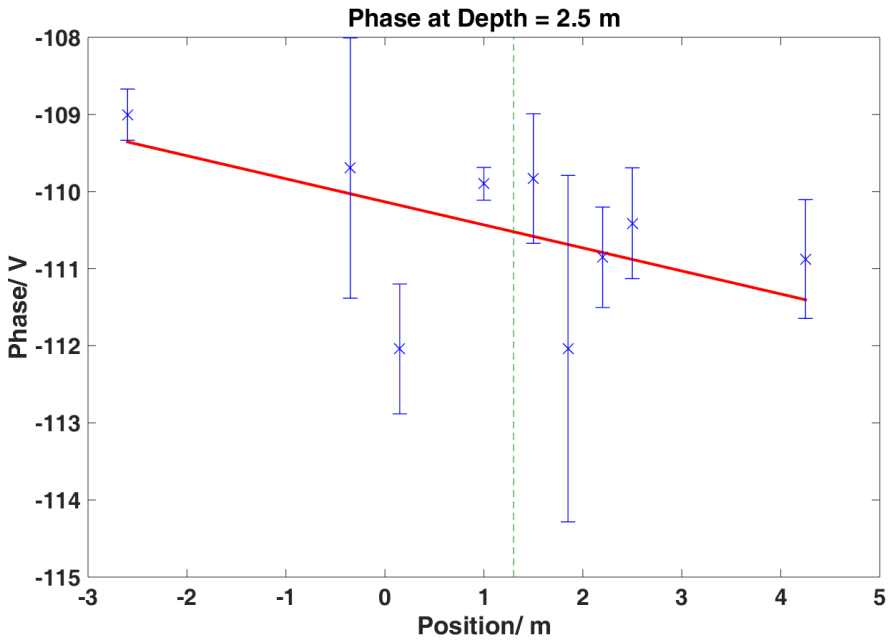

Figure V.15: Graph to show variation in phase voltage measurements when an aluminium drum was dragged in a straight line at 2.5 metres when it was directly below the OAM. The green line indicates the position of the OAM sensor relative to the drum, at 1.3 metres past the first wall of the floating cabin it is contained in that the drum goes under.

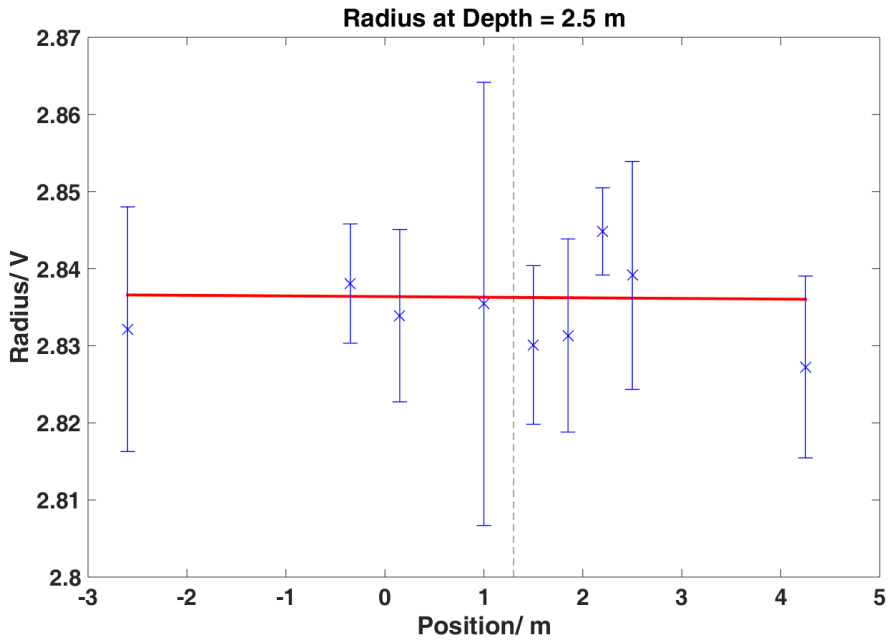

Figure V.16: Graph to show variation in radius voltage measurements when an aluminium drum was dragged in a straight line at 2.5 metres when it was directly below the OAM. The green line indicates the position of the OAM sensor relative to the drum, at 1.3 metres past the first wall of the floating cabin it is contained in that the drum goes under.

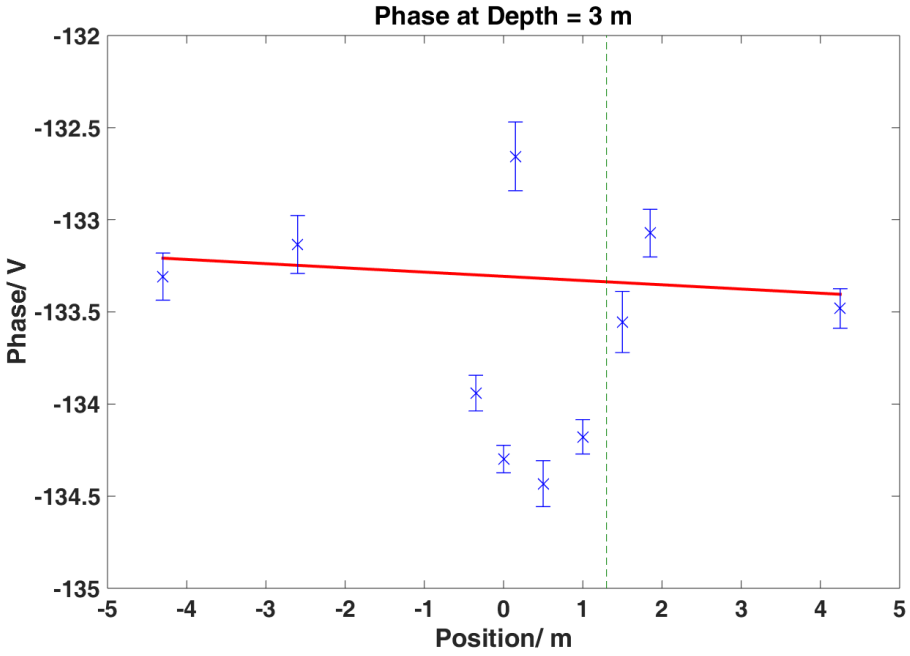

Figure V.17: Graph to show variation in phase voltage measurements when an aluminium drum was dragged in a straight line at 3 metres when it was directly below the OAM. The green line indicates the position of the OAM sensor relative to the drum, at 1.3 metres past the first wall of the floating cabin it is contained in that the drum goes under.

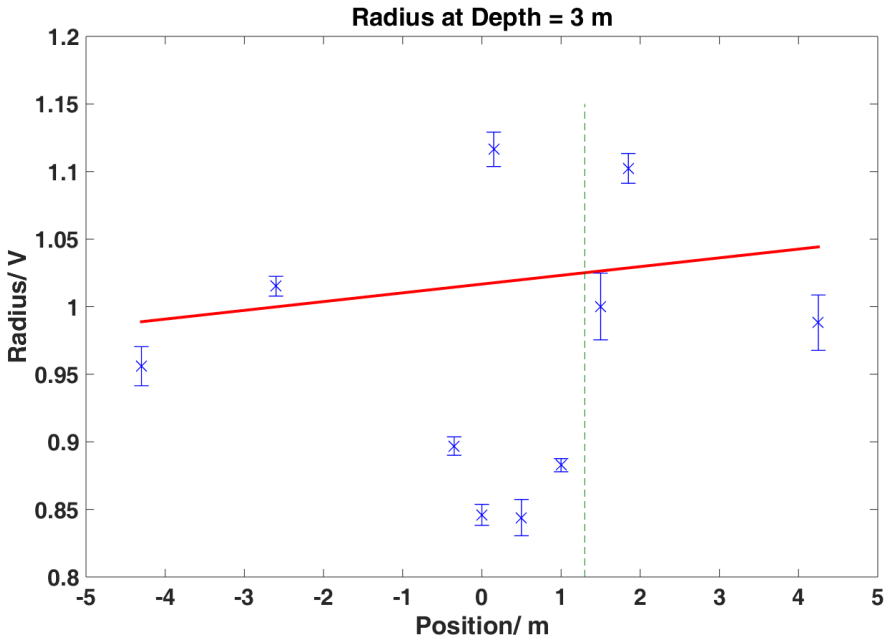

Figure V.18: Graph to show variation in radius voltage measurements when an aluminium drum was dragged in a straight line at 3 metres when it was directly below the OAM. The green line indicates the position of the OAM sensor relative to the drum, at 1.3 metres past the first wall of the floating cabin it is contained in that the drum goes under.

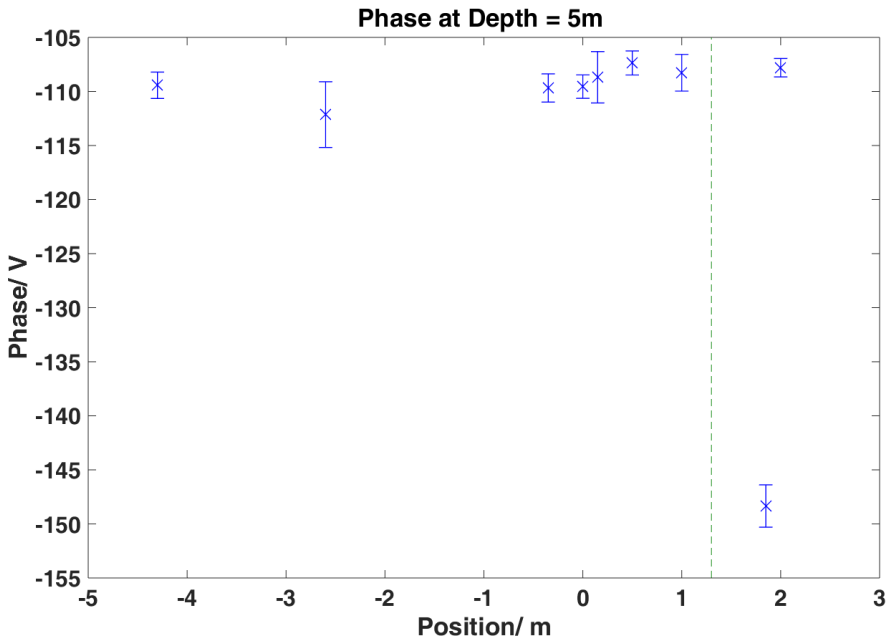

Figure V.19: Graph to show variation in phase voltage measurements when an aluminium drum was dragged in a straight line at 5 metres when it was directly below the OAM. The green line indicates the position of the OAM sensor relative to the drum, at 1.3 metres past the first wall of the floating cabin it is contained in that the drum goes under.

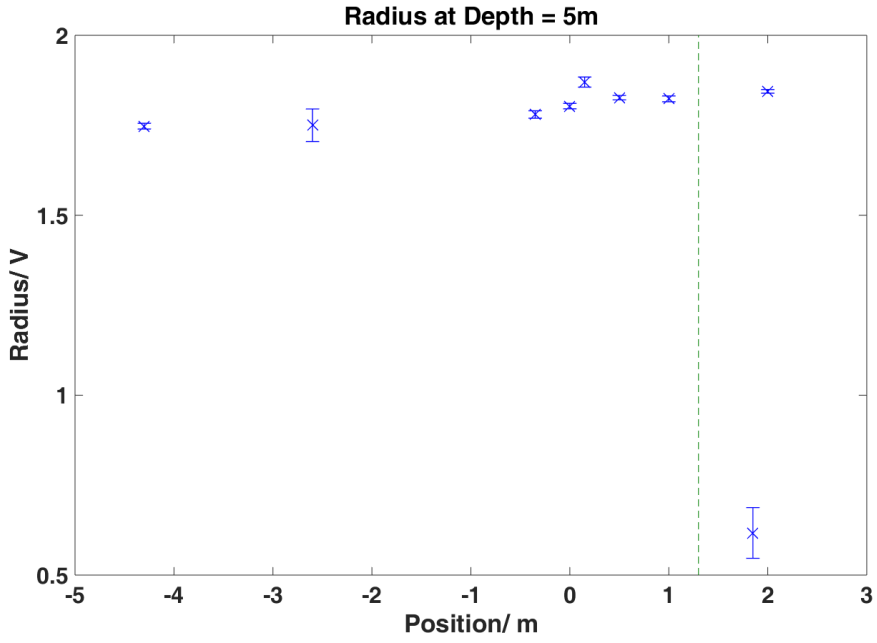

Figure V.20: Graph to show variation in radius voltage measurements when an aluminium drum was dragged in a straight line at 5 metres when it was directly below the OAM. The green line indicates the position of the OAM sensor relative to the drum, at 1.3 metres past the first wall of the floating cabin it is contained in that the drum goes under.

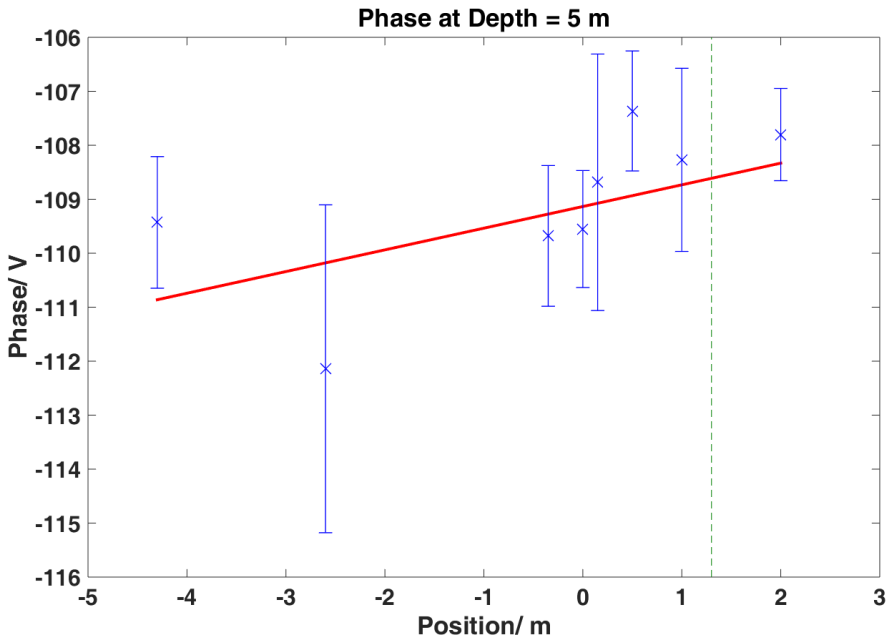

Figure V.21: Graph to show variation in phase voltage measurements when an aluminium drum was dragged in a straight line at 5 metres when it was directly below the OAM. The anomaly in the 'raw' data has been removed for comparison. The green line indicates the position of the OAM sensor relative to the drum, at 1.3 metres past the first wall of the floating cabin it is contained in that the drum goes under.

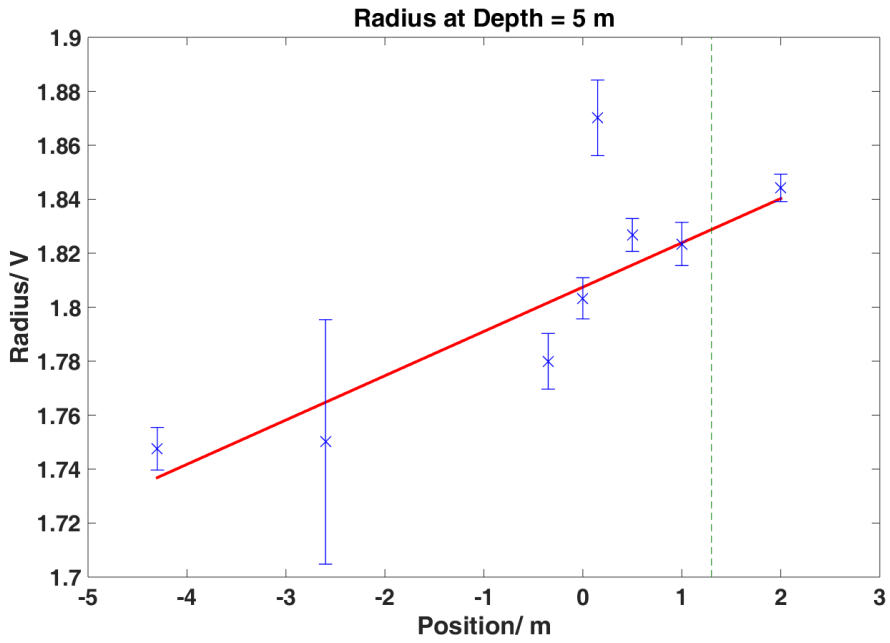

Figure V.22: Graph to show variation in radius voltage measurements when an aluminium drum was dragged in a straight line at 5 metres when it was directly below the OAM. The anomaly in the 'raw' data has been removed for comparison. The green line indicates the position of the OAM sensor relative to the drum, at 1.3 metres past the first wall of the floating cabin it is contained in that the drum goes under.

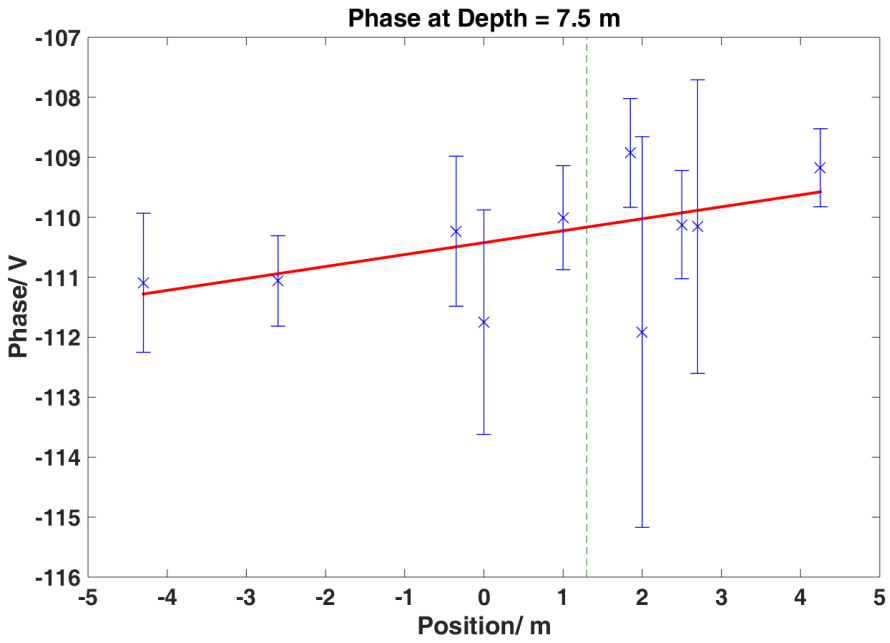

Figure V.23: Graph to show variation in phase voltage measurements when an aluminium drum was dragged in a straight line at 7.5 metres when it was directly below the OAM. The green line indicates the position of the OAM sensor relative to the drum, at 1.3 metres past the first wall of the floating cabin it is contained in that the drum goes under.

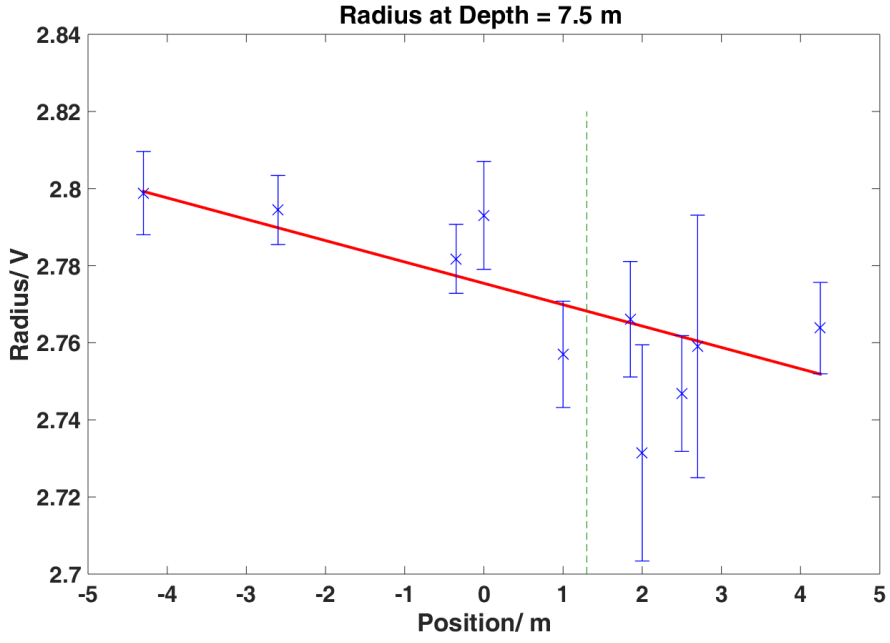

Figure V.24: Graph to show variation in radius voltage measurements when an aluminium drum was dragged in a straight line at 7.5 metres when it was directly below the OAM. The green line indicates the position of the OAM sensor relative to the drum, at 1.3 metres past the first wall of the floating cabin it is contained in that the drum goes under.

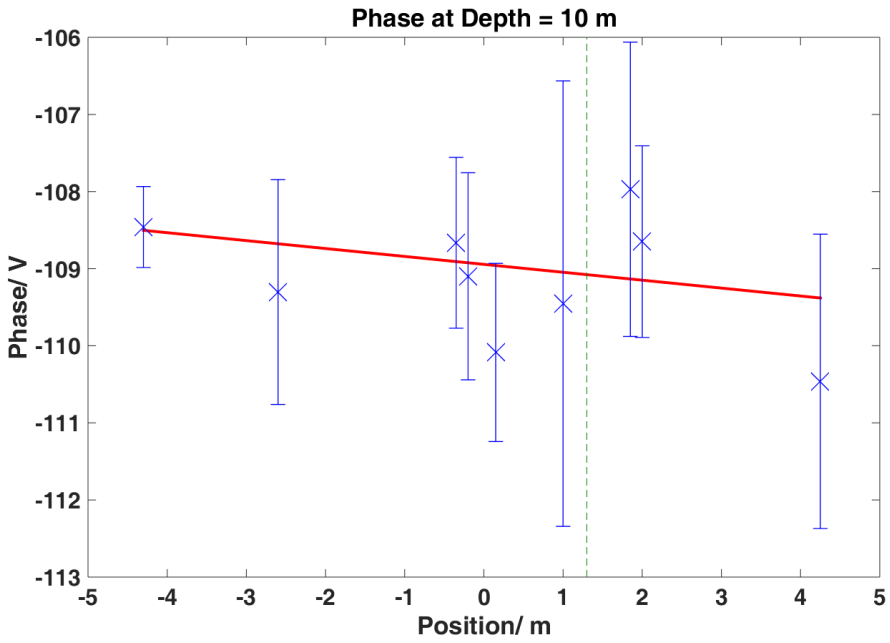

Figure V.25: Graph to show variation in phase voltage measurements when an aluminium drum was dragged in a straight line at 10 metres when it was directly below the OAM. The green line indicates the position of the OAM sensor relative to the drum, at 1.3 metres past the first wall of the floating cabin it is contained in that the drum goes under.

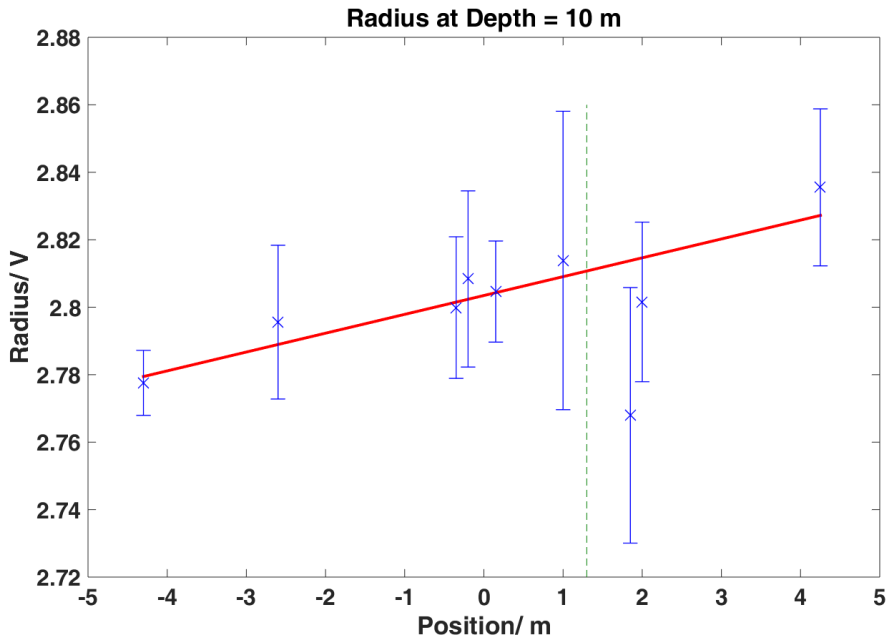

Figure V.26: Graph to show variation in radius voltage measurements when an aluminium drum was dragged in a straight line at 10 metres when it was directly below the OAM. The green line indicates the position of the OAM sensor relative to the drum, at 1.3 metres past the first wall of the floating cabin it is contained in that the drum goes under.

In figures V.27 and V.28, the voltage difference between successive measurement positions is plotted and is defined by

$$\Delta \mathrm{V} = \mathrm{V}_i - \mathrm{V}_{i-1} \ . \tag{V.2}$$

ΔV was plotted for radius and phase at the different depths. An offset was applied to the plots for clarity and purposes of comparison, and a dashed red line included to mark the position of the sensor.

In the phase difference data, a somewhat consistent dip can be seen for all depths at x = 1.8 m – just after the drum passes the sensor. This could very well be attributed to a detection of the drum.

At x = 0.3 - 0.4 m there also appears to be a change (negative or positive) in voltage in both phase and radius for ΔV. This effect is most pronounced at a depth of 0.45 which is consistent for the Δ (%) data for phase in table V.2, but not for the corresponding radius results. Since this is near position 0 at the corner of the cabin, this could be electrical noise from the cabin itself or some junk attached to this part of the platform.

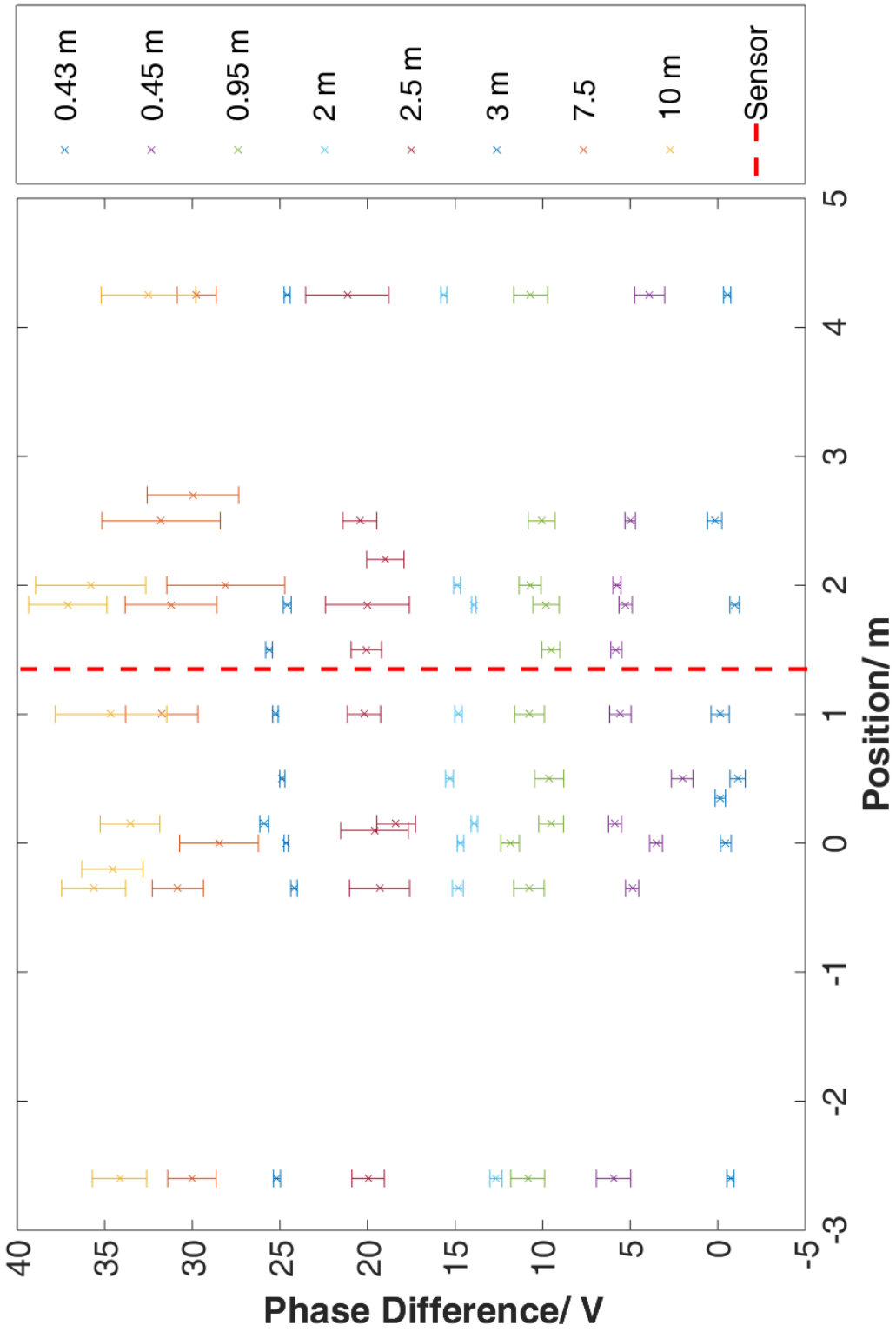

Figure V.27: Difference between successive phase measurements along x at different depths between 0.43 m and 10 m of the aluminium drum. The error bars are given by the standard deviation. An offset of an extra $+n$ 5 V is applied for each data set for clarity, with the measurement at 5m deep being purposefully ommitted.

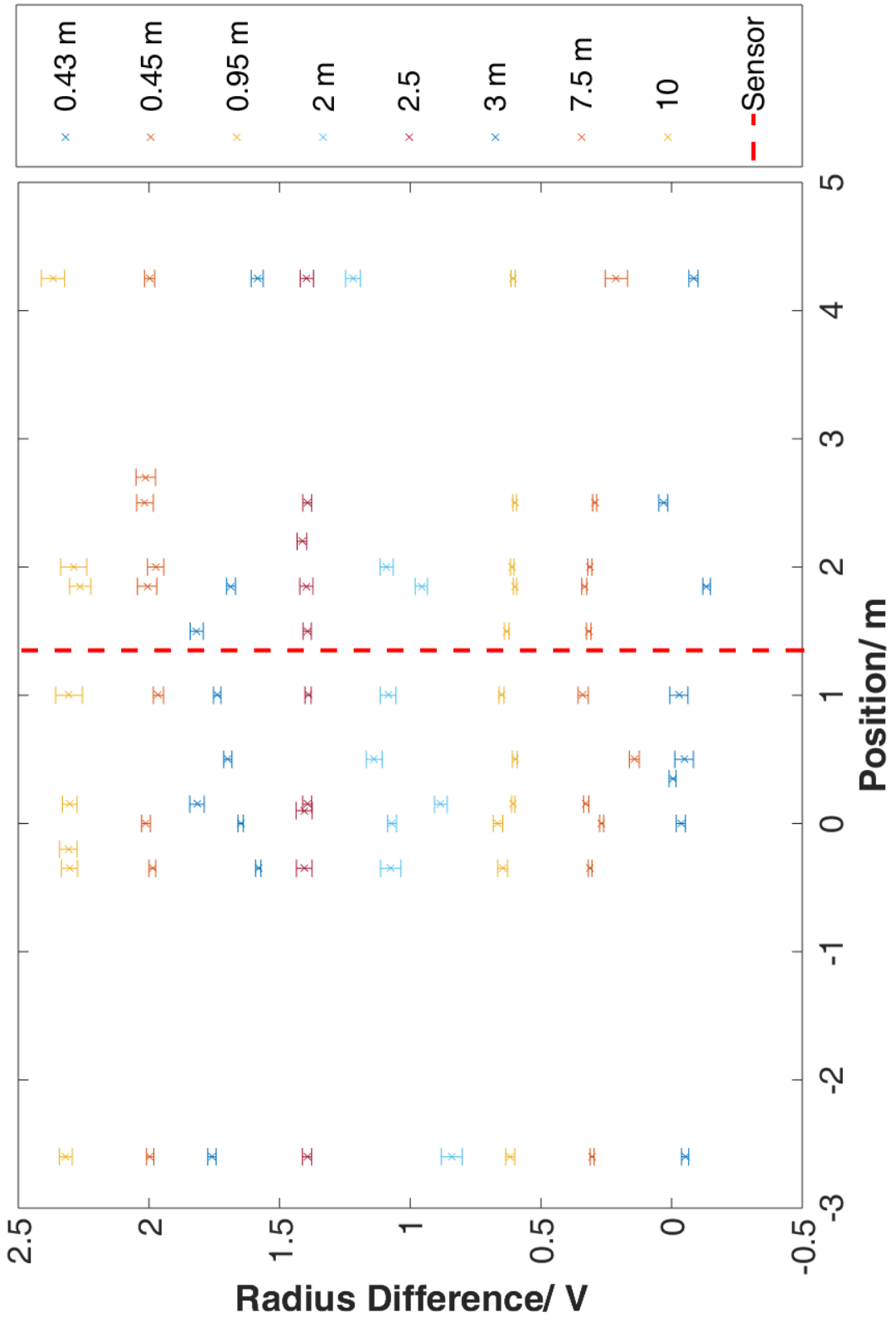

Figure V.28: Difference between successive radius measurements along x at different depths between 0.43 m and 10 m of the aluminium drum. The error bars are given by the standard deviation. An offset of an extra $+n$ 0.3 V is applied for each data set for clarity, with the measurement at 5m deep being purposefully ommitted.

5 Conclusions

The OAM size was further reduced to a sealed, self-contained optics table measuring 60 cm × 60 cm. Since the breadboard was plastic, it was light and easily portable, making it suitable for transportation and use across multiple sites and facilities. The electronics footprint has the potential to be reduced simply by purchasing smaller equipment, which could also reduce power consumption.

The OAM exhibited changes in voltage most likely due to the drum (and less likely to be potentially due to noise) when the drum was situated within 1 m of the magnetometer - proving its potential in prospective tomography applications for mapping the contents of bodies of water. This could be useful to be able to image the surrounding area of some sunken object prior to a retrieval operation, which could be costly or dangerous. The full range of the magnetometer was not explored but this is promising. Further investigation into hardware upgrades to the magnetometer i.e. how coil shape can affect detection range for example should be sought. Then, the possibility for use in long range detection such as submarines may be considered.

The phase measurements in general, in the difference data are slightly clearer and more consistent. However, the errors on phase measurements are larger. Since they are a standard deviation this indicates that the phase is more sensitive to foreign objects and debris, as the phase data are spread over a larger range. The phase data are purely imaginary (from equation III.1), compared to the radius dependence on the relative permittivity (of water, in this case). This means the radius measurement for the same object and a comparative distance will be influenced by environmental factors such as boundaries and temperature [119].

Unfortunately, due to the nature of the experiment, direct comparison in controlled conditions was not possible in the time allotted for operation at the quarry. In this instance, it is clear that the optimum magnetometer operation is adversely affected by temperature change (as expected for lasers), interference from debris and possible heading errors since the platform was not fixed. However, this real-time in-field investigation shows that even in these instances, these factors do not fatally impair the ability of the magnetometer to detect underwater conductive objects, even if the results do not point to a conclusive detection of the drum. With further investigation into how to reduce the effects of these variables, the OAM has the promising capability for an underwater or boat-mountable imaging device or detector.

Chapter VI

Summary and Outlook

This thesis details the development of an RF-magnetometer for security and surveillance purposes, with the main considerations being geared towards portability, user-friendliness, and the possibility of operation at room temperature with no need for shielding. These conditions were set out as an alternative to the existing gold standard in magnetic sensing – SQUID. However, this device is expensive, requires cryogenic cooling, and shielding.

The OAM sensor component in all incarnations of the RF-magnetometer used in these investigations required a circularly polarised pump beam, a DC homogeneous magnetic field, an Rb vapour cell and a linearly polarised probe beam for operation. In the first experiment, an OAMMIT device was built to image small aluminium shapes, which was repeated with the addition of an aluminium barrier. The OAMMIT was able to image concealed copper targets, with the phase maps being more accurately representative of size and shape.

The OAMMIT was modified by instead feeding the magnetometer output to a spectrum analyser to detect the magnetic signatures of rotating motors. This could be useful in industrial monitoring and detection of concealed machinery. The support unit was also replaced by a custom 3D-printed coil and sensor support. Conductive and magnetic objects were mounted on a manual motor and compared to a spinning bicyle wheel, electrical DC fan, and electrical AC fan. The OAM was able to detect these as sidebands of the induction frequency, at certain orientations of the object relative to the sensor. The results also indicated that the OAM was able to to outperform a fluxgate at lower operation frequencies.

The final investigation was the detection of an aluminium drum suspended in a deep quarry. To test this capability, the OAM was upgraded to include a more robust sensor and mounted on a plastic breadboard so that it was self-contained and portable. The relative instability of the platform the magnetometer was mounted on and temperature

and weather changes made it difficult to compare data directly and definitively address whether it was able to localise the drum.

The next steps for the magnetometer, from a defence point of view, would be further miniaturisation so that it is easier to use in the field. This may be achieved by designing printable optics posts and clamps so that components are able to be installed with closer spacing. This also has the advantage of being lighter, and since it reduces the amount of conductive metal in the vicinity of the OAM, the signal would be subject to less environmental noise.

Since the range of the magnetometer in the detection of rotating machinery was only explored upto 2 m away, investigations into how induction coil geometries, voltage supply, frequency and other parameters which may not be currently considered affect the detection range of the magnetometer.

It would also be of advantage to quantify the sensitivity of the magnetometer, in order to compare it to other types of magnetometer which are used for the same purpose (such as search coil magnetometers in non-destructive testing). This also would help keep track of how modifications to improve portability and user-friendliness affect the sensitivity.

Adding automation in the tomography modality by installing a stepper motor, for example, would improve the integrity of images, by removing the problems associated with manual movement of the translation stage. Since it was promising that the OAMMIT was able to image concealed objects, it would be interesting to extend this work by imaging through thick ($\geq 20\ mm$) barriers.

Bibliography

[1] Faraday, M., "On the magnetization of light and the illumination of magnetic lines of force c. 1," *Experimental Researches in Electricity* **136**, 1–20 (11 1846).

[2] Dehmelt, H., "Paramagnetic resonance reorientation of atoms and ions aligned by electron impact," *Physical Review* **103**, 1125–1126 (08 1956).

[3] Dehmelt, H., "Modulation of a light beam by precessing absorbing atoms," *Physical Review* **105**, 1924–1925 (03 1957).

[4] Bell, E. and Bloom, A., "Optical detection of magnetic resonance in alkali metal vapor," *Physical Review* **107**, 1559–1565 (09 1957).

[5] Budker, D. and Kimball, D. F. J., [*Optical Magnetometry*], 3, Cambridge University Press (2013).

[6] Budker, D. and Romalis, M., "Optical magnetometry," *Nature* , 227–234 (04 2007).

[7] Kitching, J., Knappe, S., and Donley, E., "Atomic sensors- a review," *IEEE Sensors Journal* **11**(9), 1749–1758 (2011).

[8] Beltrametti, E. and Levy-Leblond, J., [*Advances in Quantum Phenomena*], Springer Science and Business Media (1994).

[9] Major, F., [*The Quantum Beat: The Physical Principles of Atomic Clocks*], 122, Springer (1998).

[10] Marmugi, L., Hussain, S., Deans, C., and Renzoni, F., "Magnetic induction imaging with optical atomic magnetometers: Towards applications to screening and surveillance," *Proceedings SPIE* **9652**, 965209 1–11 (2015).

[11] Happer, W. and Mathur, B., "Off-resonant light as a probe of optically pumped atoms," *Physical Review Letters* **18**, 577–580 (04 1967).

[12] Brossel, J. and Bitter, F., "A new "double resonance" method for investigating atomic energy levels. Application to Hg $^3P_1$," *Physical Review* **86**, 308–316 (May 1952).

[13] Kominis, I., Kornack, T., Allred, J. ., and M.V., R., "A subfemtotesla multichannel atomic magnetometer," *Nature* **422**, 596–599 (02 2003).

[14] Allred, J. and Lyman, R., "High-sensitivity atomic magnetometer unaffected by spin-exchange relaxation," *Physical Review Letters* **89**, 130801 (2 2002).

[15] Groeger, S., Pazgalev, A., and Weis, A., "Comparison of discharge lamp and laser pumped cesium magnetometers," *Applied Physics B Lasers and Optics* **80**, 645–654 (3 2005).

[16] Haken, H. and Wolf, H., [*The Physics of Atoms and Quanta, Introduction to experiments and Theory, Sixth Edition*], Springer (2000).

[17] Andrews, D. and Babiker, M., [*The Angular Momentum of Light*], Cambridge University Press (2013).

[18] Budker, D. and Romalis, M., "Optical magnetometry," *Nature* **9**, 227–234 (04 2007).

[19] Wolf, E. et al., [*Progress in Optics*], 104, Elsevier (2006).

[20] Happer, W. and Mathur, B., "Effective operator formalism in optical pumping," *Physical Review* **163**, 12,25 (11 1967).

[21] Fox, M., [*Quantum Optics, An Introduction*], 56, Oxford University Press (2009).

[22] Kakkar, R., [*Atomic and Molecular Spectroscopy, Basic Concepts and Applications*], 24, Cambridge Univeristy Press (2015).

[23] Thyagarajan, K. and Ghatak, A., [*Lasers, Fundamentals and Applications*], 77, Springer, 2 ed. (2010).

[24] Bernath, P., [*Spectra of Atoms and Molecules*], 28, Oxford University Press, 2 ed. (2005).

[25] Hess, S., "Kinetic theory of spectral line shapes. the transition between doppler broadening and collisional broadening," *Physica* **61**, 80–94 (09 1971).

[26] Fox, M., [*Quantum Optics, An Introduction*], 58, Oxford University Press (2009).

[27] Corney, A., [*Atomic and Laser Spectroscopy*], Oxford Classic Texts (2006).

[28] Steck, D., "87 d line data," Theoretical Division (T-8), MS b=B285, Los Alamos National Laboratory (2001).

[29] Demtroder, W., [*Handbook of Laser Technology and Applications*], 169, Springer (2010).

[30] Fox, M., [*Quantum Optics, An Introduction*], 41, Oxford University Press (2009).

[31] Acosta, V. et al., "Nonlinear magneto-optical rotation with frequency-modulated light in the geophysical field range," *Physical Review A* **73**, 053404 (May 2006).

[32] Budker, D. and Kimball, D. F. J., [*Optical Magnetometry*], 6, Cambridge University Press (2013).

[33] Seltzer, S., Meares, P., and Romalis, M., "Synchronous optical pumping of quantum revival beats for atomic magnetometry," *Physical Review A* **75**, 051407 (May 2007).

[34] Guzhi, B., Wickenbrock, A., Rochester, S., Zhang, W., and Budker, D., "Suppression of the nonlinear zeeman effect and heading error in earth-field-range alkali-vapor magnetometers," *Physical Review Letters* **120**, 051407 (May 2018).

[35] Budker, D. and Kimball, D. F. J., [*Optical Magnetometry*], 9, Cambridge University Press (2013).

[36] Fox, M., [*Quantum Optics, An Introduction*], 54, Oxford University Press (2009).

[37] Foot, C., [*Atomic Physics*], Oxford University Press (2005).

[38] Auzinsh, M., Budker, D., and Rochester, S., [*Optically Polarized Atoms*], Cambridge University Press (2009).

[39] Erickson, C., *Measurements of the Magnetic Field Dependence of the Spin Relaxation Rate in Alkali Metal Vapours*, PhD thesis, Princeton University (2000).

[40] Happer, W., Jau, Y.-Y., and Walker, T., [*Optically Pumped Atoms*], 118, Wiley (2010).

[41] Abragam, A., [*The Principles of Nuclear Magnetism*], Oxford University Press (1961).

[42] Bin, B., Yu, Z., Ruifeng, L., Huaibin, Z., Yunlong, W., Fuli, L., and Zhuo, X., "Hanbury brown-twiss effect without two-photon interference in photon counting regime," *Scientific Reports* **7**(1), 2145 (2017).

[43] Budker, D. and Kimball, D. F. J., [*Optical Magnetometry*], 27, Cambridge University Press (2013).

[44] Ledbetter, M., Savukov, I., Acosta, V., and Budker, D., "Spin-exchange relaxation-free magnetometry with cs vapor," *Physical Review Letters* **104**(1), 033408 (2008).

[45] Budker, D. and Kimball, D. F. J., [*Optical Magnetometry*], 26, Cambridge University Press (2013).

[46] Savukov, I., Seltzer, S., and Romalis, M., "Tunable atomic magnetometer for detection of radio-frequency magnetic fields," *Physical Review Letters* **95**(6), 063004 (2005).

[47] Seltzer, S. and Romalis, M., "High temperature alkali vapor cells with antirelaxation surface coatings," *Journal of Applied Physics* **106**(11), 114905 (2009).

[48] Robinson, H., Ensberg, E., and Dehmelt, H., "Preservation of spin state in free atom-inert surface collisions," *Bulletin of the American Physical Society* **3**(9), 162 (1958).

[49] Sulai, I., Wyllie, R., Kauer, M., Smetana, G., Wakai, R., and Walker, T., "Diffusive suppression of ac-stark shifts in atomic magnetometers," *Optics Letters* **38**(6), 974–976 (2013).

[50] Budker, D. and Kimball, D. F. J., [*Optical Magnetometry*], 19, Cambridge University Press (2013).

[51] Happer, W. and Tam, A., "Effect of rapid spin-exchange on the magnetic-resonance spectrum of alkali vapors," *Physical Review A* **16**, 1877–1891 (11 1977).

[52] Haroche, S. and Cohen-Tannoudji, C., "Resonant transfer of coherence in nonzero magnetic field between atomic levels of different g-factors," *Physical Review Letters* **24**, 974 (05 1970).

[53] Purcell, E. and Field, G., "Influence of collisions upon population of hyperfine states in hydrogen," *Astrophysics* **124**, 542–549 (06 1956).

[54] Happer, W. and Tang, H., "Spin-exchange shift and narrowing of magnetic resonance lines in optically pumped alkali vapours," *Physical Review Letters* **31**, 273–276 (07 1973).

[55] Macintyre, S., [*Electrical Measurement, Signal Processing and Displays*], CRC Press (2003).

[56] Tumanski, S., "Induction coil sensors- a review," *Measurement Science and Technology* **18**(3), 31–46 (2007).

[57] Kaye and Online, L., [*Tables of Physical and Chemical Constants*], National Physical Laboratory (1995).

[58] Tumanski, S., "Modern magnetic field sensors- a review," *Przeglad Elektrotechniczny* **89**(10), 1–12 (2013).

[59] Coillot, C., Leroy, P., and Kuang, K., [*Induction Magnetometers Principle, Modeling and Ways of Improvement, Magnetic Sensors - Principles and Applications*], INTECH DOI: 10.5772/38945 (2012). Available from: https://www.intechopen.com/books/magnetic-sensors-principles-and-applications/induction-magnetometers-principle-modeling-and-ways-of-improvement.

[60] Roux, A., Le Contel, O., Coillot, C., et al., "The search coil magnetometer for themis," *Space Science Review* **141**(1-4), 265–275 (2008).

[61] Musmann, G. and Afanassiev, Y., [*Fluxgate Magnetometers for Space Research*], Herstellung und Verlag (2010).

[62] Vetoshko, P., Gusev, N., Chepurnova, D., et al., "Flux-gate magnetic field sensor based on yttrium iron garnet films for magnetocardiography investigations," *Phys. Lett.* **42**(860), 860–864 (2016).

[63] Fenici, R., Brisinda, D., and Meloni, A. M., "Clinical application of magnetocardiography," *Expert Review of Molecular Diagnostics* **5**(3), 291–313 (2005).

[64] Kleiner, R., Koelle, D., Ludwig, F., and Clarke, J., "Superconducting quantum interference devices: State of the art and applications," *IEEE Proceedings* **92**(10), 1534 – 1548 (2004).

[65] Clarke, J. and Barginski, A., [*The SQUID handbook Vol. I Fundamentals and Technology of SQUIDS and SQUID Systems*], Wiley-VCH (2004).

[66] Dunlop, D. and Ozdemir, O., [*Rock Magnetism: Fundamentals and Frontier*], Cambridge University Press (1997).

[67] Millen, R. L., *Giant Magneto Resistive Sensors and Magnetic Labels for Chip-Scale Detecton of Immunosorent Assays*, PhD thesis, Iowa State University (2005).

[68] Reig, C., Cardoso de Freitas, S., and Mukhopadhyay, S., [*Giant Magnetoresistance Sensors (From Basis to State-of-the-Art Applications)*], Springer (2013).

[69] Reig, C., Cubells-Beltran, M., and Munoz, D., "Magnetic field sensors based on giant magnetoresistance (gmr) technology: Applications in electrical current sensing," *MDPI Sensors 1424-8220* **9**(10), 7919–7942 (2009).

[70] Ferreira, R., Wisniowski, P., Freitas, P., Langer, J., Ocker, B., and Maass, W., "Tuning of mgo barrier magnetic tunnel junction bias current for picotesla magnetic field detection," *Journal of Applied Physics* **99**(8), 08K706 (2006).

[71] Robbes, D., Dolabdijan, C., Saez, S., Monfort, Y., Kaiser, G., and Ciureanu, P., "Highly sensitive uncooled magnetometers: State of the art superconducting magnetic hybrid magnetometers, an alternative to SQUID?," *IEEE Transactions on Applied Superconductivity* **100**(1), 629–634 (2001).

[72] Li, G., Sun, S., and et al., W. R., "Spin valve sensors for ultrasensitive detection of superparamagnetic nanoparticles for biological applications," *Sensors and Actuators A, Physical* **126**(1), 98–106 (2006).

[73] Tian, G., Al-Qubaa, A., and Wilson, J., "Design of an electromagnetic imaging system for weapon detection based on gmr sensor arrays," *Sensors and Actuators A* **174**, 75–84 (2012).

[74] Hrvoic, D., "Seaspy overhauser magnetometer technical application guide," Marine Magnetics, Corp (2007).

[75] Toh, H., Goto, T., and Hamano, Y., "A new seafloor electromagnetic station with an overhauser magnetometer, a magnetotelluric variograph and an acoustic telemetry modem," *Earth, Planets and Space* **50**(11-12), 895–903 (1998).

[76] Mandea, M. and Korte, M., [*Geomagnetic Observations and Models*], Springer (2011).

[77] Schirhagl, R., Chang, K., Loretz, M., and Degen, C., "Nitrogen-vacancy centers in diamond: Nanoscale sensors for physics and biology," *Annual Review of Physical Chemistry* **65**, 83–105 (2014).

[78] Rondin, L., Tetienne, J., Hingant, T., et al., "Magnetometry with nitrogen-vacancy defects in diamond," *Reports on Progress in Physics* **77**(5), 056503 (2014).

[79] Arnaut, J., [*Nanodiamonds. Advanced Material Analysis, Properties and Applications*], 19, Elsevier (2017).

[80] Schafer-Nolte, E. O., *Development of a Diamond-based Scanning Probe Spin Sensor Operating at Low Temperature in Ultra High Vacuum*, PhD thesis, University of Stuttgart (2014).

[81] Hong, S., Grinolds, M., Pham, L., Le Sage, D., Luan, L., Walsworth, R., and Yacoby, A., "Nanoscale magnetometry with nv centers in diamond," *MRS Bulletin* **38**(2), 155–161 (2013).

[82] Sander, T., Preusser, J., Mhaskar, R., Kitching, J., Trahms, L., and Knappe, S., "Magnetoencephalography with a chip-scale atomic magnetometer," *Biomedical Optics Express* **3**, 981–990 (05 2012).

[83] Schwindt, P., Knappe, S., Shah, V., Hollberg, L., and Kitching, J., "Chip-scale atomic magnetometer," *Applied Physics Letters* **85**, 6409–6411 (12 2004).

[84] Savukov, I., Seltzer, S., and Romalis, M., "Detection of nmr signals with a radio-frequency atomic magnetometer," *Journal of Magnetic Resonance* **185**(2), 214–220 (2007).

[85] Marmugi, L., Gori, L., Hussain, S., Deans, C., and Renzoni, F., "Remote detection of rotating machinery with a portable atomic magnetometer," *Applied Optics* **56**(3), 743–749 (2017).

[86] Romalis, M. and Dang, D., "Atomic magnetometers for materials characterisation," *Materials Today* **14**(6), 258–262 (2011).

[87] Ma, L. and Soleimani, M., "Magnetic induction tomography and applications: a review," *Measurement Science and Technology* **28**(7), 072001 (2017).

[88] Shah, V. and Wakai, R., "A compact, high performance atomic magnetometer for biomedical applications," *Physics in Medicine and Biology* **58**(22), 8153–8161 (2013).

[89] Marmugi, L. and Renzoni, F., "Optical magnetic induction tomography of the heart," *Nature Scientific Reports* **6**, 23962 (2016).

[90] Budker, D. and Kimball, D. F. J., [*Optical Magnetometry*], 265, Cambridge University Press (2013).

[91] Higbie, J., Rochester, S., Patton, B., Holzohner, R., Calia, D., and Budker, D., "Magnetometry with mesospheric sodium," *Proceedings of the National Academy of Sciences of the United States of America* **108**(9), 3522–3525 (2011).

[92] Kort, H., Strohbehn, K., Tejada, F., et al., "Miniature atomic scalar magnetometer for space based on the rubidium isotope 87Rb," *Wiley Journal of Geophysical Research Space Physics* **121**(8), 7870–7880 (2016).

[93] Kuvshinov, A. and Olsen, N., [*Earth Observation with CHAMP: Results from Three Years in Orbit*], Springer, Berlin, Heidelberg (2005).

[94] Tyler, R., Maus, S., and Luhr, H., "Satellite observations of magnetic fields due to ocean tidal flow," *Science* **299**(5604), 239–241 (2003).

[95] Mansor, M. et al., "Magnetic induction tomography: A brief review," *Jurnal Teknologi* **73**(3), 91–95 (2015).

[96] Vescent Photonics, "D2-100 dbr laser manual." Accessed: 2015-07-30.

[97] Carroll, J., Whiteaway, J., and Plumb, D., [*Distributed Feedback Semiconductor Lasers*], SPIE- The International Society for Optical Engineering (1998).

[98] Al-Azzawi, A., [*Fibre Optics Principles and Practices*], 126, CRC Press (2007).

[99] Kenyon, I., [*The Light Fantastic. A Modern Introduction to Classical and Quantum Optics*], 287, Oxford University Press (2008).

[100] Yashchuka, V., Budker, D., and Davis, J., "Laser frequency stabilization using linear magneto-optics: Technical notes," Report LBNL-43523, Univeristy of Berkeley (1999).

[101] Arrasmith, W., [*Systems Engineering and Analysis of Electro-Optical and Infrared Systems*], CRC Press (2015).

[102] Rao, M., [*Optical Communication*], Sangam Books Ltd (2000).

[103] McCarron, D., "A guide to acousto-optic modulators." Online Resource.

[104] Sherlock, B. and Hughes, I., "How weak is a weak probe in laser spectroscopy?," *American Journal of Physics* **77**(2), 111–115 (2009).

[105] Donley, E., Heavner, T., Levi, F., Tataw, M., and Jefferts, S., "Double-pass acousto-optic modulator system," *Review of Scientific Instruments* **76**(6), 063112 (2005).

[106] Webb, C. and Jones, J., [*Handbook of Laser Technology and Applications*], vol. 1, 201–213, IOP Publishing Ltd (2004).

[107] Budker, D., Kimball, D., and DeMille, D., [*Atomic Physics: An Exploration Through Problems and Solutions*], Oxford University Press (2004).

[108] Tiporlini, V. and Alameh, K., "High sensitivity optically pumped quantum magnetometer," *Scientific World Journal* , 858379 (2013).

[109] Karmel, P., Colef, G., and Camisa, R., [*Introduction to Electromagnetic and Microwave Engineering*], Wiley-Interscience (1998).

[110] "TN1000 What is a Lock-In Amplifier?." http://www.thinksrs.com/downloads/PDFs/ApplicationNotes/AboutLIAs.pdf. Accessed: 2017-09-12.

[111] Deans, C., Marmugi, L., Hussain, S., and Renzoni, F., "Electromagnetic induction imaging with a radio-frequency atomic magnetometer," *Applied Physics Letters* **108**(10), 103503 (2016).

[112] Sinclair, G., Appleby, R., Coward, P., and Price, S., "Passive millimeter-wave imaging in security scanning," *Proceedings SPIE* **4032**, 39–45 (2000).

[113] Ye, C. and Wei, T., [*Tunable External Cavity Diode Lasers*], World Scientific Publishing Co. (2004).

[114] Rosenbusch, P., X., B., Gauget, A., et al., "Interference-filter-stabilized external-cavity diode lasers," *Optics Communications* **266**(2), 609–613 (2006).

[115] "4340 High Tensile Steel." http://www.ssm.co.nz/sitefiles/4340.pdf. Accessed: 2018-03-05.

[116] "Stainless Steel Grade AISI420." http://www.steeleaglemalta.com/metal-calculator/stainless-steel-products/. Accessed: 2018-03-05.

[117] Hovde, C., Patton, B., Corsini, E., Higbie, J., and Budker, D., "Sensitive optical atomic magnetometer based on nonlinear magneto-optical rotation," *Proceedings SPIE* **7693**, 7693 – 7693 – 10 (2010).

[118] "Product attributes." https://www.digikey.com/product-detail/en/sunon-fans/KDE2412PMB1-6A/KDE2412PMB1-6A-ND/361502. Accessed: 2018-03-14.

[119] Cooper, J. D., [*Soil Water Measurement. A Practical Handbook*], Wiley Blackwell (2016).